February 2022

Infrared Investigation of Lithium Ion Electrolytes: Characterization of Structure and Dynamics via Linear and Nonlinear Spectroscopy

Jeramie Christopher Rushing
Louisiana State University and Agricultural and Mechanical College

INFRARED INVESTIGATION OF LITHIUM ION ELECTROLYTES: CHARACTERIZATION OF STRUCTURE AND DYNAMICS VIA LINEAR AND NONLINEAR SPECTROSCOPY

A Dissertation

Submitted to the Graduate Faculty of the
Louisiana State University and
Agricultural and Mechanical College
in partial fulfillment of the
requirements for the degree of
Doctor of Philosophy

in

The Department of Chemistry

by
Jeramie Christopher Rushing
B.S., The University of Alabama, 2016
May 2022

ACKNOWLEDGEMENTS

As part of the formalities for picking an advisor, I distinctly recall meeting Daniel for the first time; from the moment I set foot in the office, he was ready to put me to work. He has a small whiteboard in his office, far too small for the ideas littering it, and we spent over an hour discussing plans for future research. Equal parts enthusiastic and skeptical of new data, his scientific zeal never falters, and this fosters within the research group a sense of purpose. Working with Daniel is an evolving challenge because he has a knack for identifying difficult problems and an expectation that the researchers in his charge will rise to the task. I have learned, far beyond the scope of writing publications and aligning optics, how to identify and resolve these problems, perhaps the truest metric of a scientist. I leave a better researcher in every faculty and cannot thank Daniel enough for his guidance, perspective, and aptitude for being (frustratingly) correct.

I give further thanks to my committee members. For my general exam, I proposed a study of polymer hydrogels, having no experience with polymers myself, to experts in Dr. Schneider and Dr. Pojman. Their interest and keen inquiry prepared me to characterize polymer gels in my third project. Dr. Lopata tends to ask the toughest questions in the room, so walking away from my defense with his probing insight was gratifying. He was also asked to replace Dr. Pojman close to the defense, so I greatly appreciate his openness despite his limited availability.

I would also like to express gratitude to current and past members of the Kuroda group. Drs. Fulfer, Cui, Zhang, and Chen were always accessible for discussion and quick to exchange tips on everything from lab techniques to software complications. The younger group members, Ernest Nachaki, Laura Sepulveda, and Anit Gurung, are already engaged with complicated tasks across the spectrum of computational and experimental problems, and I look forward to the new

ground they tread. I find increasingly that I cement my understanding through teaching, so having such sharp peers spurred my growth as a scientist and forced me to be more sociable than I would otherwise elect. I give special thanks to Dr. Susith RG Kankanamge, a truly selfless man, who made himself available pre- and post-graduation for research and career advice.

Lastly, I want to acknowledge my spouse, Ven Rushing, who has dealt admirably with my late nights in the lab and long weekends at the office. Science is often a pratfall of failure, and watching someone you love hit blockade after blockade in pursuit of a problem is not easy. The love, support, and constant laughter have sustained me through multitudinous difficulties, and a bright future awaits me only beside such a glowing presence.

TABLE OF CONTENTS

ABSTRACT

Lithium ion batteries are widely employed in energy storage, but the connection between the molecular interactions in their electrolytes and the macroscopic properties remains elusive. Across three vastly different electrolytes, speciation and dynamics were studied via linear and nonlinear infrared spectroscopy to shed light on this relationship. The impact of mixed solvation on ionic speciation was studied from the perspective of the anion, which revealed a significant energetic favorability for the formation of contact ion pairs in linear carbonate solvents over cyclic carbonates. Infrared spectroscopy and density functional theory calculations described a complete inversion of the speciation due to solvent composition from 74% free anion in the cyclic carbonate to 95% contact ion pair in the linear carbonate. The impact of adding a highly-fluorinated additive on the speciation of two different electrolytes was studied via linear infrared spectroscopy. These fluorinated co-solvents are typically considered inert species with no impact on the speciation, but the research presented opposite trends in infrared spectroscopy, nuclear magnetic resonance (NMR) spectroscopy, electrochemistry, and conductivity for the two different electrolytes, indicating a change in speciation with co-solvent concentration. To explain the interesting dependence of the change in speciation on the anion, density function theory (DFT) calculations showed the formation of weak hydrogen bonds between the TFSI- anion and the co-solvent; this interaction is not observed with the PF6- anion. Finally, a polyacrylonitrile polymer gel electrolyte was investigated. The results from linear spectroscopy showed different interactions in the electrolyte with increasing polymer concentration; polymer addition also raised the viscosity of the sample by orders of magnitude, changing the sample composition from a liquid electrolyte to a room-temperature gel. Interestingly, the dynamics determined from 2DIR spectroscopy are similar across sample. A molecular picture was proposed of the nitrile side-

chains interacting at the highest polymer concentration, forming channels to facilitate the flow of ions; these interactions were confirmed via differential scanning calorimetry. This synergistic approach enabled the complete characterization of these complex systems from multiple perspectives to fully understanding the unintuitive way the molecular interactions can alter the macroscopic properties.

CHAPTER 1. INTRODUCTION

1.1. Overview of electrolyte solvation

Lithium ion batteries have become the gold standard for energy storage with vast applications across portable electronics, power tools, and medical devices.[1-3] In the near future, the widespread adoption of electric vehicles and the necessity for large-scale energy storage for power grids will further drive investment in lithium-ion battery research, focused on systems with high stability, high efficiency, and low cost without compromising safety.[4, 5] Each of these factors is determined in part by the electrolyte used. The electrolyte is typically composed of a lithium salt dissolved in either an aqueous or organic solvent to dissociate the ions and form a room temperature liquid.[6] The composition of the electrolyte is highly tunable, accommodating different lithium salts, mixtures of solvents, and various electrolyte additives in pursuit of enhanced properties and lower cost.[7-11] The electrolyte acts as a medium between the positive and negative electrodes through which charge flows, so the system must simultaneously be electrochemically stable and perform efficient charge transfer.[12] This balancing act between improving safety, cost, and stability without sacrificing transport properties or energy density remains the key challenge facing electrolytes, and many interesting solutions to this conundrum have been proposed, though these resolutions frequently result in issues unto themselves.

Lithium ion batteries have seen broad adoption for an assortment of applications, but many questions remain unanswered about the individual interactions of the components at the molecular level.[6] Current electrolytes for lithium ion batteries typically use of a mixture of cyclic and linear organic carbonates as a solvent, which are chosen to counteract the pitfalls associated with the other component, namely the high viscosity of cyclic carbonates and the low

dielectric constant of linear carbonates.[6, 12] One particularly pressing matter is the question of what determines the preference for one solvent over another, since it has been shown that solvating ability is not determined exclusively by dielectric constant.[13] These mixed solvents present the possibility of preferential solvation and raise questions of whether the coordinating solvent alters the speciation, which has significant implications for the macroscopic properties, including conductivity and electrochemical stability.[14-18]

A solution to the poor electrochemical stability of certain electrolytes has been the addition of fluorinated additives, which enhance the stability through the composition of the electrode passivation layer.[19-21] Recent research calls into question whether the addition of these fluorinated additives impacts the molecular speciation along with the electrochemical properties.[22-26] The analysis of pseudo-concentrated electrolytes further links electrochemical stability (a macroscopic property) with the molecular interactions. Pseudo-concentrated electrolytes, which constitute an organic electrolyte diluted with a “non-interacting” co-solvent to change the properties of the electrolyte, have been shown to enhance electrolyte properties, including the electrochemical stability.[27-30] One work showed a non-monotonic trend in the conductivity with co-solvent concentration, while the viscosity decreased linearly.[31] This implies changes in the interactions with co-solvent addition, since the trends should both be monotonic if the only the trend in conductivity is due to the viscosity exclusively.[32] In some systems, the co-solvent has been shown to alter the species in solution, but this effect is not universal, prompting the question of whether different molecular interactions are involved.[24-26]

These concerns extend further to polymer gel electrolytes. Polymer gels are difficult to characterize due to the assortment of potential interactions between components.[33-35] A

growing body of literature studying these systems indicates that not all polymers confer the same properties to the corresponding gel electrolytes; if the polymer identity dictates the molecular interactions, then no general theory can be developed accounting for the interactions in all polymer gel electrolytes, further complicating analysis. Specifically, the addition of polyacrylonitrile to a lithium ion electrolyte has been shown to increase the conductivity.[33] This behavior is unexpected because interactions between the lithium cation and the well-studied polyethylene oxide (PEO) and poly(methyl methacrylate) (PMMA) polymers result in either lower conductivity or no change, respectively.[36, 37] Thus, an understanding of how the molecular level interactions impact the macroscopic properties is critical for both the enhancement of current electrolytes and the rational design of future electrolytes.

Fourier transform infrared (FTIR) spectroscopy and nuclear magnetic resonance (NMR) spectroscopy have historically been used to identify changes in structure and dynamics, but neither method is alone suited to the holistic study of lithium ion electrolytes. NMR spectroscopy can resolve dynamics of proteins and polymers, but the timescales probed (nanosecond processes, 10^{-9}) are much slower than the exchange processes in these electrolytes (picosecond processes, 10^{-12} sec).[38, 39] FTIR spectroscopy measures structure but lacks both the time resolution and frequency resolution of nonlinear spectroscopy, limiting its application to matters of dynamics and complex systems with overlapping peaks.[40, 41] The combined disadvantages of these methods rationalizes the use of two dimensional infrared (2DIR) spectroscopy to study high-resolution structure and ultrafast dynamics simultaneously. Data from FTIR spectroscopy is additionally taken with respect to only one frequency axis; accordingly, FTIR spectroscopy has a lower frequency resolution than 2DIR spectroscopy, which resolves data across two frequency axes.[38] It should also be noted that the generation of amplified femtosecond pulses upon which

2DIR spectroscopy relies was only achieved three decades ago, and the extraction of dynamics from experimental 2DIR data is a more recent development.[42-44] Thus, the body of work exploring systems via 2DIR spectroscopy is still limited compared to the vast selection of literature using NMR spectroscopy, and the application of 2DIR spectroscopy would benefit many systems with unresolved questions. Lithium ion batteries contain a multitude of components exchanging on ultrafast timescales, each of which has the potential to interact with one another, exactly the sort of complex system perfectly suited to analysis via 2DIR spectroscopy.[45-51]

1.2. Previous literature

1.2.1. Dilute organic electrolytes and mixed solvation

The earliest commercial lithium ion batteries were based on a petroleum coke anode and lithium cobalt oxide ($LiCoO_2$) cathode.[3, 52] Much research interest has since focused on improvements to the electrodes. Various functional cathode materials were rapidly developed, including lithium transition-metal oxides (with nickel, cobalt, manganese, and mixtures of the three metals employed), lithium metal phosphates, and lithium-air cathodes, which persist in modern applications.[53-56] Anodes have undergone their own improvements with modern materials including graphite, silicon-carbon hybrid systems, and lithium metal.[57-60] Compared to the drastic developments in electrode enhancement, the dilute lithium-ion electrolytes used alongside these electrodes has changed negligibly since the first generation of commercial batteries were introduced almost three decades ago; the basic structure of lithium hexafluorophosphate ($LiPF_6$) dissolved in an organic carbonate solvent is untouched.[61, 62] $LiPF_6$ was used as the lithium salt due to an assortment of desirable properties in carbonate solvents compared to similar candidates, including strong dissociation, high conductivity, ion

mobility, and electrochemical stability.[63-65] Cyclic carbonate solvents, primarily propylene carbonate (PC) or ethylene carbonate (EC) were chosen as electrolyte solvents due to their high dielectric constants and compatibility with the electrodes.[66-68] In spite of these advantages, these solvents alone are not ideal candidates, considering both the high viscosities of both solvents and the solid nature of EC at room temperature.[66, 67] The discovery of melting point depression in EC when mixed with a lithium salt or PC paved the way for its use as an electrolyte solvent; modern electrolytes typically take advantage of this depression by mixing EC with a linear carbonate, such as dimethyl carbonate, whose low viscosity combats the inherent high viscosity of the cyclic carbonates.[69-71]

Despite the frequent use of mixed carbonate solvents in modern dilute electrolytes, few studies have focused on the impact of multiple solvents on lithium solvation. In particular, studies on mixed solvation from the anion perspective have been limited by the lack of simple, isolated vibrational modes in many anions, which inhibits the study of dynamics and structural changes and complicates interpretation of the data.[15-17] Much work has been dedicated to the preferential solvation of lithium by one solvent over the other in binary solvent mixtures.[72-75] The work of the Lucht group specifically highlights the contribution of linear carbonates to the solvation shell of lithium even in the presence of free propylene carbonate; this is unexpected due to the significant disparity in dielectric constant between the linear and cyclic carbonates.[17] Moreover, density functional theory computations show lower energies for solvation shells with one conformation of the linear carbonate.[17] In this way, a clear link between the favorability of the lithium-solvent interaction due to solvent orientation and the composition of the lithium solvation shell is established, but the mechanism through which the

solvents in a mixed electrolyte alter the lithium solvation structure and affect the speciation remains unanswered.

1.2.2. Concentrated and pseudo-concentrated electrolytes

Another attempt to juggle the delicate balance between electrochemical properties and transport properties led to the development of highly-concentrated lithium-ion electrolytes. Anodes made of lithium metal have been proposed due to their increased capacity compared to graphite, but the dilute organic electrolytes previously discussed are electrochemically incompatible with these new electrodes and require the development of concentrated electrolytes.[12, 76-78] These electrolytes do not suffer many of the problems associated with lithium metal anodes: aluminum corrosion, dendrite formation, and growth of the solid electrolyte interface.[6, 76-81] The disadvantages of such stability are numerous and include low conductivity, high viscosity, and high cost due to the concentration of lithium salt.[82, 83] Solving the issues created by concentrated electrolytes would constitute a cheaper system with lower viscosity but which still possesses the inert electrochemical window imbued in the concentrated structure.

This Herculean task has been surmounted by the development of pseudo-concentrated electrolytes, formed by the dilution of concentrated electrolytes with a low viscosity co-solvent.[23, 84-88] In principle, the co-solvent does not interact with the primary lithium solvation shell and serves only to disrupt the rigid structure of the concentrated electrolyte, enabling small pockets of concentrated electrolyte to flow in solution, enhancing the conductivity.[22, 23] In spite of the exceptional properties of pseudo-concentrated electrolytes, questions remain regarding the level of interaction between the supposedly inert co-solvent and the electrolyte upon addition. Multiple studies show that the addition of a highly-halogenated co-

solvent to an electrolyte enhances the electrochemical stability, which is unexpected unless there are interactions among the components.[24, 26] Furthermore, spectroscopic evidence shows changes in the speciation with co-solvent addition for some systems and no change in speciation for others.[24, 25] Thus, unresolved questions remain regarding the true impact of co-solvent insertion on the solvation structure.

1.2.3. Polymer gel electrolytes

Another key problem facing current electrolytes is the choice of organic carbonates as electrolyte solvents. The same desirable properties (ion transport and lithium salt solubility) that make carbonate solvents excellent candidates for electrolytes contribute to their flammability, which fuels interest in developing safer electrolyte materials.[89, 90] One solution to the issue of flammability is the introduction of a polymer to a dilute carbonate electrolyte at the appropriate concentration to form a polymer gel.[91-93] The gel should allow the flow of solvated lithium ions, while stabilizing the flammable solvents. Unfortunately, the problem of characterizing the lithium solvation shell is not limited to solutions, as the role of the polymer in these electrolytes is still under investigation. There is significant evidence that the identity of the polymer influences its interactions with the electrolyte with some polymers like polyethylene oxide (PEO) dissociating ion pairs, some having no influence on the speciation like poly(methyl methacrylate) (PMMA), and some promoting stronger interactions between the lithium and anion, as seen for polyacrylonitrile (PAN).[33-35, 94-97] Moreover, different transport behaviors are observed with polymer identity, where, conductivity is coupled to the chain motions of the polymer for PEO, but the introduction of PMMA has no impact on the ion flow.[35-37, 97-103] Interestingly, PAN shows conductivity enhancement when added to a lithium ion electrolyte, which implies interactions between the electrolyte and polymer that are not present in other samples.[104, 105]

Probing the solvation structure of a polymer gel electrolyte is more complex than any of the electrolytes sampled thus far; in addition to all the liquid phase interactions that occur in a dilute electrolyte, polymer chains have the potential to interact with the cation, the anion, the solvent molecules, and other polymer chains.[33-35]

1.3. Infrared characterization of electrolytes

The solvation structure, which denotes the number and identity of molecules situated near the lithium cation, can distinguish between the various species in solutions, helping clarify the interactions at the molecular level.[17] Free ion species, where the lithium ion is solvated completely by solvent molecules and does not directly interact with the anion, produce free-flowing charges, generally increasing the conductivity; the lack of interactions with the cation, however, frees the anion to deposit on the electrodes, decreasing the electrochemical stability.[12, 18, 106, 107] When the lithium cation and anion are closer in space, they have stronger interactions and form ion pairs; the ion pair confers electrochemical stability, typically at the expense of higher viscosity and lower conductivity.[18, 108-111] Accordingly, solvation structure is the holy grail of characterization, as many electrolyte properties can be rationalized by the state of the lithium cation and corresponding anion in solution. Among other methods, nonlinear infrared spectroscopy has emerged as a pivotal tool for studying solvation structure and dynamics due to its sensitivity to chemical environments, enhanced frequency resolution, and ability to probe processes on picosecond timescales.[38, 112]

Two-dimensional infrared (2DIR) spectroscopy provides an unparalleled glimpse into the solvation structure of these complex systems through a series of laser pulses which label the vibrational frequencies and track their changes over time.[38, 112] The use of femtosecond laser pulses enables the study of processes which are orders of magnitude faster than those resolvable

via NMR spectroscopy, underscoring the utility of 2DIR spectroscopy for characterization.[39, 113, 114] By studying the change in vibrational frequency across waiting time, structure and dynamics can be simultaneously measured.[38, 113, 115] Understanding the processes underlying these vibrational peaks further improves the analysis by linking the motions of the system to the observed timescales; the peak assignment is often simplified through complementary linear Fourier transform infrared (FTIR) spectroscopy.[116] Measurements via linear infrared spectroscopy are much simpler to conduct and offer a convenient window into how infrared spectra change under various conditions, including concentration and temperature.[6, 17, 117-119] FTIR spectroscopy does not require the tedious alignment and long data acquisition times to which 2DIR is subjected, but FTIR lacks time resolutions, which limits its applicability for dynamics measurements. Combined, these methods offer a complete picture of local solvation around a selected vibrational frequency, through changes at equilibrium and non-equilibrium dynamics and structural changes. These spectroscopies have been used in tandem to study a multitude of systems including dilute electrolytes, concentrated electrolytes, ionic liquids, deep eutectic solvents, proteins, and polymer systems.[48-51, 119-135]

1.4. Dissertation Overview

The work herein probes the solvation structure and dynamics across three significantly different electrolytes, linked by the importance of the lithium solvation shell to the broader properties of the system. Across three projects, a case will be built that no component is negligible to the structure, dynamics, and macroscopic properties of the electrolyte.

Chapter 2 focuses on the theory of linear and nonlinear infrared spectroscopy. Beginning with the Schrodinger equation and a single wavefunction, a formalism is constructed for considering statistical averages of molecules, the interactions of the system with laser pulses, and

a description of the polarization and molecular response, which account for the time-dependent changes which are tracked spectroscopically and from which the 2DIR spectra originate. The chapter closes with a description of the experimental setup and how data acquisition is performed.

Chapter 3 chronicles the impact of a mixed solvent, composed of a linear and cyclic carbonate, on the structure and dynamics of a dilute organic electrolyte. The lithium 4,5-dicyano-2-trifluoromethylimidzaole (LiTDI) salt provides a unique window into the local structure via the nitrile modes of its anion. These spectroscopically distinct modes give a direct measure of the lithium-nitrile interactions, which are difficult to parse from the vibrational modes of other anions. The lithium-anion interactions are shown to be highly-dependent on the choice of solvent molecule with linear carbonates favoring the formation of ion pairs. Interestingly, the mixed solvent system always favors a mixed lithium solvation shell, in spite of the higher dielectric constant of the cyclic carbonate. This stabilization in the mixed system results from a conformational change of the linear carbonate when associated with the cation, shown via DFT computations.

Chapter 4 discusses the impact of adding 1,1,1,3,3-pentafluorobutnae (PFB), a highly-fluorinated alkane, as a co-solvent in two dilute electrolytes comprised of two different lithium salts. Combined characterization from FTIR, ATR, and NMR shows stronger lithium-anion interactions for the $LiPF_6$ electrolyte and weaker interactions for the LiTFSI electrolyte with the addition of PFB. The co-solvent addition is shown to cause different anion-dependent trends in the electrochemical stability, which is attributed to the different speciation in the two electrolytes via DFT computations. The origin of the different speciation is the unexpected formation of hydrogen bonds between the TFSI anion and PFB, which is evidenced by DFT computations.

Chapter 5 details the study of three polymer gel electrolyte systems across different concentrations: 0% polymer, 5% polymer, and 10% polymer by mass added to a dilute electrolyte. The interactions between the lithium cation and polymer are maximized for the 5% concentration, reflecting nonlinear dependence on the polymer content. The viscosity of the samples increases by orders of magnitude with the addition of polymer, but surprisingly the dynamics are nearly identical for the three systems. A molecular picture is proposed of the polymer chains forming channels through which the solvated cations can travel independent of the chain motions, such that viscosity and diffusion are not related. The polymer is proposed to form different structures with concentration, where more polymer-polymer interactions are observed in the 10% sample than at lower concentrations; this is supported by DSC data.

CHAPTER 2. INFRARED SPECTROSCOPY: THEORY AND EXPERIMENTAL METHODS

The development of a proper interpretation of nonlinear infrared spectra is useful for discussing the theory of both linear and nonlinear infrared spectroscopies. This chapter serves to develop an intuitive understanding of the relationship between molecular motions, interactions with the laser field, and the appearance of the experimentally-observed spectra. A description of the density matrix is critical, as it allows the representation of an ensemble of fluctuations rather than the fluctuations of a single oscillator via its wavefunction. The plethora of information necessary to understand the time evolution of the density matrix is organized into Feynman diagrams, which elegantly represent the state of the ensemble with each laser interaction. The polarization and response functions are developed for linear and nonlinear spectra, and their relation to the emitted signal in infrared experiments is discussed.[38] The 2DIR lineshape will be described semiclassically using a quantum mechanical treatment of the vibrational transitions and a classical treatment of the electric field of the laser; this semiclassical approximation follows the convention of Kubo's stochastic lineshape theory.[38, 136] Finally, the experimental 2DIR setup is described in depth, and the specifics of data acquisition are detailed.

2.1. Description of the density matrix

2.1.1. The wavefunction and density matrix

A pure state is any quantum state of a single molecule which can be described by a single wavefunction. The total Hamiltonian for a pure state $\hat{H}(t)$ is comprised of two terms: the time-independent molecular Hamiltonian $\hat{H}_0$ and the time-dependent potential $\hat{W}(t)$, which describes the perturbation of the wavefunction due to an interaction with the electric field:

$$\hat{H}(t) = \hat{H}_0 + \hat{W}(t) \tag{1}$$

where the potential $\hat{W}(t)$ is defined in terms of the electric field $E(t)$:

$$\begin{gathered}\hat{W}(t) = -\hat{\mu}E(t) \\ E(t) = E'(t)\cos(\omega t)\end{gathered} \tag{2}$$

with the pulse envelope $E'(t)$ including the polarization, which will be discussed later. $\hat{H}(t)$ has a time-dependence due to the potential term $\hat{W}(t)$, so the time evolution of the wavefunction is given by the time-dependent Schrödinger equation:

$$\frac{\partial}{\partial t}|\psi(t)\rangle = -\frac{i}{\hbar}\hat{H}(t)|\psi(t)\rangle \tag{3}$$

Because $\hat{H}_0$ has no time dependence, the energy eigenstates are those derived from the time-independent Schrödinger equation:

$$H_0|n\rangle = E_n|n\rangle \tag{4}$$

and the time-dependent wavefunction can be expanded in terms of the basis of $\hat{H}_0$:

$$|\psi(t)\rangle = \sum_n c_n(t)|n\rangle \tag{5}$$

with a time-dependent probability amplitude $c_n(t)$. The density operator, defined as $\rho = |\psi\rangle\langle\psi|$ for a pure state, is here introduced and expanded in in the basis of $\hat{H}_0$:

$$\rho = |\psi\rangle\langle\psi| = \sum_{n,m} c_n c_m^* |n\rangle\langle m| \tag{6}$$

where the wavefunction is denoted by a *ket* $|\psi\rangle = \sum_n c_n|n\rangle$ and its complex conjugate is denoted by the *bra* $\langle\psi| = \sum_n c_n^*\langle n|$. Then the evolution of the density matrix over time is:

$$\frac{d}{dt}\rho = \frac{d}{dt}(|\psi\rangle\langle\psi|) = (\frac{d}{dt}|\psi\rangle) \cdot \langle\psi| + |\psi\rangle \cdot (\frac{d}{dt}\langle\psi|) \tag{7}$$

and the time-dependent evolution of a wavefunction is simply the Schrödinger equation:

$$\frac{d}{dt}|\psi\rangle = -\frac{i}{\hbar}\hat{H}|\psi\rangle \tag{8}$$

$$\frac{d}{dt}\langle\psi| = +\frac{i}{\hbar}\langle\psi|\hat{H} \tag{9}$$

By plugging (8) and (9) into (7), the time evolution of ρ can be rewritten:

$$\begin{aligned}\frac{d}{dt}\rho &= -\frac{i}{\hbar}\hat{H}|\psi\rangle\langle\psi| + \frac{i}{\hbar}|\psi\rangle\langle\psi|\hat{H} \\ &= -\frac{i}{\hbar}\hat{H}\rho + \frac{i}{\hbar}\rho\hat{H} \\ &= -\frac{i}{\hbar}[\hat{H},\rho].\end{aligned} \tag{10}$$

Equation (10) is the Liouville-von Neumann equation, which describes the time evolution of the density matrix analogously to the description of the time evolution of the wavefunction via the Schrödinger equation.

2.1.2. Time dependence of a statistical average

The density matrix ρ has thus far been expressed for a pure state, but the true strength of the density matrix lies in its ability to represent ensembles, which are more apt for condensed-phase systems. The density matrix for a statistical average of molecules (an ensemble) is the sum of the weighted probabilities p_s of the system existing in each quantum state $|\psi_s\rangle$:

$$\rho = \sum_s p_s|\psi_s\rangle\langle\psi_s| \tag{11}$$

where $p_s \geq 0$ and by normalization $\sum_s p_s = 1$. If there is only one quantum state, ρ describes a pure state, and equation (11) matches the definition of ρ introduced in equation (6); likewise, the density matrix of a statistical ensemble can also be expanded in the basis of the molecular Hamiltonian:

$$\rho_{nm} = \sum_s p_s c_m^{s*} c_n^s = \langle c_m^{s*} c_n^s\rangle \tag{12}$$

and the time dependence of ρ_{nm} for s quantum states with weighted probabilities can be evaluated by applying the chain rule to equation (12):

$$\begin{aligned}\dot{\rho}_{nm} &= \sum_s \frac{dp_s}{dt} c_n c_m^* + \sum_s p_s \left(\frac{dc_n}{dt} c_m^* + c_n \frac{dc_m^*}{dt}\right) \\ &= \sum_s \frac{dp_s}{dt} c_n c_m^* - \frac{i}{\hbar}[\hat{H}, \rho]_{nm}\end{aligned} \tag{13}$$

where $\dot{\rho}_{nm}$ is the time derivative using Newton's notation. The second term of equation (13) is identical to the Liouville-von Neumann equation, while the first term denotes the average fluctuation of the probability for each state. To understand the first term of equation (13), it is useful to introduce the matrix elements of the density matrix. For a simple system with only ground state $|0\rangle$ and first excited state $|1\rangle$, an interaction with a laser pulse results in (1) the promotion of some ground state molecules to the excited state and (2) the creation of a superposition between states $|0\rangle$ and $|1\rangle$, such that the wavefunction is now described by a linear combination of states:

$$\begin{aligned}|\Psi\rangle &= c_0 e^{-iE_0 t/\hbar}|0\rangle + i c_1 e^{-iE_1 t/\hbar}|1\rangle \\ &\equiv c_0(t)|0\rangle + i c_1(t)|1\rangle\end{aligned} \tag{14}$$

The density matrix is defined as $\rho = |\psi\rangle\langle\psi|$, so the density matrix after interaction with a laser pulse gives:

$$\rho = \begin{pmatrix}\rho_{00} & \rho_{01} \\ \rho_{10} & \rho_{11}\end{pmatrix} = \begin{pmatrix}\langle c_0(t) c_0^*(t)\rangle & -i\langle c_0(t) c_1^*(t)\rangle \\ i\langle c_1(t) c_0^*(t)\rangle & \langle c_1(t) c_1^*(t)\rangle\end{pmatrix} \tag{15}$$

Looking at the diagonal terms of ρ, $\langle c_0(t) c_0^*(t)\rangle$ represents the average probability amplitude of molecules being in the ground state with time; $\langle c_1(t) c_1^*(t)\rangle$ similarly gives the average probability of molecules occupying the first excited state. Two important conclusions can be drawn from these diagonal terms. First, the terms describe the population of molecules in the

ground state ρ_{00} and first excited state ρ_{11} individually; the populations are not in a superposition state. Second, since all molecules must be in either state $|0\rangle$ or $|1\rangle$, the population of the excited state is inversely proportional to the population of the ground state:

$$\rho_{00}(t) = 1 - \rho_{11}(t) \tag{16}$$

One consequence of this relation is population relaxation, where energy loss causes molecules in the excited state to return to the ground state. Since the excited state population is generated by the interaction with a laser, removing the energy source results in a decay of the excited state population with time T_1:

$$\rho_{11}(t) = \rho_{11}(0)e^{-t/T_1} \tag{17}$$

This sets a limit on the measurement of vibrational dynamics via nonlinear spectroscopy related to the lifetime of the sample in the excited state.

Considering instead the anti-diagonal terms, ρ_{01} and ρ_{10} depend on the average probability of the superposition and not an individual quantum state. The interaction with the laser pulse select via polarization all the molecules in an ensemble in-phase, such that their vibrational frequencies are overlapped directly after the interaction. These molecules are said to be coherent, and their coordinated oscillation generates a field measured via experiment. Since each molecule experiences a slightly different local environment, their vibrational frequencies are all different, and molecules with larger vibrational frequency will move faster than the rest of the molecules, resulting in a dispersion of the coherence. As the molecules lose phase correlation, they destructively interfere, and the emitted signal decays to zero. Just as the excited state population decays in time, the vibrational coherence equivalently dephases with time T_2:

$$\rho_{01}(t) = -ic_0c_1e^{+i\omega_{01}t}e^{-t/T_2}$$

$$\rho_{10}(t) = ic_0c_1e^{-i\omega_{01}t}e^{-t/T_2} \tag{18}$$

With a firm understanding of how population and coherence are represented by ρ, equation (13) is revisited, namely the previously untouched first term. This term characterizes the average fluctuation of the wavefunction coefficients $c_n c_m^*$, which are related to the probability of an associated state. For $c_n = c_m$, this is the change in the probability of finding a molecule in either the ground state $c_n c_m^* = c_0 c_0^*$ or excited state $c_n c_m^* = c_1 c_1^*$ with time; this is simply a description of population relaxation. For $c_n \neq c_m$, the probability changes for the interaction terms $c_n c_m^* = c_0 c_1^*$ and $c_n c_m^* = c_1 c_0^*$, which are the vibrational coherences; the time-dependent change of the coherence probability is just the dephasing of the coherences. Equation (13) thereby accounts for the general time evolution of the density matrix (via the Liouville-von Neumann equation), as well as the loss of coherence and decay of the excited state population which arise from considering an ensemble.

2.1.3. The interaction picture and perturbative treatment of W(t)

In spectroscopy, the interactions between the system and the laser pulse $\hat{W}(t)$ dictate the dynamics, and the wavefunction is described in terms of the time intervals separating the laser pulses. To develop the density matrix in this way, the wavefunction is rewritten in the interaction picture:

$$|\psi(t)\rangle \equiv e^{-\frac{i}{\hbar}\hat{H}_0(t-t_0)}|\psi_I(t)\rangle \tag{19}$$

where the total wavefunction is taken with respect to a reference time t_0. $|\psi(t)\rangle$ depends on $\hat{H}(t) = \hat{H}_0 + \hat{W}(t)$, and the time evolution due to the molecular Hamiltonian is collected in the exponential term of equation (19). Accordingly, the time evolution of wavefunction in the

interaction picture $|\psi_I(t)\rangle$ is attributed to the difference $\hat{H}(t) - \hat{H}_0 = \hat{W}(t)$. The time evolution of the wavefunction $|\psi_I(t)\rangle$, described by the Schrödinger equation, depends only on the perturbation due to interactions with the laser pulse $\hat{W}(t)$:

$$\frac{d}{dt}|\psi_I(t)\rangle = -\frac{i}{\hbar}\hat{W}_I(t)|\psi_I(t)\rangle \tag{20}$$

where the perturbation has also been defined with respect to a reference time t_0 in the interaction picture:

$$\hat{W}_I(t) = e^{\frac{i}{\hbar}\hat{H}_0(t-t_0)}\hat{W}(t)e^{-\frac{i}{\hbar}\hat{H}_0(t-t_0)} \tag{21}$$

The choice of the interaction picture simplifies the evaluation of $|\psi_I(t)\rangle$ in that the integration of equation (20) over the range $t_0 \to t$ separates the wavefunction into the time-independent wavefunction and time-dependent perturbation term:

$$|\psi_I(t)\rangle = |\psi_I(t_0)\rangle - \frac{i}{\hbar}\int_{t_0}^{t} d\tau \hat{W}_I(\tau)|\psi_I(\tau)\rangle \tag{22}$$

and the last term can be expanded by perturbation theory to include the second-order correction:

$$\begin{aligned} |\psi_I(t)\rangle = \quad & |\psi_I(t_0)\rangle - \frac{i}{\hbar}\int_{t_0}^{t} d\tau \hat{W}_I(\tau)|\psi_I(t_0)\rangle \\ & +(-\frac{i}{\hbar})^2\int_{t_0}^{t} d\tau_2 \int_{t_0}^{\tau_2} d\tau_1 \hat{W}_I(\tau_2)\hat{W}_I(\tau_1)|\psi_I(\tau_1)\rangle \end{aligned} \tag{23}$$

or more generally, the *n*th-order correction describing a power series of $\hat{W}(t)$:

$$\begin{aligned} |\psi_I(t)\rangle = |\psi_I(t_0)\rangle + \sum_{n=1}^{\infty}(-\frac{i}{\hbar})^n \int_{t_0}^{t} d\tau_n \int_{t_0}^{t_n} d\tau_{n-1} \cdots \int_{t_0}^{t_2} d\tau_1 \\ \hat{W}_I(\tau_n)\hat{W}_I(\tau_{n-1}) \cdots \hat{W}_I(\tau_1)|\psi_I(t_0)\rangle \end{aligned} \tag{24}$$

Converting from the interaction picture to the Schrödinger picture, an intuitive explanation of the time evolution emerges:

$$|\psi(t)\rangle = |\psi^{(0)}(t)\rangle + \sum_{n=1}^{\infty}(-\frac{i}{\hbar})^n \int_{t_0}^{t} d\tau_n \int_{t_0}^{\tau_n} d\tau_{n-1} \cdots \int_{t_0}^{\tau_2} d\tau_1$$
$$e^{-\frac{i}{\hbar}\hat{H}_0(t-\tau_n)}\hat{W}(\tau_n)e^{-\frac{i}{\hbar}\hat{H}_0(\tau_n-\tau_{n-1})}\hat{W}(\tau_{n-1})\cdots$$
$$\cdots e^{-\frac{i}{\hbar}\hat{H}_0(\tau_2-\tau_1)}\hat{W}(\tau_1)e^{-\frac{i}{\hbar}\hat{H}_0(\tau_1-t_0)}|\psi(t_0)\rangle \tag{25}$$

where the time dependence of the zeroth-order wavefunction comes only from propagation under influence of the molecular Hamiltonian $\hat{H}_0$:

$$|\psi^{(0)}(t)\rangle \equiv e^{-\frac{i}{\hbar}\hat{H}_0(t-t_0)}|\psi(t_0)\rangle \tag{26}$$

Before interaction with the laser field, the total wavefunction $|\psi(t)\rangle$ is influenced only by the molecular Hamiltonian with time evolution described by $e^{-\frac{i}{\hbar}\hat{H}_0(t-t_0)}$. The first interaction with the laser pulse occurs at τ_1, represented as the perturbation $\hat{W}(\tau_1)$, after which the wavefunction again propagates until the next interaction $\hat{W}(\tau_2)$ at τ_2. The set of times $[\tau_1, \tau_2, \ldots \tau_n]$ and the laser interactions $\hat{W}(\tau)$ can be used to construct Feynman diagrams, which describe pictorially the time evolution of the wavefunction under interactions with laser fields. More interestingly, if the density matrix rather than the wavefunction is expanded by perturbation theory, Feynman diagrams can be drawn cataloguing the time evolution of the density matrix under all interactions! The density matrix in the interaction picture is developed in a straightforward way from equation (19):

$$|\psi(t)\rangle\langle\psi(t)| = e^{-\frac{i}{\hbar}\hat{H}_0(t-t_0)}|\psi_I(t)\rangle\langle\psi_I(t)|e^{+\frac{i}{\hbar}\hat{H}_0(t-t_0)} \tag{27}$$

where the outer product $|\psi_I(t)\rangle\langle\psi_I(t)|$ is the density matrix in the interaction picture, $\rho_I(t)$. In the interaction picture, the time evolution of the wavefunction is equivalent to the Schrödinger equation, as shown in equation (20). For the perturbative expansion of the density matrix, the time evolution is equivalent to the Liouville-von Neumann equation, as proven in equation (10):

$$\frac{d}{dt}\rho_I(t) = -\frac{i}{\hbar}[\hat{W}_I(t), \rho_I(t)] \tag{28}$$

and perturbation theory can be applied similarly to the expansion of the wavefunction to derive a power series expansion in terms of $\hat{W}_I(\tau)$:

$$\begin{aligned}\rho_I(t) = \quad & \rho_I(t_0) + \sum_{n=1}^{\infty}(-\frac{i}{\hbar})^n \int_{t_0}^{t} d\tau_n \int_{t_0}^{\tau_n} d\tau_{n-1} \cdots \int_{t_0}^{\tau_2} d\tau_1 \\ & [\hat{W}_I(\tau_n), [\hat{W}_I(\tau_{n-1}), \cdots [\hat{W}_I(\tau_1), \rho_I(t_0)] \cdots]]\end{aligned} \tag{29}$$

and converting the density matrix back to the Schrödinger picture gives the unperturbed density matrix and a power series of correction terms accounting for the time evolution due to electric field interactions:

$$\begin{aligned}\rho(t) = \quad & \rho^{(0)}(t) + \sum_{n=1}^{\infty}(-\frac{i}{\hbar})^n \int_{t_0}^{t} d\tau_n \int_{t_0}^{\tau_n} d\tau_{n-1} \cdots \int_{t_0}^{\tau_2} d\tau_1 \\ & e^{-\frac{i}{\hbar}\hat{H}_0(t-t_0)}[\hat{W}_I(\tau_n), [\hat{W}_I(\tau_{n-1}), \cdots [\hat{W}_I(\tau_1), \rho(t_0)] \cdots]]e^{+\frac{i}{\hbar}\hat{H}_0(t-t_0)} \\ \equiv \quad & \rho^{(0)}(t) + \sum_{n=1}^{\infty}\rho^{(n)}(t)\end{aligned} \tag{30}$$

Two important facts should be noted about equation (30). First, when converting $\rho(t)$ back to the Schrödinger picture ,the perturbation terms $\hat{W}_I(\tau)$ are left in the interaction picture. Second, the interactions between the density matrix and $\hat{W}_I(\tau)$ are written as commutators. Because the density matrix $\rho = |\psi\rangle\langle\psi|$ is composed of a *ket* $|\psi\rangle$ and *bra* $\langle\psi|$, the perturbations can interact with either term, and interactions from the left (acting on the *ket*) and from the right (acting on the *bra*) must be considered.

2.1.4. Macroscopic polarization and response functions

Since the perturbation $\hat{W}(t)$ can interact with both $|\psi\rangle$ and $\langle\psi|$ of the density matrix, it is useful to revisit its role as an operator, defined as $\hat{W}(t) = -\hat{\mu}E(t)$ in equation (2). The dipole moment can operate on ρ, but the electric field, a scalar, cannot. Substituting this definition into

equation (30), the electric field can be removed from the commutator, and the perturbation of ρ depends only on its interaction with the dipole operator $\hat{\mu}$:

$$\begin{aligned}\rho^{(n)}(t) = \quad & -(-\frac{i}{\hbar})^n \int_{t_0}^{t} d\tau_n \int_{t_0}^{\tau_n} d\tau_{n-1} \cdots \int_{t_0}^{\tau_2} d\tau_1 E(\tau_n) E(\tau_{n-1}) \cdots E(\tau_1) \\ & \cdot e^{-\frac{i}{\hbar}\hat{H}_0(t-t_0)} [\hat{\mu}_I(\tau_n), [\hat{\mu}_I(\tau_{n-1}), \cdots [\hat{\mu}_I(\tau_1), \rho(t_0)] \cdots]] e^{+\frac{i}{\hbar}\hat{H}_0(t-t_0)}\end{aligned} \tag{31}$$

with the dipole operator rewritten in the interaction picture as:

$$\hat{\mu}_I(t) = e^{+\frac{i}{\hbar}\hat{H}_0(t-t_0)} \hat{\mu} e^{-\frac{i}{\hbar}\hat{H}_0(t-t_0)} \tag{32}$$

It is worth noting that $\hat{\mu}$ is time-independent in the Schrödinger picture but time-dependent $\hat{\mu}_I(t)$ in the interaction picture. The value in this substitution lies in the definition of the macroscopic polarization:

$$P(t) = \mathrm{Tr}(\hat{\mu}\rho(t)) \equiv \langle \hat{\mu}\rho(t) \rangle \tag{33}$$

The macroscopic polarization is just the expectation value of the dipole operator, and the *n*th order polarization is similarly:

$$P^{(n)}(t) = \langle \hat{\mu}\rho^{(n)}(t) \rangle \tag{34}$$

Equation (31) defines the density matrix in terms of n perturbative interactions, such that substitution into equation (34) gives:

$$\begin{aligned}P^{(n)}(t) = - \quad & (-\frac{i}{\hbar})^n \int_{t_0}^{t} d\tau_n \int_{t_0}^{\tau_n} d\tau_{n-1} \cdots \int_{t_0}^{\tau_2} d\tau_1 E(\tau_n) E(\tau_{n-1}) \cdots \cdots E(\tau_1) \\ & \langle \hat{\mu}(t) [\hat{\mu}(\tau_n), [\hat{\mu}(\tau_{n-1}), \cdots [\hat{\mu}(\tau_1), \rho(t_0)] \cdots]] \rangle\end{aligned} \tag{35}$$

where $\hat{\mu}$ from equation 34 in the Schrödinger picture has been converted to the interaction picture $\hat{\mu}(t)$. It is also noted that all $\hat{\mu}(\tau)$ terms are within the commutator, but the $\hat{\mu}(t)$ interaction is outside the commutator. Under the assumption that $\rho(t_0)$ is at equilibrium, there is

no time evolution until τ_1 where the first interaction occurs; thus, equation (35) can be rewritten with t_0 approaching $-\infty$:

$$P^{(n)}(t) = - \quad (-\frac{i}{\hbar})^n \int_{-\infty}^{t} d\tau_n \int_{-\infty}^{\tau_n} d\tau_{n-1} \cdots \int_{-\infty}^{\tau_2} d\tau_1 E(\tau_n)E(\tau_{n-1}) \cdots \cdots E(\tau_1)$$
$$\langle \hat{\mu}(t)[\hat{\mu}(\tau_n), [\hat{\mu}(\tau_{n-1}), \cdots [\hat{\mu}(\tau_1), \rho(-\infty)] \cdots]]\rangle \tag{36}$$

In an analogous way to the interaction picture, it is useful to define these integrals in terms of time intervals, which can be controlled experimentally, rather than points in time.

$$\begin{gathered} \tau_1 = 0 \\ t_1 = \tau_2 - \tau_1 \\ t_2 = \tau_3 - \tau_2 \\ \vdots \\ t_n = t - \tau_n \end{gathered} \tag{37}$$

Changing the notation leads to the integrals of equation (36), which are defined from 0 to ∞, and the nth-order polarization is:

$$P^{(n)}(t) = \quad -(-\frac{i}{\hbar})^n \int_0^{\infty} dt_n \int_0^{\infty} dt_{n-1} \cdots \int_0^{\infty} dt_1$$
$$E(t - t_n)E(t - t_n - t_{n-1}) \cdots \cdots E(t - t_n - t_{n-1} - \cdots - t_1)$$
$$\langle \hat{\mu}(t_n + t_{n-1} + \cdots + t_1)[\hat{\mu}(t_{n-1} + \cdots + t_1), \cdots [\hat{\mu}(0), \rho(-\infty)] \cdots]\rangle \tag{38}$$

and more generally, the *n*th-order macroscopic polarization is a convolution of n electric fields with the *n*th-order response function, $R^{(n)}(t_n, \cdots, t_1)$, which collects the perturbations of the density matrix by dipole operator:

$$P^{(n)}(t) = \int_0^{\infty} dt_n \int_0^{\infty} dt_{n-1} \cdots \int_0^{\infty} dt_1$$
$$E(t - t_n)E(t - t_n - t_{n-1}) \cdots \cdots E(t - t_n - \cdots - t_1)R^{(n)}(t_n, \cdots, t_1) \tag{39}$$

with the response function:

$$R^{(n)}(t_n,\cdots,t_1) = -(-\frac{i}{\hbar})^n\langle\hat{\mu}(t_n+\cdots+t_1)[\hat{\mu}(t_{n-1}+\cdots+t_1),\cdots[\hat{\mu}(0),\rho(-\infty)]\cdots]\rangle \tag{40}$$

Careful observation of the response function highlights the importance of the $\hat{\mu}(t_n+\cdots+t_1)$ interaction, which as previously noted is excluded from the commutator. The final dipole operator acts on the density matrix created by the other interactions, resulting in an emitted light field. For linear absorption, the first-order nonlinear response is:

$$P^{(1)}(t) = \int_0^\infty dt_1 E(t-t_1)R^{(1)}(t_1) \tag{41}$$

with the linear response function defined as:

$$R^{(1)}(t_1) \propto i\langle\hat{\mu}(t_1)[\hat{\mu}(0),\rho(-\infty)]\rangle \tag{42}$$

In nonlinear spectroscopy, three laser pulses are incident on the sample, and the polarization (or third-order nonlinear response) is the convolution of three electric fields and the third-order response function:

$$\begin{aligned} P^{(3)}(t) \propto \quad & \int_0^\infty dt_3 \int_0^\infty dt_2 \int_0^\infty dt_1 E_3(t-t_3)E_2(t-t_3-t_2) \\ & \cdot E_1(t-t_3-t_2-t_1)R^{(3)}(t_3,t_2,t_1) \end{aligned} \tag{43}$$

with

$$R^{(3)}(t_3,t_2,t_1) \propto -i\langle\hat{\mu}(t_3+t_2+t_1)[\hat{\mu}(t_2+t_1),[\hat{\mu}(t_1),[\hat{\mu}(0),\rho(-\infty)]]]\rangle \tag{44}$$

2.2. Constructing Feynman diagrams

2.2.1. Linear response theory and the rotating wave approximation

In principle, the macroscopic polarization is identical to the molecular response if the envelope of the electric field $E'(t)$ is a delta function. In practice, this does not hold because any

experimentally generated pulse has a finite width, such that $E'(t) \neq \delta(t)$. However, similar to the perturbative expansion of $\rho(t)$, by assuming the potential $\hat{W}(t)$ is a weak interaction, the macroscopic polarization and electric field strength scale linearly; this is known as *linear response theory.* If linear response theory applies, the pulse envelope $E'(t)$ for a pulse of finite width can be approximated as the sum of several δ-functions, and the macroscopic polarization can be calculated as:

$$P^{(1)}(t) = \int_0^\infty dt_1 E(t - t_1) R^{(1)}(t_1) \tag{45}$$

which only differs from equation (41) by inclusion of the pulse envelope. The pulse envelope is related to the electric field by:

$$2E'(t)\cos(\omega t) = E'(t)(e^{-i\omega t} + e^{+i\omega t}) = E(t) + E^*(t) \tag{46}$$

and substituting the electric field into equation (45) relates the polarization to both terms of the electric field:

$$P^{(1)}(t) = \int_0^\infty dt_1 (E(t - t_1) + E^*(t - t_1)) R^{(1)}(t_1) \tag{47}$$

The linear response function is given in its nested commutator form in equation (42), but the expanded notation is provided here for the sake of clarity:

$$\begin{aligned} R^{(1)}(t_1) \quad &= i\langle \mu(t_1)\mu(0)\rho(-\infty)\rangle - i\langle \mu(t_1)\rho(-\infty)\mu(0)\rangle \\ &= i\langle \mu(t_1)\mu(0)\rho(-\infty)\rangle - i\langle \rho(-\infty)\mu(0)\mu(t_1)\rangle \end{aligned} \tag{48}$$

where the second term is the trace $\langle \mu(t_1)\rho^{(1)}\rangle$ of the macroscopic polarization and has undergone cyclic permutation to form a symmetric equation. This form of the equation leads to a straightforward interpretation of the dipole operator acting twice on the *ket* side of $\rho(-\infty)$ in the first term and twice on the *bra* side in the second term. In the development of Feynman

diagrams, this symmetry will prove critical, but first, a minor correction must be made to the linear response function, which has thus far been written without the coherence dephasing term. Looking at only the first term of equation (48) for simplicity:

$$R^{(1)}(t_1) = i\langle\mu(t_1)\mu(0)\rho(-\infty)\rangle = ie^{-i\omega_{01}t_1}e^{-t_1/T_2} \tag{49}$$

Assuming the laser field is resonant with the vibrational transition $\omega = \omega_0$, the polarization for the *ket* interaction is:

$$P^{(1)}(t) \propto ie^{-i\omega t}\int_0^\infty dt_1 E'(t-t_1)e^{-t_1/T_2} + ie^{+i\omega t}\int_0^\infty dt_1 E'(t-t_1)e^{-t_1/T_2}e^{-i2\omega t_1} \tag{50}$$

The second term has two exponential functions dependent on t_1, which causes it to oscillate much faster than the first term; this makes the second integral negligibly small. By making use of the rotating wave approximation, the highly oscillating term is disregarded entirely, simplifying equation (50) to:

$$P^{(1)}(t) = \int_0^\infty dt_1 E(t-t_1)R^{(1)}(t_1) \tag{51}$$

Analyzing equations (49) and (51) together, the macroscopic polarization depends on the time ordering of the interactions, whether the dipole operator acts on the *ket* or *bra* side of $\rho(-\infty)$, and whether the interacting field is $E(t) \propto e^{-i\omega t}$ or its complex conjugate $E^*(t) \propto e^{+i\omega t}$. Algebraically, it is also of pivotal importance to track the state (population states and coherence states) of the density matrix through each interaction. To simplify the organization of all these details, Feynman diagrams are an outstanding tool; these will be developed in the next subchapter, alongside a matrix representation of the evolution of $\rho(-\infty)$ perturbed by interactions with the electric field.

2.2.2. Feynman diagrams for the linear response

The matrix elements of $\rho(-\infty)$ were introduced in equation (15) for a simple system with a ground state $|0\rangle$ and excited state $|1\rangle$. To describe the evolution of the population and coherence states under laser field interactions, it is useful to view the density matrix and dipole operator as interacting matrices:

$$\rho(-\infty) = \begin{pmatrix} 1 & 0 \\ 0 & 0 \end{pmatrix}$$

$$\mu = \begin{pmatrix} 0 & 1 \\ 1 & 0 \end{pmatrix} \tag{52}$$

Considering only the interaction of $\mu(0)$ on the *ket* side of $\rho(-\infty)$ gives a coherence of ρ_{10}:

$$i\mu(0)\rho(-\infty) = i\begin{pmatrix} 0 & 1 \\ 1 & 0 \end{pmatrix}\begin{pmatrix} 1 & 0 \\ 0 & 0 \end{pmatrix} = \begin{pmatrix} 0 & 0 \\ i & 0 \end{pmatrix} \tag{53}$$

After the laser pulse, ρ evolves in time according to the influence of H_0, which is $e^{-i\omega_{01}t}$ as only the $E(t)$ term survives the rotating wave approximation. The density matrix after the first interaction is:

$$ie^{-i\omega_{01}t_1}\mu(0)\rho(-\infty) = \begin{pmatrix} 0 & 0 \\ ie^{-i\omega_{01}t_1} & 0 \end{pmatrix} \tag{54}$$

Furthermore, the interaction of $\mu(0)$ on the *bra* side of $\rho(-\infty)$ gives a coherence of ρ_{01}:

$$\begin{pmatrix} 1 & 0 \\ 0 & 0 \end{pmatrix} \overset{-i\rho(-\infty)\mu(0)}{\longrightarrow} \begin{pmatrix} 0 & -i \\ 0 & 0 \end{pmatrix} \overset{-i\rho(-\infty)\mu(0)e^{+i\omega_{01}t_1}}{\longrightarrow} \begin{pmatrix} 0 & -ie^{+i\omega_{01}t_1} \\ 0 & 0 \end{pmatrix} \tag{55}$$

such that the density matrix after the first interaction is:

$$\rho^{(1)} = \begin{pmatrix} 0 & -ie^{+i\omega_{01}t_1} \\ ie^{-i\omega_{01}t_1} & 0 \end{pmatrix} \tag{56}$$

This density matrix $\rho^{(1)}$ describes the time evolution due to the laser field interactions; it is not the full density matrix, which includes the unperturbed density matrix $\rho^{(0)}$, the matrix representing all the population in the ground state. Bearing this distinction in mind, $\rho^{(0)}$ has no time-dependence, so the macroscopic polarization, which develops only due to the vibrational coherences, can be described using only $\rho^{(1)}$. Comparing the development of $\rho^{(1)}$ with the definition of $R^{(1)}(t_1)$ given in equation (42) or equation (48), the $\mu(t_1)$ interaction on the density matrix has not been considered. Recalling the definition of the dipole operator (equation 52), it follows that the final laser interaction forces the system to emit a coherent field and returns $\rho^{(1)}$ to the ground state:

$$\begin{aligned} i\mu(t_1)e^{-i\omega_{01}t_1}\mu(0)\rho(-\infty) &= \begin{pmatrix} 0 & 1 \\ 1 & 0 \end{pmatrix}\begin{pmatrix} 0 & 0 \\ ie^{-i\omega_{01}t_1} & 0 \end{pmatrix} \\ &= \begin{pmatrix} ie^{-i\omega_{01}t_1} & 0 \\ 0 & 0 \end{pmatrix} \end{aligned} \tag{57}$$

This interaction occurs through the ρ_{10} coherence, and a similar matrix could be developed through the ρ_{01} coherence:

$$\begin{aligned} -i\rho(-\infty)\mu(0)e^{+i\omega_{01}t_1}\mu(t_1) &= \begin{pmatrix} 0 & 0 \\ -ie^{+i\omega_{01}t_1} & 0 \end{pmatrix}\begin{pmatrix} 0 & 1 \\ 1 & 0 \end{pmatrix} \\ &= \begin{pmatrix} -ie^{+i\omega_{01}t_1} & 0 \\ 0 & 0 \end{pmatrix} \end{aligned} \tag{58}$$

The definition of $R^{(1)}(t_1)$ from equation (48) can be written as the difference of two traces:

$$R^{(1)}(t_1) = iTr[\mu(t_1)\mu(0)\rho(-\infty)] - i\,Tr[\mu(t_1)\rho(-\infty)\mu(0)] = R_1 - R_1^* \tag{59}$$

and taking the traces of equations (57) and (58) gives the linear response functions in terms of $E(t)$ and $E^*(t)$:

$$R_1 = -ie^{+i\omega_{01}t_1}$$

$$R_1^* = ie^{-i\omega_{01}t_1} \tag{60}$$

which passes through the ρ_{01} and ρ_{10} coherences:

$$\begin{aligned}(\rho_{00} \rightarrow \rho_{01} \rightarrow \rho_{00}) \quad &\equiv (|0\rangle\langle 0| \rightarrow |0\rangle\langle 1| \rightarrow |0\rangle\langle 0|) \\ (\rho_{00} \rightarrow \rho_{10} \rightarrow \rho_{00}) \quad &\equiv (|0\rangle\langle 0| \rightarrow |1\rangle\langle 0| \rightarrow |0\rangle\langle 0|)\end{aligned} \tag{61}$$

With all the proper pieces finally in play, Feynman diagrams can be developed for the linear response described above, where both of R_1 and R_1^* are represented by the Feynman diagrams in Figure 2.1.

First examining the diagram for R_1, the system starts out in the ground state $\rho = |0\rangle\langle 0|$. At time t=0, the dipole operator $\mu(0)$ acts on the *ket* of the density matrix, generating a $|0\rangle\langle 1|$ coherence; this is represented as the black arrow pointed toward the system. The density matrix propagates under $\hat{H}_0$ until time $t=t_1$, when the $\mu(t_1)$ forces the emission of the signal, depicted as the dashed arrow, returning the density matrix to the ground state. The same logic can be used to analyze the Feynman diagram for R_1^*, where $\mu(0)$ operates on the *bra* instead, creating a $|1\rangle\langle 0|$ coherence. One important distinction should be made regarding the arrows, which serve a dual role in the Feynman diagrams. Arrows pointed to the system describe an excitation, and arrows pointed away depict emission. However, the direction of the arrows provides separate information on which electric field, $E(t)$ or $E^*(t)$, interacts with the density matrix at each time. $E(t)$ is denoted by arrows pointing right and $E^*(t)$ by arrows pointing left. Paired with the rotating wave approximation, this leads to a straightforward interpretation of the interactions. $E(t)$, an arrow pointing right, excites *kets* and stimulates emission of *bras*; $E^*(t)$, for which arrows point left, excite *bras* and stimulate emission of *kets*. Feynman diagrams are convenient tools for organizing the many parameters that dictate the time evolution of the density matrix,

and these pictures become even more useful for tracking the third-order nonlinear response. First, however, one additional wrinkle is introduced by multiple laser field excitations: the direction of the emitted field must be considered.

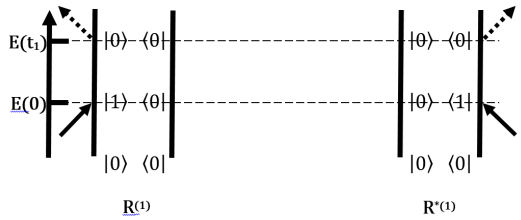

Figure 2.1. Feynman diagrams for the linear response functions R_1 and R_1^*

2.2.3. Phase matching to collect data

The linear response function, $R^{(1)}(t_1)$ is comprised of two components, R_1 and R_1^*, due to the interaction of the dipole operator $\mu(0)$ on the *ket* or *bra* of the density matrix, respectively; these are the only Feynman diagrams that survive the rotating wave approximation. For nonlinear spectroscopy, multiple laser field interactions occur, such that several dipole operators interact with both sides of the density matrix and produce 8 Feynman diagrams (considering only those that survive the rotating wave approximation), which results in a complicated signal of overlapping components, each with different information. To distinguish between the different response function components, it is convenient to reconsider the definition of the electric field introduced in equation (2), recognizing now that this reduced definition excludes contributions from the wavevector $\boldsymbol{k}$ and phase ϕ. Under these considerations, $E(t)$ becomes:

$$E(t) = E'(t)\cos(\boldsymbol{k}\cdot\vec{r} - \omega t + \phi) \tag{62}$$

Recalling now the rotating wave approximation, which dictates the frequency $e^{-i\omega t}$ or $e^{+i\omega t}$ related to the $E(t)$ and $E^*(t)$ interactions with the density matrix, it is seen that $\boldsymbol{k}$ and ϕ are also fixed in similar fashion, such that $E(t)$ and $E^*(t)$:

$$E(t) \propto e^{-i\omega t + i\phi + i\boldsymbol{k}\cdot\vec{r}}$$

$$E^*(t) \propto e^{+i\omega t - i\phi - i\boldsymbol{k}\cdot\vec{r}} \tag{63}$$

Considering now the third order polarization from two different pathways, producing the response components R_1 and R_4 with pulse envelope E_n'':

$$P_1^{(3)}(t) \propto e^{i(-\boldsymbol{k_1}+\boldsymbol{k_2}+\boldsymbol{k_3})\cdot\vec{r}} e^{i(-\phi_1+\phi_2+\phi_3)} \int_0^\infty dt_3 \int_0^\infty dt_2 \int_0^\infty dt_1 E_3''(t-t_3) \cdot E_2''(t-t_3-t_2) E_1''^*(t-t_3-t_2-t_1) R_1(t_3,t_2,t_1)$$

$$P_4^{(3)}(t) \propto e^{i(+\boldsymbol{k_1}-\boldsymbol{k_2}-\boldsymbol{k_3})\cdot\vec{r}} e^{i(+\phi_1-\phi_2+\phi_3)} \int_0^\infty dt_3 \int_0^\infty dt_2 \int_0^\infty dt_1 E_3''(t-t_3) \cdot E_2''^*(t-t_3-t_2) E_1''(t-t_3-t_2-t_1) R_4(t_3,t_2,t_1) \tag{64}$$

the wavevectors are different, causing the signals each to emit in a different direction. By placing a detector in the matching direction ($-\boldsymbol{k_1}+\boldsymbol{k_2}+\boldsymbol{k_3}$ for R_1), one signal can be selectively measured. Figure 2.2 shows how two emitted signals with different wavevectors separate in space.

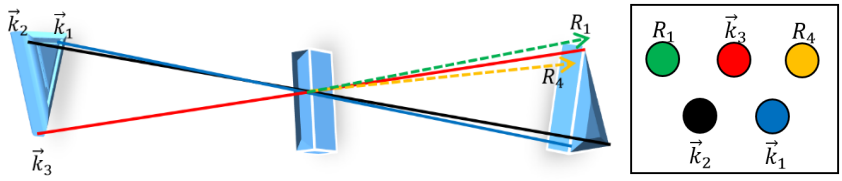

Figure 2.2. Illustration of the phase matching direction in 3D and 2D. Three 3 laser pulse in the $\boldsymbol{k_1}, \boldsymbol{k_2}, \boldsymbol{k_3}$ directions are incident on the sample. The signals R_1 and R_4 are emitted in different directions based on their wavevectors, $-\boldsymbol{k_1}+\boldsymbol{k_2}+\boldsymbol{k_3}$ and $+\boldsymbol{k_1}-\boldsymbol{k_2}-\boldsymbol{k_3}$, respectively. The 2D picture shows the path of the beams after the same, as they would arrive on a detector.

2.2.4. Rephasing and non-rephasing signals

The pathways R_1 and R_4 from which the polarization was developed are the two signals measured by two-dimensional infrared spectroscopy (2DIR), the rephrasing pulse sequence in the $-\boldsymbol{k_1}+\boldsymbol{k_2}+\boldsymbol{k_3}$ direction and the non-rephasing pulse sequence in the $+\boldsymbol{k_1}-\boldsymbol{k_2}-\boldsymbol{k_3}$

direction, respectively. To understand these terms, the full time evolution of ρ as it interacts with the laser pulses is displayed for R_4 in equation 65 and for R_1 in equation 66:

$$\begin{pmatrix}1 & 0\\ 0 & 0\end{pmatrix} \overset{i\mu_0\rho}{\longrightarrow} \begin{pmatrix}0 & 0\\ i & 0\end{pmatrix} \overset{i_1}{\longrightarrow} \begin{pmatrix}0 & 0\\ ie^{-i\omega_{01}t_1} & 0\end{pmatrix} \overset{i\mu_0\rho\mu_1}{\longrightarrow} \begin{pmatrix}0 & 0\\ 0 & ie^{-i\omega_{01}t_1}\end{pmatrix} \overset{i\mu_0\rho\mu_1\mu_2}{\longrightarrow} \begin{pmatrix}0 & 0\\ ie^{-i\omega_{01}t_1} & 0\end{pmatrix} \overset{t_3}{\longrightarrow} \begin{pmatrix}0 & 0\\ ie^{-i\omega_{01}(t_3+t_1)} & 0\end{pmatrix} \overset{i\langle\mu_3\mu_0\rho\mu_1\mu_2\rangle}{\longrightarrow} ie^{-i\omega_{01}(t_3+t_1)} \tag{65}$$

$$\begin{pmatrix}1 & 0\\ 0 & 0\end{pmatrix} \overset{i\rho\mu_0}{\longrightarrow} \begin{pmatrix}0 & i\\ 0 & 0\end{pmatrix} \overset{t_1}{\longrightarrow} \begin{pmatrix}0 & ie^{+i\omega_{01}t_1}\\ 0 & 0\end{pmatrix} \overset{i\mu_1\rho\mu_0}{\longrightarrow} \begin{pmatrix}0 & 0\\ 0 & ie^{+i\omega_{01}t_1}\end{pmatrix} \overset{i\mu_1\rho\mu_0\mu_2}{\longrightarrow} \begin{pmatrix}0 & 0\\ ie^{+i\omega_{01}t_1} & 0\end{pmatrix} \overset{t_3}{\longrightarrow} \begin{pmatrix}0 & 0\\ ie^{-i\omega_{01}(t_3-t_1)} & 0\end{pmatrix} \overset{i\langle\mu_3\mu_1\rho\mu_0\mu_2\rangle}{\longrightarrow} ie^{-i\omega_{01}(t_3-t_1)} \tag{66}$$

For R_4, μ_0 acts on the *ket* of ρ and makes a ρ_{10} coherence. For R_1, μ_0 instead acts on the *bra* of ρ and makes a ρ_{01} coherence. Interaction with the second laser pulse μ_1 then puts both systems in the excited state. The critical difference comes from the interaction with the third pulse μ_2. This results in a ρ_{10} coherence for both systems, returning R_4 to the same state as directly after the initial field interaction μ_0. Conversely, R_1 was initially put in a ρ_{01} coherence, so the interaction with μ_2 also converts the coherence to its converse conjugate. This distinction has significant consequences for the dephasing of vibrational coherences with time. Each molecule can be envisioned as a dipole vector rotating around the origin at its vibrational frequency, ω. Any changes in the environment, which change ω, will also alter the rotation of the dipole, leading to some dipoles rotating slower and some rotating faster than the average, a pictorial portrayal of dephasing. Coherences are prepared by interactions with a laser field, and dephasing occurs in the time period directly following. Following ρ for R_4, the coherences dephase following pulses μ_0 and μ_2. The density matrix evolution is more interesting for R_1; since the

interaction with μ_2 converts the ρ_{10} term to the complex conjugate, the frequencies are inverted. This results in the faster molecules now dispersed behind the average and the slower molecules positioned in front. As time passes, when dephasing would normally occur, the faster molecules get closer to the average, and the average precessing molecules catch up to the slowest frequencies. At time t_3, all the different molecules will be overlapped in frequency, again generating a vibrational coherence. They have been rephased, and the macroscopic polarization is emitted as the photon echo signal, which contains information on the dephasing of the system. This photon echo signal is the key experimental observable of 2DIR spectroscopy, allowing the study of changes in frequency on ultrafast timescales, and measuring the rephasing and non-rephasing signals allows the isolation of the photon echo signal. As already presented, this creates a problem: the R_1 and R_4 signals emit in different directions (due to their different wavevectors). This could in principle be solved by a second detector in the $+\boldsymbol{k_1} - \boldsymbol{k_2} - \boldsymbol{k_3}$ direction, but a cheaper, more elegant solution emerges from understanding the time ordering of the laser pulses. The final two laser fields interaction for R_1, $\langle \mu_3 \mu_1 \rho(-\infty) \mu_0 \mu_2 \rangle$, and R_4, $\langle \mu_3 \mu_0 \rho(-\infty) \mu_1 \mu_2 \rangle$, are the same. Moreover, the first two interactions only differ by when they occur; the electric fields and interactions with the *bra* or *ket* are otherwise indistinguishable. This means the non-rephasing signal R_4 emitted in the $+\boldsymbol{k_1} - \boldsymbol{k_2} - \boldsymbol{k_3}$ is identical to the signal emitted in the $-\boldsymbol{k_1} + \boldsymbol{k_2} + \boldsymbol{k_3}$ direction if $\boldsymbol{k_2}$ preceeds $\boldsymbol{k_1}$. If the time ordering of pulses $\boldsymbol{k_1}$ and $\boldsymbol{k_2}$ is inversed, the rephrasing and non-rephasing spectra for each system can be measured in the same direction with a single detector. The third-order response components R_1 and R_4 can therefore be written to include dephasing of both coherences as well as population relaxation, differing only by the frequency of the initial coherence:

$$R_1(t_1,t_2,t_3) \propto i\mu_{01}^4 e^{+i\omega_{01}t_1} e^{-t_1/T_2} e^{-t_2/T_1} e^{-i\omega_{01}t_3} e^{-t_3/T_2}$$

$$R_4(t_1,t_2,t_3) \propto i\mu_{01}^4 e^{-i\omega_{01}t_1} e^{-t_1/T_2} e^{-t_2/T_1} e^{-i\omega_{01}t_3} e^{-t_3/T_2} \quad (67)$$

2.2.5. Third-order Feynman diagrams

With the understanding that both the rephasing ($-\boldsymbol{k_1}+\boldsymbol{k_2}+\boldsymbol{k_3}$) and non-rephasing ($+\boldsymbol{k_1}-\boldsymbol{k_2}-\boldsymbol{k_3}$) data must be measured, third-order Feynman diagrams can be developed for all Feynman pathways. To begin, the rules for drawing Feynman diagrams, which have been described in relation to the linear picture, are detailed:

1. Time runs from the bottom to the top of the diagram. The solid black line on the left is the time evolution of the *ket,* and the solid line on the right is the time evolution of the *bra*.

2. Arrows toward the system represent excitation (absorption); arrows pointed away from the system indicate emission. The final emission arrow, which returns the system to the ground state, is dashed. Due to the rotating wave approximation, arrows pointing toward the system always represent an up-climbing of the associated *bra* or *ket*.

3. The sign of the diagram $(-1)^n$ varies with n, the number of *bra* interactions, due to the definition of the commutator. The final field interaction is not included in the commutator and should not be counted as part of n.

4. An arrow pointing right depicts an electric field with $e^{-i\omega t+i\phi+i\mathbf{k}\cdot\vec{r}}$; an arrow pointing right has opposite frequency, phase, and wavevector, $e^{+i\omega t-i\phi-i\mathbf{k}\cdot\vec{r}}$

5. The final interaction must end in a population state, ρ_{nn}; for nonlinear spectroscopy, this does not have to be the ground state.

This established, the evolution of the density matrix catalogued in equation (66) can be used to sketch the example Feynman diagram for R_1. The first laser interaction μ_0, an $E^*(t)$ field, acts on the *bra* of ρ, producing a ρ_{01} coherence; the coherence then decays during t_1. Then μ_1, the

second laser interaction, creates a population state ρ_{11} via an $E(t)$ electric field interaction with the *ket* of ρ (population relaxation has not been considered yet for this system; the next section will develop full Feynman diagrams considering population relaxation and a three state system). Next, the third laser pulse μ_2 interacts with the *bra* via an $E(t)$ field, turning the population state into a ρ_{10} coherence. Finally, the last field interaction $E^*(t)$ interacts with the *ket* through the dipole operator μ_3, emitting the signal and returning the system to its ground state. Each interaction presented is charted beautifully through the Feynman diagram with the direction of the arrows showing the signs of the interacting electric fields, the state of the system represented as a *ket* and *bra*, and the time chronicled along the leftmost axis. The third-order Feynman diagram for the R_4 pathway or any other combination of interactions could be developed similarly. Six Feynman diagrams for the third-order polarization are plotted in Figure 2.3 (the other diagrams either do not survive the rotating wave approximation, pass through a ρ_{20} or ρ_{02} state, or are just the complex conjugate of one of the six graphed spectra). Examining the time axis of Figure 2.3, the timescales have been rewritten in terms of 3 time intervals, similar to the definition in the interaction picture: τ, the coherence time between μ_0 and μ_1; T, the population time between μ_1 and μ_2; and t, the coherence time between μ_2 and μ_3. These intervals define the experimentally-controlled time delay between pulses and allow the simultaneous measurement of structural changes and dynamics processes, as will be derived in a subsequent section. The laser pulses can also be defined in terms of these intervals: μ_0, $\mu_1(\tau)$, $\mu_2(\tau + T)$, and $\mu_3(\tau + T + t)$.

Two interesting points should be noted regarding the R_3 and R_6 pathways. If the R_1, R_2, R_4, and R_5 signals were measured (excluding R_3 and R_6), the resulting absorptive spectrum would have a single peak in the 2DIR spectrum. As shown in the Feynman diagrams, the R_3 and

R_6 pathways both achieve a $|2\rangle\langle 1|$ coherence state, which involves the second excited state. Due to the anharmonicity of the vibrational potential, the frequency of the $|0\rangle$ to $|1\rangle$ transition is smaller than the $|1\rangle$ to $|2\rangle$ transition, and the information collected from the ρ_{21} coherence appears as a separate peak in the 2DIR spectra at a lower frequency. Thus, the pair of diagonal peaks observed in a typical 2DIR spectrum originate from the R_3 and R_6 pathways. Additionally, by the third rule for drawing Feynman diagrams, both the R_3 and R_6 pathways have a negative sign, while the other pathways are all positive. This leads to the notation of the low-frequency diagonal peak derived from R_3 and R_6 as the "negative" peak; in all spectra, this peak will be presented as blue with the "positive" diagonal peak in red.

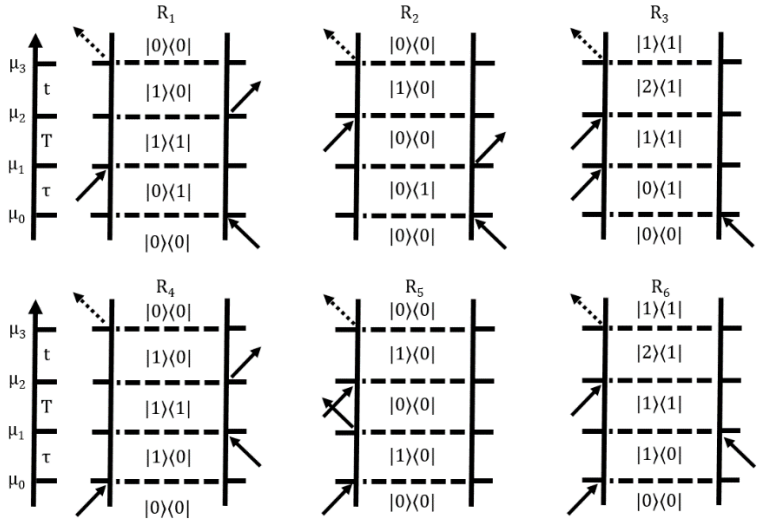

Figure 2.3. Third-order Feynman diagrams for the rephrasing (top) and non-rephasing (bottom) Feynman diagrams of a three-state system.

2.3. Lineshapes in nonlinear spectroscopy

2.3.1. Kubo theory and the cumulant expansion

Kubo theory describes the dephasing of vibrational transitions semiclassically, in terms of quantum mechanical vibrational transitions and classical solvent molecules.[136] Simply, the frequency of a vibrational transition ω for a single oscillator is time-dependent, since the solvent molecules perturb the oscillator over time. Each oscillator in an ensemble experiences different

time-dependent interactions with the solvent, which is the origin of dephasing. Dephasing has until now been explicated added as an $e^{-\frac{t}{T_2}}$ term to the Liouville-von Neumann equation, which was derived as equation (29). To derive an expression for dephasing, the time evolution for a single molecule in a ρ_{01} coherence is:

$$\dot{\rho}_{01}(t) = -i\omega_{01}(t)\rho_{01}(t) \tag{68}$$

and the density matrix in this during this coherence is found by integration:

$$\rho_{01}(t) \propto \exp(-i\int_0^t \omega_{01}(\tau)d\tau) \tag{69}$$

and the average density matrix can be considered, accounting for all the molecules interacting with the solvent bath by taking the ensemble average:

$$\rho_{01}(t) \propto < \exp(-i\int_0^t \omega_{01}(\tau)d\tau) > \tag{70}$$

If the time-dependent frequency is decomposed into an average component ω_{01} and a small time-dependent fluctuation $\delta\omega_{01}(t)$, the average density matrix becomes:

$$\rho_{01}(\mathrm{t}) \propto e^{-i\omega_{01}t} < \exp(-i\int_0^t \delta\omega_{01}(\tau)d\tau) > \tag{71}$$

Since the density matrix has been decomposed into a time-independent average and the time-dependent fluctuation describing dephasing, this is just part of the linear response function:

$$R^{(1)}(t_1) = i\mu_{01}^2 e^{-i\omega_{01}t_1} < \exp -i\int_0^{t_1} d\tau\delta\omega_{01}(\tau) > \tag{72}$$

The transition dipole moment in equation (72) is not included in the average, reflecting the Condon approximation derived from the Franck-Condon principle. The Condon approximation states that the solvent motions occur on a much slower time scale than the frequency

fluctuations, such that the transition dipole moment is time-independent on the time scale of the frequency fluctuations. Expanding equation (71) as a cumulant expansion gives:

$$< \exp(-i\int_0^t d\tau \delta\omega_{01}(\tau)) >= \quad 1 - i\int_0^t d\tau \langle \delta\omega_{01}(\tau)\rangle \\ -\frac{1}{2}\int_0^t \int_0^t d\tau' d\tau'' \langle \delta\omega_{01}(\tau')\delta\omega_{01}(\tau'')\rangle + \cdots \tag{73}$$

and the cumulants are rewritten and expanded in terms of an arbitrary function $g(t)$ which consolidates the fluctuations of ω_{01}:

$$< \exp(-i\int_0^t d\tau \delta\omega_{01}(\tau)) > \equiv e^{-g(t)} = 1 - g(t) + \frac{1}{2}g^2(t) + \cdots$$

$$e^{-g(t)} = 1 - (g_1(t) + g_2(t) + \cdots) + \frac{1}{2}(g_1(t) + g_2(t) + \cdots)^2 + \cdots \tag{74}$$

The first cumulant is the average, so $g_1(t) = 0$. The second cumulant $g_2(t)$ is the variance, and integration of equation (74) gives $g(t)$, a lineshape function:

$$g(t) = \frac{1}{2}\int_0^t \int_0^t d\tau' d\tau'' \langle \delta\omega_{01}(\tau')\delta\omega_{01}(\tau'')\rangle = \int_0^t \int_0^{\tau'} d\tau' d\tau'' \langle \delta\omega_{01}(\tau'')\delta\omega_{01}(0)\rangle \tag{75}$$

The average now contains only the integrand. This average is the frequency-frequency correlation function, $C(t)$, which formally describes coherence dephasing. This function is responsible for the shape of peaks in 2DIR, which will be detailed in the next subchapter.

2.3.2. Homogenous and inhomogeneous broadening

Before continuing, it is worthwhile to address the simple relationship between the time constants for homogenous dephasing T_2, population relaxation T_1, and pure dephasing T_2^* (caused by environmental fluctuations):

$$\frac{1}{T_2} = \frac{1}{2T_1} + \frac{1}{T_2^*} \tag{76}$$

The frequency-frequency correlation function is rewritten in the notation introduced in subsection 2.2.5, where time intervals τ is the initial coherence time, T is the population time, and t is the final coherence time:

$$C(t) = \langle \delta\omega_{01}(t)\delta\omega_{01}(0)\rangle \tag{77}$$

Now possessing the lineshape function $g(t)$, the upper and lower limits for $C(t)$ will be explored. Again pulling from Kubo's stochastic theory, $C(t)$ is written in terms of a fluctuation amplitude Δω and correlation time τ

$$\langle \delta\omega(t)\delta\omega(0)\rangle = \Delta\omega^2 e^{-\frac{t}{\tau}} \tag{78}$$

and the Kubo lineshape function is developed from the double integral of equation (78):

$$g(t) = \Delta\omega^2\tau^2[e^{-\frac{t}{\tau}} + \frac{t}{\tau} - 1] \tag{79}$$

The homogeneous limit occurs when the frequency fluctuations happen very quickly relative to time *t*. In this case, the time constant τ is very small, and the product $\Delta\omega \cdot \tau \ll 1$. Examining $g(t)$, the exponential goes to 0, and the $\frac{t}{\tau}$ term simplifies to just t, such that the lineshape function simplifies to:

$$g(t) = \Delta\omega^2 \cdot \tau \cdot t \equiv \frac{t}{T_2^*} \tag{80}$$

where the pure dephasing time T_2^* is just the reciprocal of $\Delta\omega^2\tau$. The absorption $A(\omega)$ can be calculated from the definition of the linear response by substituting $g(t)$:

$$R^{(1)}(t) = i\mu_{01}^2 e^{-i\omega_{01}t}e^{-g(t)} \tag{81}$$

$$A(\omega) \propto R\int_0^\infty e^{i(\omega-\omega_{01})t}e^{-g(t)}dt = R\int_0^\infty e^{i(\omega-\omega_{01})t}e^{-\frac{t}{T_2^*}}$$
$$= \frac{\frac{1}{T_2^*}}{(\omega-\omega_{01})^2 + \frac{1}{T_2^{*2}}} \tag{82}$$

Two important points regarding the homogenous limit are here noted. First, the homogeneous limit produces a Lorentzian lineshape. Second, the linewidth of the Lorentzian is $\frac{1}{T_2^*}$, and by rearranging the definition of T_2^*, it can be shown that the linewidth is smaller than the frequency distribution. This results in motional narrowing, where the frequencies fluctuate so fast that the average lineshape is narrower than the distribution of frequencies.

Conversely, if the frequency fluctuations are very slow, the inhomogeneous limit applies, wherein $\Delta\omega \cdot \tau \gg 1$. The time constant τ is necessarily large, so the $\frac{t}{\tau}$ term of equation (79) goes to 0. Meanwhile, the exponential term of equation expands as $1 - \frac{t}{\tau} + \frac{t^2}{2\tau^2}$..., so the τ terms cancel, leaving $g(t) = \Delta\omega^2 \cdot \frac{t^2}{2}$, which does not depend on the correlation time τ. Thus the absorption in the inhomogeneous limit is:

$$A(\omega) \propto R\int_0^\infty e^{i(\omega-\omega_{01})t}e^{-g(t)}dt = R\int_0^\infty e^{i(\omega-\omega_{01})t}e^{-\frac{\Delta\omega^2}{2}t^2}dt$$
$$\propto e^{-\frac{(\omega-\omega_0)^2}{2\Delta\omega^2}} \tag{83}$$

which is a Gaussian function. As noted earlier, the importance of these lineshapes lies in the Voigt shape frequently observed for linear and nonlinear infrared spectra. The Voigt function is a convolution of a Lorentzian and a Gaussian, implying contributions from both to the lineshape. The 2DIR spectra therefore exists between the homogenous and inhomogeneous limits, which gives rise to spectral diffusion. Between these limits, the frequency fluctuations are slow enough that if multiple measurements of the frequency fluctuations are made across a time delay (T, the

population time in the convention established prior), the loss of correlation can be observed. More quantitatively, two metrics are commonly used in the following works to characterize the spectral diffusion: the nodal line slope and CLS analysis methods. The slope method was developed by Cho et al. in 2003, which described the first procedure for extracting the frequency-frequency correlation function from data using the slope the node between the positive and negative peaks.[44] The Fayer group devised a different method in 2007, which measured the slope through the peak maximum instead, which is beneficial when the anharmonicity is small.[43]

2.4. Full nonlinear response

The full nonlinear response can be developed by taking into account the R_1, R_2, and R_3 rephasing pathways, the R_4, R_5, and R_6 non-rephasing pathways, and a full description of the dephasing. Explicitly including dephasing, the response functions for a two-state system are:

$$R_{1,2}(\tau,T,t) \propto i\mu_{01}^4 e^{+i\omega_{01}\tau} e^{-\frac{\tau}{T_2}} e^{-i\omega_{01}t} e^{-\frac{t}{T_2}}$$
$$R_{4,5}(\tau,T,t) \propto i\mu_{01}^4 e^{-i\omega_{01}\tau} e^{-\frac{\tau}{T_2}} e^{-i\omega_{01}t} e^{-\frac{t}{T_2}} \quad (84)$$

and replacing the dephasing terms with the average density matrix as done in equation (72) for the linear response:

$$R_{1,2} = i\mu_{01}^4 e^{-i\omega_{01}(t_3-t_1)} < \exp(+i\int_0^{t_1} \delta\omega_{01}(\tau)d\tau - i\int_{t_2+t_1}^{t_3+t_2+t_1} \delta\omega_{01}(\tau)d\tau) >$$
$$R_{4,5} = i\mu_{01}^4 e^{-i\omega_{01}(t_3+t_1)} < \exp(-i\int_0^{t_1} \delta\omega_{01}(\tau)d\tau - i\int_{t_2+t_1}^{t_3+t_2+t_1} \delta\omega_{01}(\tau)d\tau) > \quad (85)$$

Both sets of response functions can also be expanded in terms of the lineshape function via the cumulant expansion as performed in equation (74):

$$R_{1,2} = i\mu_{01}^4 e^{-i\omega_{01}(t-\tau)} e^{-g(\tau)+g(T)-g(t)-g(\tau+T)-g(T+t)+g(\tau+T+t)}$$
$$R_{4,5} = i\mu_{01}^4 e^{-i\omega_{01}(t+\tau)} e^{-g(\tau)-g(T)-g(t)+g(\tau+T)+g(T+t)-g(\tau+T+t)} \quad (86)$$

Including the R_3 and R_6 pathways, which access the second excited state (now considering a three-level system), is as simple as accounting for the anharmonic shift in their vibrational potentials: $\omega_{01} - \Delta$, where the anharmonicity is Δ. This results in the following additions to the cumulant expansion:

$$\begin{aligned} R_{1,2,3} &= 2i\mu_{01}^4(e^{-i\omega_{01}(t_3-t_1)} - e^{-i((\omega_{01}-\Delta)t_3-\omega_{01}t_1)}) \\ &\cdot e^{-g(t_1)+g(t_2)-g(t_3)-g(t_1+t_2)-g(t_2+t_3)+g(t_1+t_2+t_3)} \\ R_{4,5,6} &= 2i\mu_{01}^4(e^{-i\omega_{01}(t_3+t_1)} - e^{-i((\omega_{01}-\Delta)t_3+\omega_{01}t_1)}) \\ &\cdot e^{-g(t_1)-g(t_2)-g(t_3)+g(t_1+t_2)+g(t_2+t_3)-g(t_1+t_2+t_3)} \end{aligned} \tag{87}$$

The sum gives the total third-order response function, and the integrated (over t and τ) sum gives the 2DIR spectrum, measured in intensity, where the integration has Fourier transformed the signal into the frequency domain:

$$S(\omega_\tau, T, \omega_t) = i\int_0^\infty d\tau \int_0^\infty dt [\sum_{n=1}^6 R_n(\tau, T, t)] e^{-i(\omega_t t + \omega_\tau \tau)} \tag{88}$$

2.5. Experimental measurement

2.5.1. Ultrafast pulses and optical parametric amplification

The laser used in the following experiments was generated by a Spectra Physics Spitfire Ace Ti:Sapphire amplifier equipped with a MaiTai SP short pulse oscillator for generating the seed pulse and an Empower Q-switched Nd:YLF laser for pumping. The initial laser pulses are generated by passive modelocking in the Ti-sapphire crystal. The crystal is pumped by the green Nd:YLF laser, and the pulse is focused via the Kerr lens effect with two prisms in the cavity to correct pulse dispersion.[42, 137-141] The output pulse is 800 nm and used as a seed pulse for further amplification in a chirped pulse amplifier (CPA). The amplifier contains a pulse stretcher, a cavity where the amplification occurs, and a pulse compressor, in that order. The CPA first stretches the pulse duration, so that the intensity is lowered. This avoids damaging the components of the amplifier with high-intensity pulses. The amplification takes place in the

cavity, and the compressed pulse is the same wavelength as the input, 800 nm, with 1.0 W of power and a repetition rate of 5 kHz.

Following compression, the pulse is introduced to an optical parametric amplifier (OPA), which uses difference frequency generation to turn the 800 nm light into the desired infrared pulses. The pulse initially hits a beam splitter, where 96% of the signal is transmitted. The other 4% is focused on the sapphire plate of the white light generator. The remaining signal hits another beam splitter, splitting the pump into 2 components. One component, the weaker pre-amp pump, is overlapped with the emitted white light and focused on a β-barium borate (BBO) crystal to generate the signal and idler beams. The idler beam is then used as the seed pulse for further amplification. The second pump component, the power-amp pump, overlaps with the idler on the BBO crystal, amplifying the signal and idler beams. The time delay between the beams is controlled translation-stage mounted reflectors, until sufficient stability is reached, at which point both signal and idler beams exit the OPA and generate IR pulses through a $AgGaS_2$ difference frequency generation (DFG) crystal. The amplification path through the OPA is illustrated in Figure 2.4.

2.5.2. The 2DIR optics setup

The 2DIR setup used for data collection was three replica pulses focused in the box-CARS geometry, for which the phase-matching direction was $-\boldsymbol{k_1} + \boldsymbol{k_2} + \boldsymbol{k_3}$, as introduced in Figure 2.2. This is not the only experimental setup possible for 2DIR, but it is commonly used for heterodyne detection, which will be explained in the next subsection.[38, 112, 142-145] To facilitate measurement in the box-CARS geometry, the output from the DFG crystal is split into 4 beams, which are spatially-separated. Three beams $\boldsymbol{k_1}$, $\boldsymbol{k_2}$, and $\boldsymbol{k_3}$ are focused on the sample through a lens, such that all pass through the same position of the sample. A signal is then

emitted in the phase-matching direction and overlapped with the fourth pulse, the local oscillator, on a beam

splitter before being dispersed on a monochromator and detected on a 64-element MCT array detector. An optical chopper in the path of $\boldsymbol{k_3}$ is used to collect the background signal for subtraction from the emitted signal. The sample is held in a sealed optical cell wedged between two CaF_2 windows; the windows may be separated by a Teflon (or Mylar) spacer depending on the sample and concentration. For the experimental parameters typically used, τ is varied from -4 to +4 ps in increments of 5 fs per waiting time T. The path of the three beams and the local oscillator is catalogued in Figure 2.5.

2.5.3. Finding time zero

Time is completely relative in a 2DIR experiment, since everything is defined with respect to time intervals. This naturally means that the quality of the data depends on the

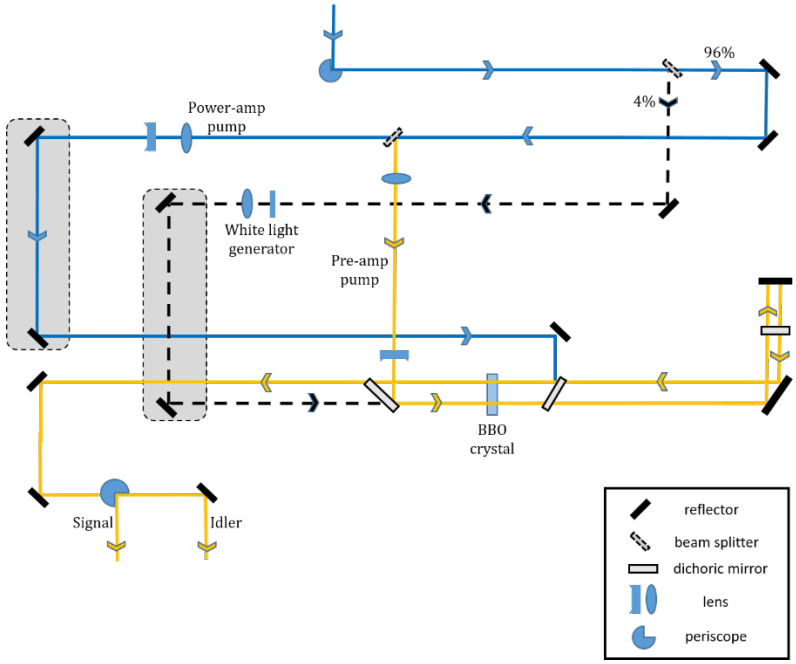

Figure 2.4. A diagram of the optical parametric amplifier (OPA) with several critical components shown.

accuracy of the time delays between pulses. To measure the overlap between pulses in time, the thermal grating signal of water is employed.[146] A pulse incident on a water sample cell heats the sample and produces a weak signal. If one pulse is moved far away in time from the other two, one pulse can be held constant in time while the other is scanned against it; when these pulses overlap in time, the grating signal from water will be maximized. This procedure is then used to overlap the other pulse as well. All the time delays are set by computer-controlled delay stages and adjusted to accuracy within 0.2 fs.

2.5.4. Heterodyned detection

The emitted photon echo signal is weak by virtue of it being an echo signal. When measuring the frequency fluctuations of a system, the signal measured should not be just the photon echo but rather the interference term between the photon echo and local oscillator. This is widely employed as heterodyned detection.[38, 144, 147] The intensity, not the electric field, for the

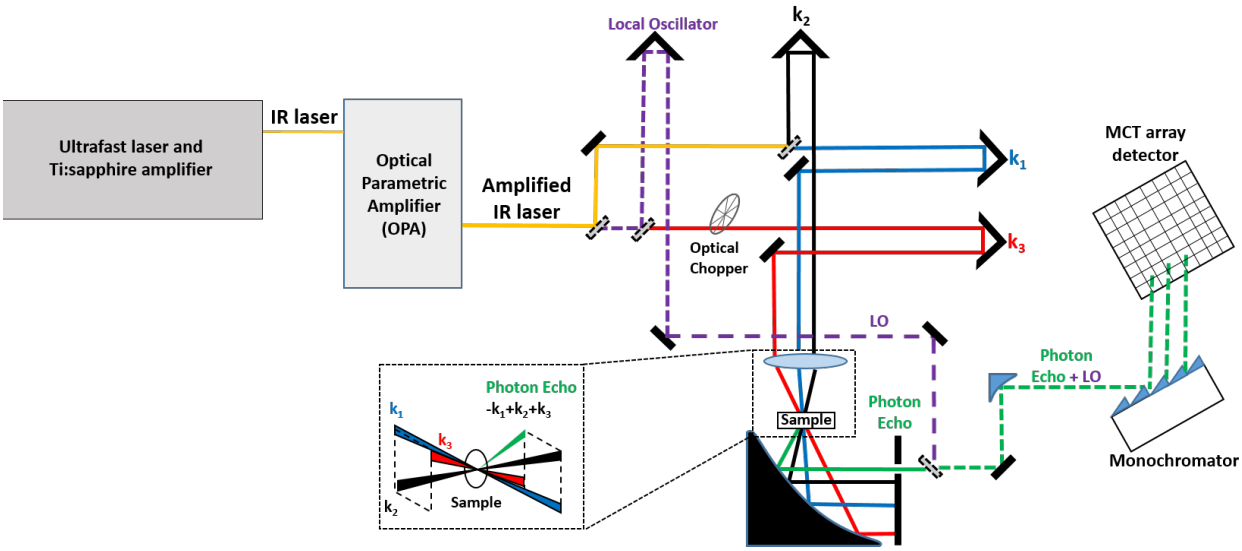

Figure 2.5. 2DIR optics setup, which generates three pulses from the OPA output aligned in the box-CARS geometry.

emitted signal will be collected by the detector, so the electric field is Fourier transformed and the magnitude squared:

$$\begin{aligned} S(\omega) \quad &\propto \left|\int_0^\infty \{E(t) + E_{\text{sig}}^{(1)}(t)\} e^{i\omega t} dt\right|^2 \\ &\propto I_0(\omega) + 2\Re\left(\int_0^\infty E(t) e^{i\omega t} dt \cdot \int_0^\infty E_{\text{sig}}^{(1)}(t) e^{i\omega t} dt\right) + I_{\text{sig}}^{(1)}(\omega) \\ &\approx I_0(\omega) + 2\Re\left(E(\omega) \cdot E_{\text{sig}}^{(1)}(\omega)\right) \end{aligned} \tag{89}$$

where $I_0(\omega)$ is the signal from the laser pulse, $I_{sig}^{(1)}(\omega)$ is the signal from the photon echo, and the middle term as the interference. The local oscillator and emitted photon echo signal are incident on the same detector, so their individual signals, as well as the interference term, will be detected. The photon echo signal can be neglected due to its negligibly-small contribution. To isolate the interference term, the signal from the laser pulse must be subtracted. This is the background collected via the optical chopper, $I_0(\omega)$, and the amplified photon echo can in this way be collected and analyzed.

2.5.5. Time domain to frequency domain spectra

The experimental setup complicates the initial data processing because the use of a monochromator leaves the data in terms of wavelength and time. To generate frequency domain spectra, the data must first be reverse Fourier transformed ($\lambda \rightarrow t$), then the entire spectra Fourier transformed twice ($\tau, t \rightarrow \omega_\tau, \omega_t$).[144, 147, 148] The reverse Fourier transform is:

$$\begin{gathered} S(\tau, T, t) = \sum_{n=1}^{64} \tilde{S}(\tau, T, t) e^{-i\omega_n t} \Delta\omega_n \\ \omega_n = \frac{2\pi c}{\lambda_n} \\ \Delta\omega_n = \frac{2\pi c}{\lambda_n - \frac{1}{2}\Delta\lambda} - \frac{2\pi c}{\lambda_n + \frac{1}{2}\Delta\lambda} \end{gathered} \tag{90}$$

Once the signal is redefined in terms of only time intervals, the standard Fourier transforms are applied in a straightforward way:

$$\tilde{S}(\tau, T, \omega_t) = \sum_t S(\tau, T, t) e^{-i\omega_t t} \Delta t$$
$$\tilde{S}(\omega_\tau, T, \omega_t) = \sum_\tau S(\tau, T, t) e^{-i\omega_\tau \tau} \Delta \tau \quad (91)$$

2.6. Summary

In this chapter, the theoretical background for interpreting frequency fluctuations, the basis of 2DIR data analysis, was outlined. The formalism for depicting an ensemble of states as a density matrix was discussed, and the linear and nonlinear response functions were developed in terms of the interactions between laser pulses and the density matrix. Several concepts central to data interpretation were explained in detail, among them coherences, dephasing, population relaxation, inhomogeneous broadening, and homogeneous broadening. Experimental considerations were examined, wherein the optics setup, the optical parametric amplifier, and detected signal were reviewed. Finally, the method of using the Fourier transform and inverse Fourier transform was introduced to convert the detected signal into a frequency domain signal for further analysis.

CHAPTER 3. THE EFFECT OF SOLVATION SHELL STRUCTURE AND COMPOSITION ON ION PAIR FORMATION: THE CASE STUDY OF LITDI IN ORGANIC CARBONATES

3.1. Introduction

Lithium ion batteries have become the standard technology in energy storage over the last 25 years. While this battery technology is particularly ubiquitous to the energy demands of portable electronics,[1] lithium ion batteries have also found its use in rechargeable power tools and electric vehicles.[1, 2] Looking into the future, substantial effort is expected for implementing lithium ion energy storage technologies in power grids.[4, 5] Thus, the rapid global adoption of lithium ion batteries has led to considerable interest in researching new materials and technologies to improve battery efficiency and lower costs. However, there is a knowledge gap of the batteries currently on the market, arising from the lack of molecular level understanding of the electrochemical components of the device.[6] More precisely, identifying the molecular-level interactions in the electrode, electrolytes, and their interphases has remained a grand challenge in science.[6]

Common electrolyte solvents for lithium ion batteries are comprised of a mixture of one linear carbonate, such as dimethyl carbonate (DMC) or ethyl methyl carbonate (EMC), and one cyclic carbonate, such as ethylene carbonate (EC), propylene carbonate (PC), or butylene carbonate (BC).[6] Cyclic carbonates are chosen for their large dielectric constants, while linear carbonates are utilized for their low viscosity.[6, 12] Thereby, linear and cyclic carbonates are both critical to the design of a functional electrolyte. However, in the mixture of carbonates, each

Reprinted with permission from Rushing, J. C.; Leonik, F. M.; Kuroda, D. G., Effect of solvation shell structure and composition on ion pair formation: The case study of litdi in organic carbonates. *J. Phys. Chem. C* **2019,** *123* (41), 25102-25112. Copyright 2022 Amercan Chemical Society.

solvent competes to solvate the lithium ion (Li+) and the anion. As such, the presence of two different solvents has significant consequences on the solvation structure of the cation and anion.

It has been shown for commercially available electrolytes, composed of lithium hexafluorophosphate ($LiPF_6$) in organic carbonates, that the structure of the Li+ solvation shell is determined by the structure of the nearby solvent molecules.[17, 49] For example, it has been found that linear organic carbonates form a more compact solvation shell than their cyclic analogues. In the latter case, the solvation shell is more extended due to the interaction between molecules in the first and second solvation shell.[149] In addition, it is apparent that the solvation structure of Li+ also dictates its speciation in solution.[14-17] Moreover, the electrolyte properties, such as conductivity, are drastically different depending on which solvent solvates Li+ and its counter-ion.[82, 150, 151] While there have been previous investigations of the effect of the solvation shell in the solvation of Li+,[17, 50, 152] questions remain about the effect of mixed solvation on solvation structure of organic carbonate electrolytes. In particular, there are contradictory findings regarding the mixtures of organic carbonates. For example, studies have concluded that linear carbonates preferentially solvate Li+,[17] while others favor the cyclic carbonate in this role.[153] Further complicating matters, other studies have concluded that preferential solvation is concentration dependent in mixtures of organic carbonates,[154] but not in mixtures of a cyclic organic carbonate and water.[155] It is also interesting that the preferential solvation is structurally dependent,[13] but the observed order (i.e., ethylene carbonate > dimethyl carbonate > vinylene carbonate) does not necessary follow the dielectric constant of the solvent. In addition, it has been observed that propylene carbonate presents dipolar ordering in solution,[156] indicating that solvent-solvent interactions could play a role in the preferential solvation. Moreover, it has been recently demonstrated that solvent-solvent

interaction are key in defining the lithium ion solvation shell structure and dynamics formed in pure cyclic carbonates.[49, 72, 157] These conflicting results clearly illustrate the merit for studying lithium salts in mixtures of organic carbonates.

While the preferential solvation by organic carbonates is a topic extensively studied,[72-75] the role of the mixed solvation shell in the speciation of Li+ is a topic vastly unexplored. So far, most studies have focused on either lithium hexafluorophosphate ($LiPF_6$) or lithium bis(trifluoromethanesulfonyl)imide (LiTFSI),[17, 65, 154, 158] but the lack of simple vibrational modes in PF_6- and TFSI- has complicated their analysis and interpretation.[17, 50, 159-160] Thus, this study focuses on the effect of carbonate structure and composition on the speciation of lithium 4,5-dicyano-2-(trifluoromethyl)imidazole salt (LiTDI, Scheme 3.1).

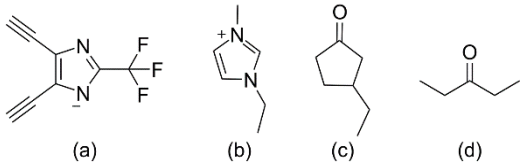

Scheme 3.1. Structures for (a) 4,5-dicyano-2-(trifluoromethyl)imidazole (TDI-), (b) 1-ethyl-3-methylimidazole (EMIM), (c) 1,2-butylene carbonate (BC) and (d) dimethyl carbonate (DMC).

LiTDI has been subject to many recent studies due to its potential as an alternative to $LiPF_6$ in electrolytes. To this end, the properties of LiTDI in various electrolytes have been explored. In particular, the physicochemical and electrochemical properties of LiTDI in solvents such as acetonitrile,[161] propylene carbonate,[162, 163] methyl and ethyl ethers of poly(ethylene glycol),[164] poly(ethylene oxide),[165] mixed carbonate solvents, [166] and ionic liquids[167] have been studied. Other studies on LiTDI have concentrated on the interaction and coordination of Li+ and the anion in solution,[168] and solvates.[169] Overall, these studies have shown that nitrile (-CN) groups are sensitive infrared probes to the speciation of TDI-.[117, 170] In particular, it has been derived that TDI- forms ion pairs with Li+ at low concentrations in mixed solvents, in spite of the strong delocalization of the charge in the anion.[165] While the

effect of a mixed solvent on the speciation of LiTDI has been studied from the conductivity and transport number perspective,[165, 171] the molecular origins behind the speciation of LiTDI in the different carbonate solutions are still unknown.

This study focuses on the speciation of LiTDI in pure linear and cyclic carbonates as well as their mixtures using linear infrared (FTIR) and time-resolved infrared spectroscopies. Two dimensional IR (2DIR) spectroscopy is used because it can determine the dynamics processes, such as solvation shell reorganization and ion pair formation, on picosecond timescales, which is well beyond the capabilities of other commonly used characterization spectroscopies, such as NMR.[38] Furthermore, 2DIR spectroscopy also features high frequency resolution and a second dimension, which provide one not only with the opportunity of resolving peaks not seen in linear spectra,[172, 173] but also with the possibility of determining vibrational coupling among vibrational transitions.[38, 148, 174, 175] This last feature is an essential characteristic for correctly assigning vibrational peaks and their assignment to different species.[38, 113, 175] These two characteristics grant 2DIR spectroscopy with unique insights into the structure and dynamics of systems at a molecular level. In particular, 2DIR spectroscopy has been successfully used to study the ion-ion and ion-solvent interactions in a variety of systems.[149, 176-182] Thus, the use of FTIR and 2DIR allows us to study the structure and dynamics of LiTDI in organic carbonates, as well as to obtain the speciation of the ion. To this end, our study of LiTDI is focused on each pure solvent (DMC and BC) and on their mixtures. The LiTDI salt is employed due to its well-documented sensitivity to solvent environment[183-186] and spectrally-isolated infrared bands.[187] Our experimental results provide a molecular picture of the anion solvation structure and dynamics, which are complemented with computational calculations to validate the modeling of our findings.

3.2. Methods

3.2.1. Experimental methods

3.2.1.1 Sample preparation. Lithium 4,5-dicyano-2-(trifluoromethyl)imidazole (LiTDI, Alfa Aesar, 95% pure) was dried at 140° C for 15 hours under vacuum before use and stored in a N_2-filled glovebox. 1-ethyl-3-methylimidazolium 4,5-dicyano-2-(trifluoromethyl)imidazole ((EMIM)TDI) was synthesized in 95% purity (by NMR) according to Ref. [165]. Dimethyl carbonate (DMC, 99+% Acros Organics), ethyl methyl carbonate (EMC, >98% TCI), propylene carbonate (PC, 99.5% Acros Organics), and 1,2-butylene carbonate (BC, 98% TCI) were all dried under activated 4A molecular sieves prior to use to remove water. All components were stored in a N_2-filled glovebox to minimize exposure to moisture. In addition, all solutions and samples were prepared inside the glovebox. All samples tested <200 ppm of water after preparation.

Sample cells were prepared in a N_2-filled glovebox by sandwiching the LiTDI solution between two CaF_2 windows with a 6 μm spacer. The same preparation was used for both FTIR and 2DIR sample cells for experiments in the nitrile IR stretch region (2100-2300 cm^{-1}). All 2DIR experiments were conducted at the same concentration (X_{Li} = 0.05) because of the poor solubility of the salt in linear carbonates (i.e., DMC and EMC). In this case, X_{Li} is defined as the moles of Li+ over the total moles of Li+ and solvent. Also, FTIR sample cells used in the carbonyl IR stretch region (1700-1900 cm^{-1}) were prepared by sandwiching the sample between two CaF_2 windows without a spacer to minimize the high absorbance for the carbonyl band of the organic carbonate.[49] The approximate path length of this latter cell is ~1-2 μm.

3.2.1.2. FTIR Spectroscopy. FTIR spectra were taken on a Bruker Tensor 27 spectrometer with a 0.5 cm^{-1} resolution. Forty scans were averaged for each spectrum.

3.2.1.3. 2D IR Spectroscopy. The setup used for 2DIR experiments has been previously detailed in the literature, so only a short description is provided here.[38, 142] The input IR pulses were generated with a Spectra Physics Spitfire Ace Ti:sapphire amplifier at a repetition rate of 5 kHz, in combination with an OPA-800C and difference frequency generation crystal. These input IR pulses were then split into 3 replicas and later focused on the sample using the well-known boxcars geometry.[143] The photon echo signal was measured in the $\mathbf{-k_1+k_2+k_3}$ phase-matching direction. A heterodyned detection was performed using a forth pulse (local oscillator). The heterodyned signal was measured in a 64 element MCT array detector after dispersing the heterodyned signal in a spectrometer. The photon echo signal was measured as a function of three critical time intervals: the coherence time τ (interval between pulses 1 and 2), the waiting time T_W (interval between pulses 2 and 3), and the coherence time t (interval between pulse 3 and the detected signal). These time intervals were set via computer-controlled translation stages. Here, 2D IR data were collected by scanning τ time from -4 ps to +4 ps in increments of 5 fs for each waiting time in order to collect both the rephasing and non-rephasing data by switching the time ordering.[38] Signals were collected for waiting times from 0 to 5 ps in steps of 0.5 ps. Note that the data collection in waiting was confined to a maximum of 5 ps due to the presence of heating effects, seen in Figure 3.1. In all the measurements, the local oscillator always preceded the photon echo signal by ~0.5 ps. The time domain signal, collected as function of (τ,T, λ_t) via a monochromator-array detection, is transformed into the 2DIR spectra (ω_τ, T, ω_t) by means of Fourier transforms. A detailed explanation of the Fourier analysis has been described elsewhere.[148]

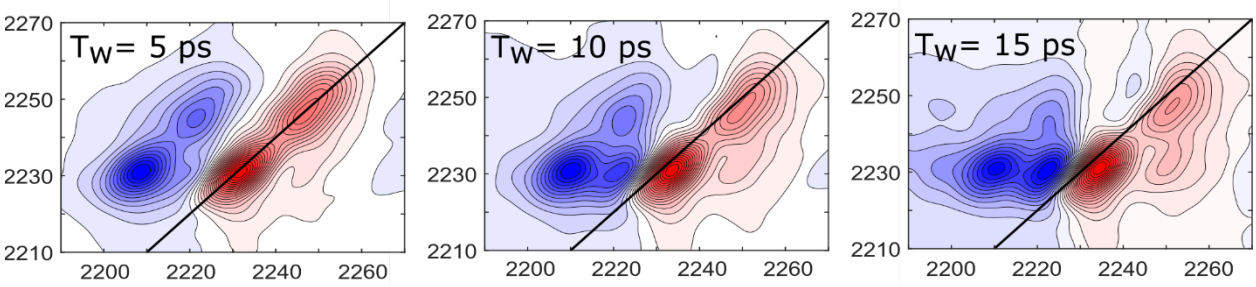

Figure 3.1. 2DIR spectra of LiTDI in DMC for waiting times 5ps, 10ps and 15ps.

3.2.2. Computational methods

3.2.2.1. DFT calculations. Density functional theory (DFT) frequency calculations were conducted in Gaussian 09 software.[188] Geometry optimizations and frequency calculations were conducted using DFT with B3YLP functional and the 6-311++G** basis set. This functional and basis set has been successfully used to investigate the energetics and IR frequencies of lithium ion solvation structures and its ion pairing.[17, 50, 162, 189, 190] Initial molecules were built in the Avogadro software and the structures were first minimized using a classical force field (MMFF94). All geometries were optimized in Gaussian 09. Geometry optimizations and frequency calculations were performed in vacuum since the addition of a dielectric continuum has been shown to not change the trends in the Li+ solvation.[191] After minimization, molecules did not present imaginary frequencies confirming each structure as a minimum on the potential energy surface. The energy of ion pair formation as function of solvation shell structure and composition was computed using the same procedure as Ref. [192]. The natural bond orbital analysis (NBO) was used to calculate the atomic partial charges.[193-195] NBO was performed at the same level of theory (B3LYP/6-311++G**) using the NBO software implemented in Gaussian 09 software.

3.3. Results

3.3.1. FTIR spectroscopy of single-solvent solutions

The characterization of the solvation shell of Li+ was performed by measuring the IR spectra in the carbonyl stretch region (1700-1900 cm^{-1} region). FTIR spectra of different concentration solutions of LiTDI (X_{Li} = 0.01, 0.025, and 0.05) in DMC and BC are shown in Figure 3.2. The IR spectra display a high-intensity band located at 1755 cm^{-1} and at 1797 cm^{-1} for DMC and BC, respectively. A low frequency band, located at 1725 cm^{-1} for DMC and at 1765 cm^{-1} for BC, rises with increasing Li+ concentration in the solution. Due to its growth with increasing Li+ concentration, the low frequency band has been previously assigned to the carbonyl stretch of carbonate molecules coordinated to Li+.[6, 17, 117] Similarly, the high frequency band has been previously assigned to the free carbonyl stretch of the solvent.[6, 17, 117]

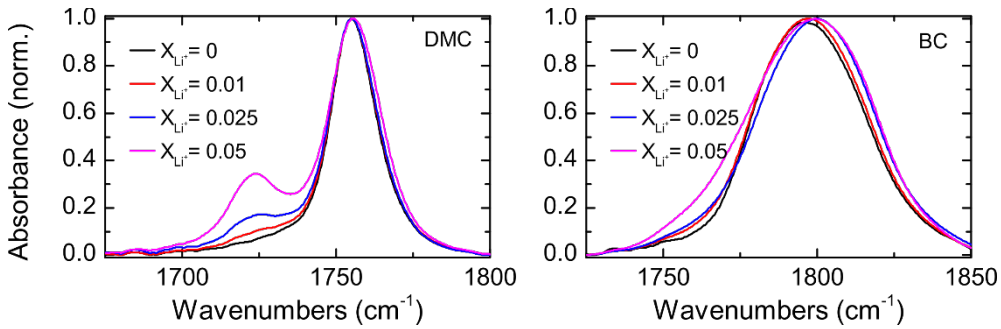

Figure 3.2. FTIR spectra for the carbonyl region of LiTDI as function of concentration: X_{Li} = 0.00 (black), 0.01 (red), 0.025 (blue), and 0.05 (pink) in DMC (left panel) and BC (right panel). XLi = 0.00 corresponds to the sample containing (EMIM)TDI with XEMIM=0.05 Both spectra are normalized with respect to the high frequency band.

The characterization of the TDI- solvation was performed by measuring the IR spectra in the CN stretch region (2150-2300 cm^{-1}). Figure 3.3 shows the IR spectra of LiTDI in DMC and BC as a function of Li+ concentration (X_{Li} = 0.00, 0.01, 0.025, and 0.05). Note that the sample with X_{Li} = 0.00 corresponds to the sample containing (EMIM)TDI with X_{EMIM}=0.05. In both

carbonate solutions, a low frequency band (2230 cm^{-1} for DMC, 2225 cm^{-1} for BC) and a high frequency band (2247 cm^{-1} for DMC, 2245 cm^{-1} for BC) are observed. The high frequency bands grow with increasing Li+ concentration in both samples, but it always remains significantly higher for DMC than BC solutions with equal X_{Li}. For comparison purposes, the FTIR spectra of (EMIM)TDI at X_{EMIM} = 0.05 in DMC and BC are also displayed in Figure 3.3.

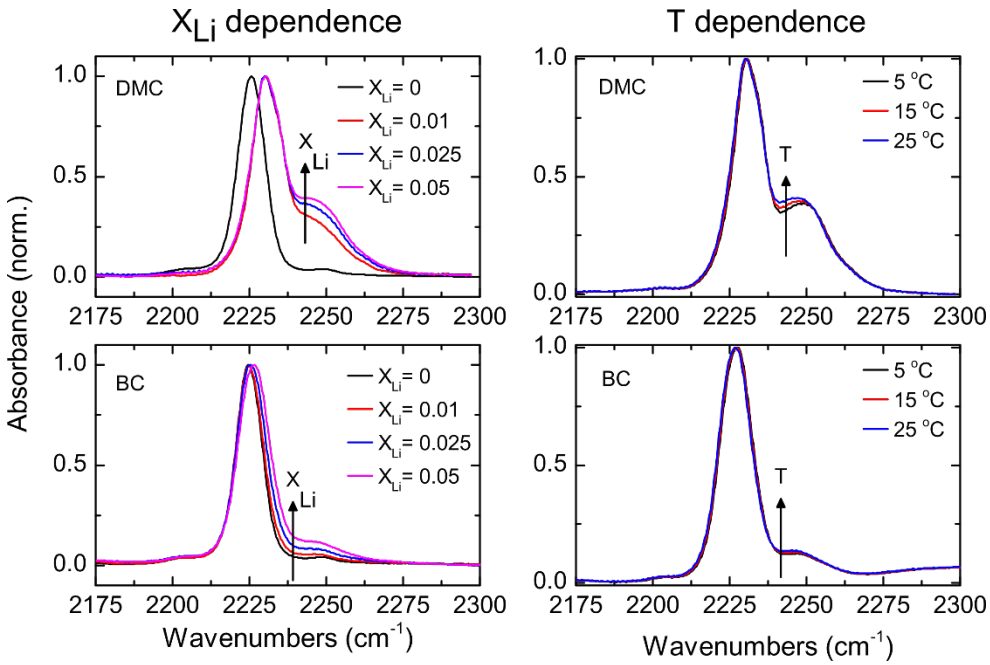

Figure 3.3. FTIR spectra for the nitrile region of LiTDI. Left panels concentration dependence of LiTDI for X_{Li} = 0.01, 0.025, and 0.05 in DMC (top) and BC (bottom) and (EMIM)TDI (X_{Li} = 0.00 and X_{EMIM} = 0.05) for comparison. Right panels temperature dependence of LiTDI (X_{Li} = 0.05) in DMC (top) and BC (bottom) for 5 °C, 15 °C, and 25 °C. All spectra are normalized with respect to the low frequency band.

Interestingly, (EMIM)TDI shows only one peak at 2225 cm^{-1} in both solvents. Note that the small peak at 2250 cm^{-1} observed in the (EMIM)TDI in both solvents arises from either the residual Li+ or an impurity from its synthesis (see methods section). While the peak position of TDI- presents the same frequency position for (EMIM)TDI and LiTDI in BC, a shift of ~5 cm^{-1} is observed for the DMC solution. The difference between the CN stretch bands of TDI- in samples containing Li+ and EMIM+ is attributed to the different speciation of the TDI- in the

two solvents. The assignment of the CN stretch peaks is further investigated by temperature-dependent FTIR. The IR spectra of the LiTDI samples with X_{Li}=0.05 as function of temperature is displayed in Figure 3.3. Both samples present two discernable changes with temperature: a small frequency shift and a change in the ratio of absorptions between the two frequency bands, in which the high frequency band grows with respect to the low frequency band with increasing temperature. These spectral changes with temperature are also in agreement with the difference spectra shown in Figure 3.4.

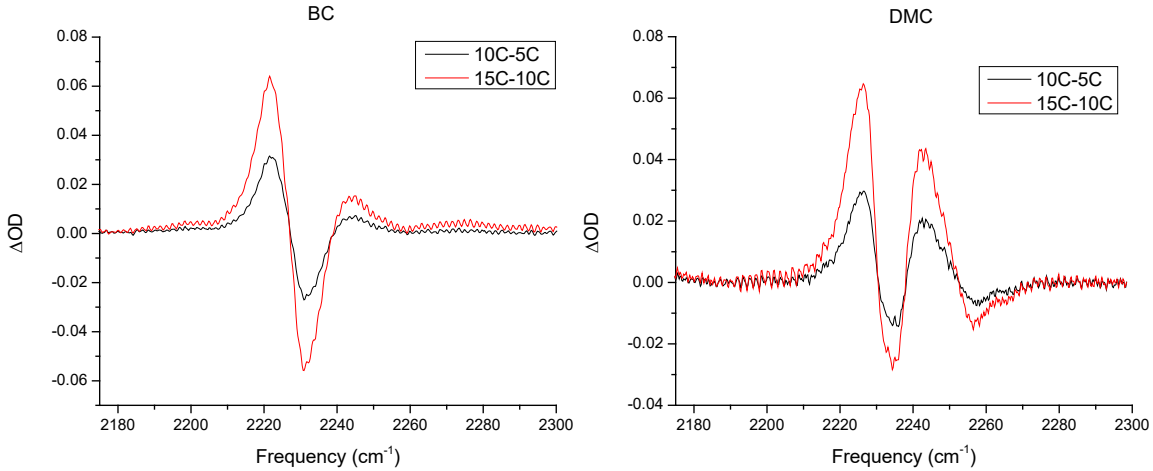

Figure 3.4. Changes in the CN stretch spectra of BC and DMC with temperature using the spectrum at 5°C as a reference.

3.3.2. 2DIR spectroscopy

TDI- was further investigated by measuring the 2DIR spectra. The 2D IR spectra for LiTDI in DMC and BC are presented in Figure 3.5 for waiting times 0 ps, 2.5 ps, and 5 ps. As in the FTIR spectra, two sets of peaks are observed at ω_τ = 2230 cm^{-1} and ω_τ = 2247 cm^{-1} for DMC and at ω_τ = 2225 cm^{-1} and ω_τ = 2245 cm^{-1} for BC. In the 2DIR spectra, the red (positive) peaks located in the diagonal (ω_τ= ω_t = 2025 cm^{-1} for DMC, ω_τ= ω_t = 2030 cm^{-1} for BC) represent the

transitions between ν=0 and ν=1 vibrational states, and blue (negative) peaks down shifted by ~25 cm^{-1} depict the transitions between ν=1 to ν=2 vibrational states.[38] The downshifts of the blue peaks with respect to the red peaks denotes the anharmonic nature of CN stretch potential of TDI- and is in agreement with other aromatic nitrile groups.[196] The 2DIR spectra also demonstrate that the intensity of the low frequency peak is always greater than that of the higher frequency peak in both solvents. Moreover, the high frequency peak has a larger intensity forDMC than BC. In fact, in the latter case, the high frequency peak is substantially weaker in the 2DIR spectra. The observed number of diagonal peaks and their intensities in the 2DIR have the expected direct correspondence with the linear IR spectra for the two samples.

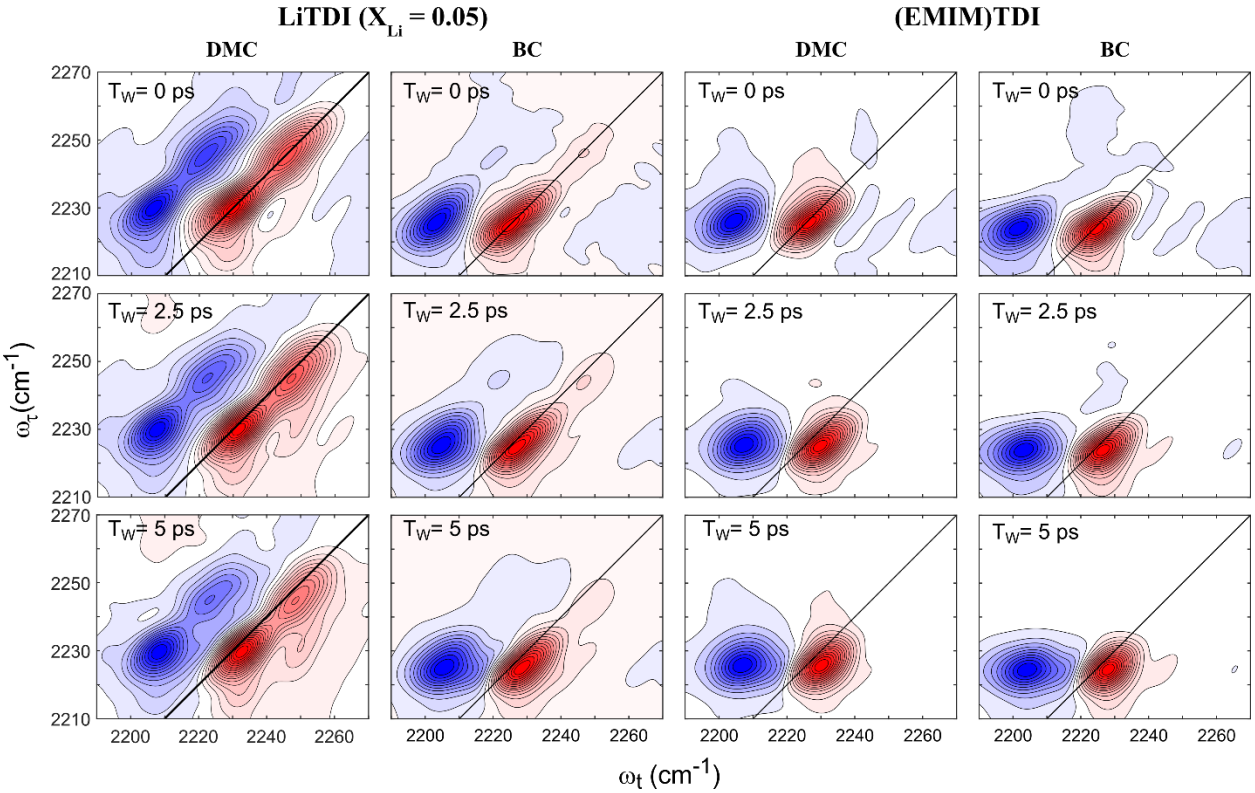

Figure 3.5. 2D IR spectra for the nitrile region of LiTDI (X_{Li} = 0.05) and (EMIM)TDI (X_{EMIM} = 0.05) in DMC and BC. The presented spectra corresponds to three waiting times: 0 ps, 2.5 ps, and 5 ps.

The 2DIR spectra do not display significant changes in the shape of the peaks with waiting time (T_W) besides the changes in intensity given by the vibrational population lifetime. In other words, the peaks initially elongated along the diagonal remain nearly unchanged as T_W progresses. A small cross peak is also present at $T_W = 0$ ps at $[\omega_\tau,\omega_t]=[2230\ cm^{-1}, 2250\ cm^{-1}]$ for DMC, but it is not appreciable in the 2DIR of LiTDI in BC at the zero waiting time. However, the cross peak appears to grow with increasing T_W for both DMC and BC. Moreover, the cross peak growth in the BC sample is also corroborated by the waiting time evolution of the integrated sections of the 2DIR spectra, represented in Figure 3.6. The presence of cross peaks is evidence of a vibrational coupling between the two CN stretch modes of TDI- (see next section).[38, 175, 197] For comparison, 2DIR spectroscopy was also performed on (EMIM)TDI in DMC and BC samples. In these later samples, only one set of peaks was observed at ω_τ = 2225 cm^{-1} irrespective of the solvent. In addition, the peaks appear to become rounder with waiting time in both cases, contrasting with LiTDI samples where no apparent evolution is observed with T_W.

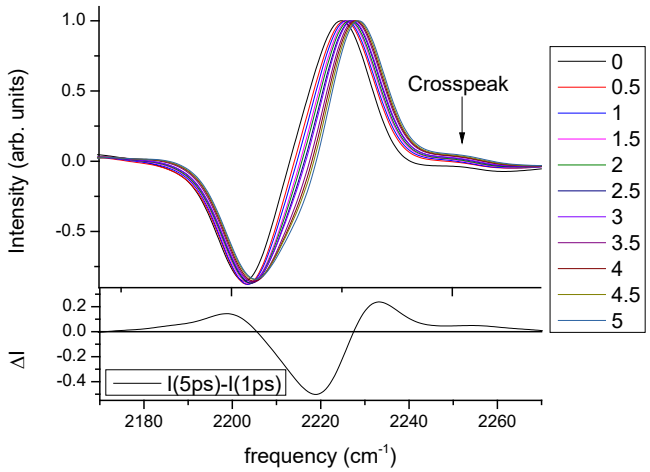

Figure 3.6. Integrated slice as function of waiting time for the 2DIR spectra of BC. The slices are taken in a range of 5 cm^{-1} from the maximum at ~2225 cm^{-1}.

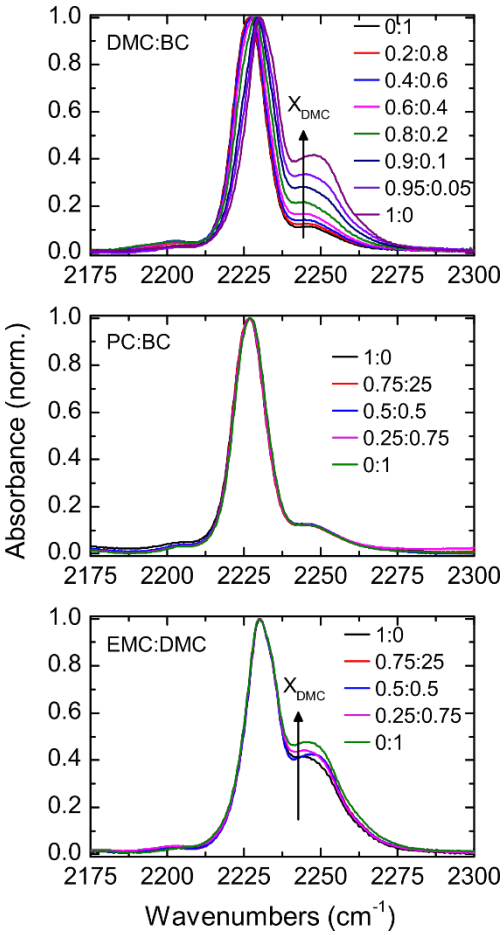

Figure 3.7. FTIR spectra for the nitrile region of LiTDI (X_{Li} = 0.05) as a function of solvent composition. The mixed solvent data is representative of [X:1-X] ratios as indicated in the figure for DMC:BC (top), PC:BC (middle) and EMC:DMC (bottom).

3.3.3. FTIR spectroscopy of binary-mixture solutions

Finally, the FTIR spectroscopy of LiTDI (X_{Li} = 0.05) in DMC/BC, DMC/EMC, and BC/PC solvent mixtures were investigated (Figure 3.7). For mixtures, two bands located at 2225 cm^{-1} and 2250 cm^{-1} are observed with the low frequency band having a larger intensity in all samples at all compositions. While the mixtures of linear carbonates (DMC/EMC) and cyclic carbonates (BC/PC) do not appear to show substantial changes in the band areas with solvent composition, the linear and cyclic mixture (DMC/BC) shows that the low frequency band shifts its frequency position to higher values as the concentration of DMC increases in the solvent. In

addition, there is a large change in the ratio of absorptions between the two CN stretch bands as the solvent composition changes from pure BC to pure DMC.

3.4. Discussion

3.4.1. Pure carbonates

The speciation of TDI- is directly related to the overall solvation of Li+. Based on previous assignments of the bands in the 1700-1900 cm^{-1} region, the appearance of a low-frequency band in the C=O stretch region (Figure 3.2) shows that some carbonates are directly coordinated to Li+.[117] While the solvation of Li+ through the carbonyl bands is evident, the complex nature of the carbonyl band does not allow us to conclude whether Li+ is fully solvated by the solvent or is forming contact ion pairs.[49, 160] However, the results show that even in the case of Li+ and TDI forming contact ion pair, the majority of Li+ must be partially solvated by carbonates.

Table 3.1. Integrated oscillator strength for the CN stretches of TDI-

Species	Sum of CN stretch Anion Band Intensities (KM/Mole)
CIP - $LiTDI(BC)_3$	251
CIP - $LiTDI(BC)_2(ctDMC)$	248
CIP - $LiTDI(BC)(ctDMC)_2$	278
CIP - $LiTDI(ctDMC)_3$	228
SSIP - $Li(ctDMC)_4TDI$	244
Free anion - $TDI(DMC)_4$	247

From the anion perspective, the nitrile stretch region provides a direct window to investigate the anion. The spectra of (EMIM)TDI in both solvents (Figure 3.3) presents only one band at 2225 cm^{-1}. Since the imidazolium cation has a delocalized charge, it is unlikely that EMIM+ will form contact ion pairs (CIP) with TDI- or affect its vibrational manifold.[179, 198] Thus the band at 2225 cm^{-1} is assigned as the free anion band in pure BC and DMC. It is

important to note that the free anion band is comprised of two transitions, the asymmetric and symmetric nitrile stretches.[175] The two combination modes of CN stretches are nearly-degenerate in the free species because the solvent lacks sufficiently large and directional interactions to break the symmetry of the molecule, but the non-degeneracy can explain the small asymmetry of the TDI- peak towards the high frequency side. The presence of Li+ in the TDI- solutions produces the growth of a second peak at ~2245 cm^{-1} in DMC and BC pure solvents. The appearance of the high frequency peak denotes the formation of contact ion pairs as previously demonstrated.[175, 179] In the case of CIPs, the coordination of Li+ to TDI- breaks the symmetry of the molecule, which shifts the frequency of one of the CN modes to ~20 cm^{-1} higher than that observed for the free ion (i.e., (EMIM)TDI solution). While the same splitting and the growth of the high frequency band with Li+ concentration is observed for LiTDI in both carbonates, the intensity of the high frequency band is much greater in DMC than BC solution. While this result could be interpreted as a change in the oscillator strength of TDI- and the different ion pairs, DFT computations in Table 3.1 show that the oscillator strength is similar for TDI- as free ion, SSIP, and CIPs with different carbonates. Thus, the appearance of the high frequency band shows that the structure of the organic carbonate affects the formation of contact ion pairs, which is in agreement with previous studies.[49, 179] In particular, it shows that CIP species are more prevalent in linear carbonates, which differs with other anions such as hexafluorophosphate (PF6-) ions and bis(trifluoromethanesulfonyl)imide (TFSI) ions at the same concentrations.[17, 49, 152, 159] Moreover, it has been previously shown that the charge delocalization of the anion is not sufficient to avoid a strong interaction with the cation. For example, the thiocyanate anion (SCN-) also shows a strong interaction with cations of different

sizes and charge density in various environments, even though it has a relatively delocalized charge and it is on the extreme of the Hofmeister series.[178, 179, 181, 199]

The proposed TDI speciation and IR CN stretch assignments are further tested by computing the vibrational modes of the possible different species using DFT computations. DFT frequency calculations of the CN stretches for free TDI-, solvent separated ion pair (SSIP), and CIP are presented in Figure 3.8. The free anion spectrum presents two nearly overlapping transitions located at 2312 cm^{-1} and 2315 cm^{-1} with similar intensities. Similarly, the SSIP spectrum shows two overlapping modes with similar intensities. In contrast, the CIP CN stretch modes are split into two distinct bands located at 2308 cm^{-1} and 2331 cm^{-1}, and the intensity of the low frequency mode is larger than that of the high frequency mode. The theoretical calculations show that the growth of the high-frequency band in the CN region of the IR spectrum of TDI in either solvent only evidences the formation of CIPs. In addition, they demonstrate that the IR spectroscopy is not sensitive enough to differentiate between SSIPs and free ions as previously observed in other ions. [123, 200, 201]

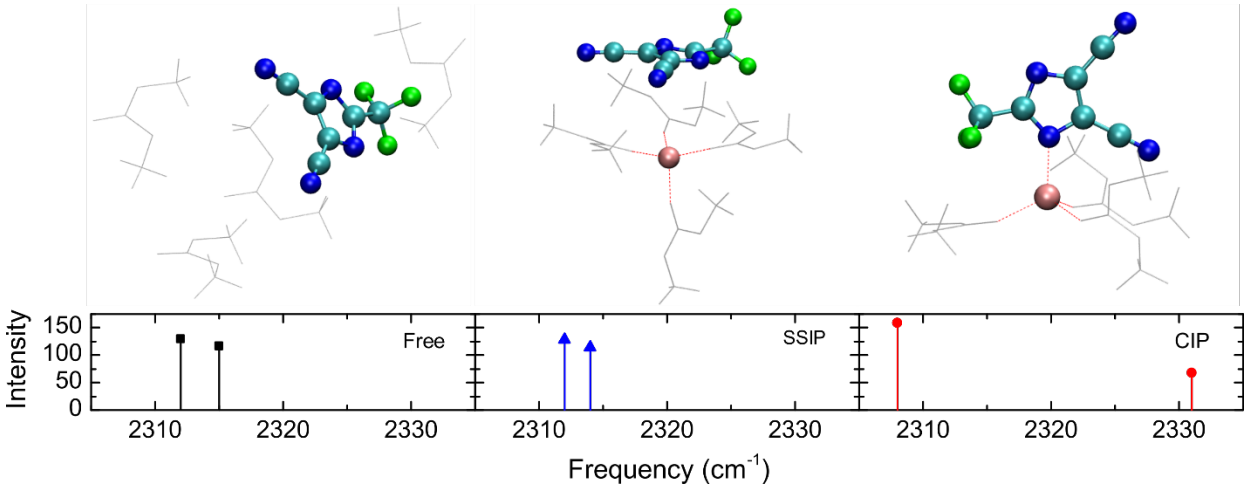

Figure 3.8. Structures and calculated vibrational frequencies for different species of anion association: free anion, solvent-separated ion pair (SSIP), and contact ion pair (CIP).

The experimental data as well as the DFT frequency calculations provide a reasonable assignment of the FTIR bands of LiTDI in both solvents. However, the DFT frequency calculations also present some ambiguity. For example, DFT computations predict that the two CN stretches of the SSIP or free TDI- should appear at the same frequency as the low frequency band in the CIP. Thus, it is not possible to evaluate whether LiTDI in DMC is present as a mixture of CIPs and SSIPs or only CIPs. To this end, the spectrum of an equimolar mixture of LiTDI and (EMIM)TDI (X_{Li}=X_{EMIM}=0.05) in DMC was measured. In this case, the IR spectrum of the sample shows the same number of peaks and frequency positions as in the pure LiTDI, but the intensity of the high frequency peak decreases by half (Figure 3.9, left). The result indicates that LiTDI in DMC solution is composed in its majority by CIPs and that only LiTDI contributes to the formation of CIPs in DMC. In other words, the presence of extra TDI- in the solution does not change ion pair equilibrium (Li+ + TDI- ↔ LiTDI) because the anion is primarily as CIPs in the DMC solution. In addition, it is observed that the frequency position and width of the low frequency band of TDI- is not affected by the mixture, indicating that the difference in frequency between the EMIM+ and Li+ samples is likely to be caused by the difference in the dielectric constant of the solution due to the presence of the lithium salt.[202] These findings support the assertion that LiTDI does not form free ions or SSIPs in DMC, which is in agreement with the previous speciation of LiTDI in DMC.[179] However, our results indicate that TDI- is primarily found as free ion or SSIP in BC solutions.

In addition, temperature-dependent FTIR performed on LiTDI (X_{Li} = 0.05) in DMC and BC further supports our assignment, since it shows that the high frequency band at ~2245 cm^{-1} grows with increasing temperature irrespective of the solvent. This observation is in agreement with the CIP becoming more energetically favorable at high temperature due to a decrease of the

Gibbs free energy of CIP formation with increasing temperature.[203] The temperature dependence of the Gibbs free energy in CIP formation is caused by the entropy term, which is positive because solvent molecules gain in the degrees of freedom when they are removed from the solvation shell of the ions as a consequence of ion pair formation.[203, 204]

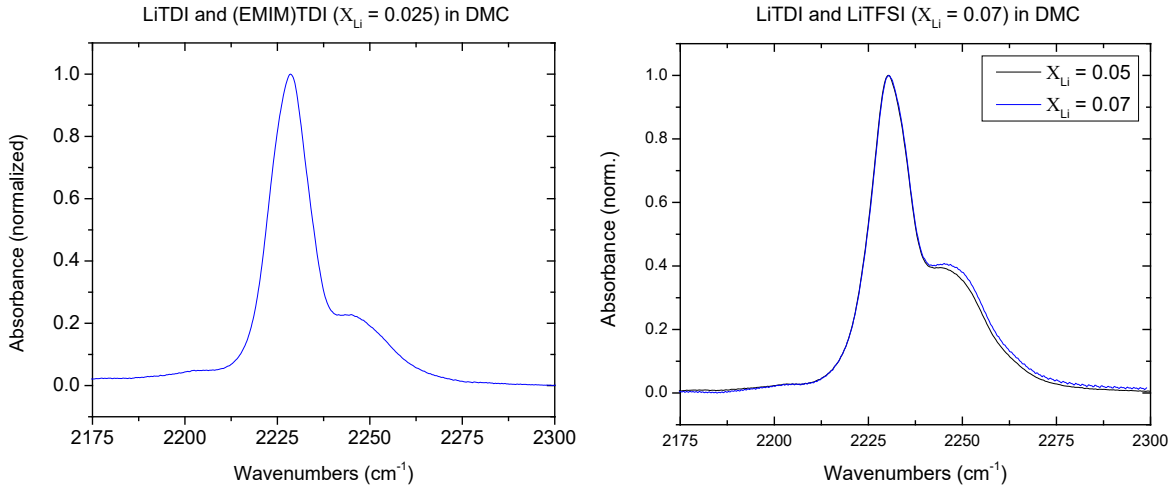

Figure 3.9. FTIR spectra for mixtures of LiTDI/(EMIM)TDI (X_{Li} = 0.025) in DMC and LiTDI/LiTFSI (X_{Li} = 0.07) in DMC.

The structure and dynamics of TDI- in the organic carbonates were also derived from 2D IR spectroscopic experiments. The 2DIR spectra of LiTDI in DMC and BC (Figure 3.5) show two pairs of peaks with the lower frequency bands having higher intensity as seen in the linear IR (Figure 3.3). However, the second dimension allows one to observe a cross peak between the two diagonal peaks for both DMC and BC samples. The presence of a cross peak indicates a vibrational coupling between the two nitrile stretches modes of the anion.[38, 197] In turn, the vibrational coupling confirms that some TDI- have a broken symmetry in their nearly degenerated CN stretches caused by the direct interaction of Li+ with TDI-. Thus, the presence of the cross peak further confirms the formation of CIPs and their vibrational signatures. While it is also possible that the cross peak arises from chemical exchange between SSIPs and free TDI and CIPs,[38] the presence of the cross peak at T_W=0 makes the exchange mechanism unlikely,

since it implies a rate of ion pair formation comparable to the IR excitation pulse duration; i.e., ~50-60 fs.[172, 182, 205] Moreover, DFT computations predict a favorable energetics for the ion pair formation on the order of ~50 kcal/mol (see next section), which is significantly larger than the available thermal energy of system. In addition, the 2DIR spectra for (EMIM)TDI in either DMC or BC at various waiting times (Figure 3.5) display only one set of peaks at 2225 cm^{-1}, but neither sample presents an obvious cross peak at T_W=0 ps. Thus, the cross peak seen in the 2DIR spectra corroborates the idea that CIPs species exist in both DMC and BC samples. Furthermore, the high frequency peak in the 2DIR spectra does not show evidence of an intraband cross peak at longer waiting times, which indicates that this peak does not contain two CIP transitions and only corresponds to the high frequency transition of the CIP as predicted by DFT calculations (Figure 3.8).

The structure and dynamics of TDI- in the organic carbonates were also derived from 2D IR spectroscopic experiments. The 2DIR spectra of LiTDI in DMC and BC (Figure 3.5) show two pairs of peaks with the lower frequency bands having higher intensity as seen in the linear IR (Figure 3.3). However, the second dimension allows one to observe a cross peak between the two diagonal peaks for both DMC and BC samples. The presence of a cross peak indicates a vibrational coupling between the two nitrile stretches modes of the anion.[38, 197] In turn, the vibrational coupling confirms that some TDI- have a broken symmetry in their nearly degenerated CN stretches caused by the direct interaction of Li+ with TDI-. Thus, the presence of the cross peak further confirms the formation of CIPs and their vibrational signatures. While it is also possible that the cross peak arises from chemical exchange between SSIPs and free TDI and CIPs,[38] the presence of the cross peak at T_W=0 makes the exchange mechanism unlikely, since it implies a rate of ion pair formation comparable to the IR excitation pulse duration; i.e.,

~50-60 fs.[172, 182, 205] Moreover, DFT computations predict a favorable energetics for the ion pair formation on the order of ~50 kcal/mol (see next section), which is significantly larger than the available thermal energy of system.

In addition, the 2DIR spectra for (EMIM)TDI in either DMC or BC at various waiting times (Figure 3.5) display only one set of peaks at 2225 cm^{-1}, but neither sample presents an obvious cross peak at T_W=0 ps. Thus, the cross peak seen in the 2DIR spectra corroborates the idea that CIPs species exist in both DMC and BC samples. Furthermore, the high frequency peak in the 2DIR spectra does not show evidence of an intraband cross peak at longer waiting times, which indicates that this peak does not contain two CIP transitions and only corresponds to the high frequency transition of the CIP as predicted by DFT calculations (Figure 3.8).

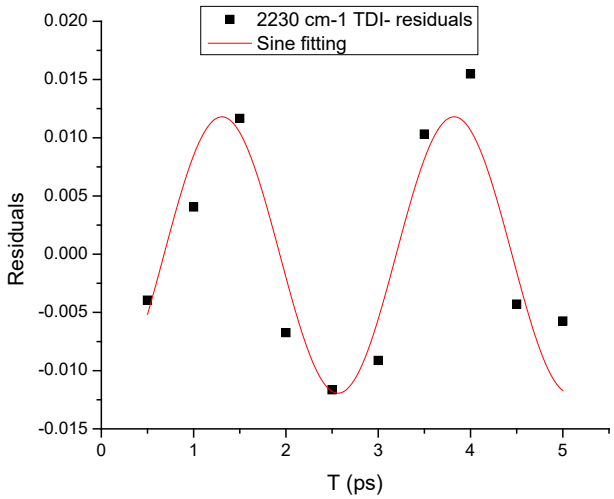

Figure 3.10. Fitting of the residual with a sine function of the form $y = y0 + A.sin(2\pi\nu T + \phi)$.

The dynamics of TDI- is derived from the 2DIR spectra using the center line slope (CLS) analysis.[43] The CLSs as a function of T_W for (EMIM)TDI and LiTDI in both pure DMC and pure BC are shown in Figure 3.11. The CLSs of the free anion from the (EMIM)TDI samples reveal an exponential decay dynamics of ~13 ps and ~12 ps (Table 3.2) for BC and DMC, respectively. The similarity between spectral diffusion characteristic times shows that both

systems sense similar environments. In the case of the sample containing almost all of CIP, such as LiTDI in DMC, the peak at 2230 cm^{-1} shows a faster dynamics than the free ion and it has an offset (Table 3.1). While the difference in the dynamics evidences that the CN transitions might have a different mechanism for the frequency fluctuation, the offset in the CLS is related to the presence of multiple vibrational transitions associated to different configurations of the CIP, which are likely to exchange with much slower time constants than the investigated time window as previously seen for other CIPs.[172, 206]

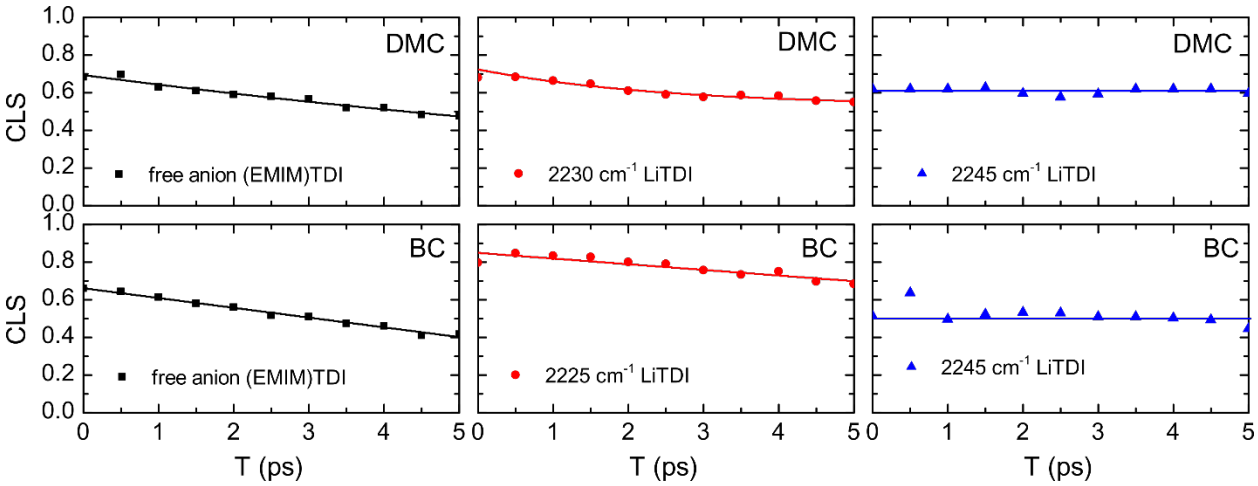

Figure 3.11. CLS analysis of the 2D IR bands of (EMIM)TDI (X_{EMIM} = 0.05) and LiTDI (X_{Li} = 0.05) in DMC and (EMIM)TDI (X_{EMIM} = 0.05) and LiTDI (X_{Li} = 0.05) in BC as a function of waiting time, T_W. Black squares correspond to (EMIM)TDI and red circles and blue triangles relate to the low and high frequency bands of LiTDI, respectively.

Table 3.2. Time constants and amplitudes for CLS fitting. *Time constants were derived from a linear fit (see derivation below). **Requires more than one exponential (see Figure 3.12 below).

Salt	Solvent	Solvent	Solvent	Solvent	Solvent
Salt	DMC	DMC	DMC	BC	BC
Salt	τ (ps)	A_0	y_0	τ (ps)	A_0
(EMIM)TDI	12.0*	0.69 ± 0.01	--	12.7*	0.662 ± 0.007
LiTDI (2230 cm^{-1})	2.5 ± 0.8**	0.19 ± 0.01	0.53 ± 0.03	23.7*	0.873 ± 0.008
LiTDI (2245 cm^{-1})	>100	0.728 ± 0.007	--	>100	0.58 ± 0.02

Moreover, the residual of the CLS fitting of the 2230 cm^{-1} band (Figure 3.10) shows the presence of an oscillation with a period of 9-30 cm^{-1}, which could arise from coherent vibrational

energy transfer of the two CN mixed modes of TDI-,[207, 208] since they are separated by ~20 cm^{-1} in DMC. Interestingly, the CLS of the high frequency peak, located at 2247 cm^{-1} and assigned to one transition of the CIP, exhibits a nearly constant behavior in both DMC and BC samples. The observed behavior might not be directly related to the solvation dynamics due to the excitonic nature (strong coupling of the two CN stretches) of the vibrational modes. In other words, for two strongly coupled and degenerated transitions, the vibrational Hamiltonian in the CN site representation can be written as:

$$\hat{H} = \begin{bmatrix} \omega_{10} + \delta\omega^1(t) & \beta(t) \\ \beta(t) & \omega_{10} + \delta\omega^2(t) \end{bmatrix}$$

where ω_{10} is the frequency of the two CN stretch modes of the molecule in the site representation, and $\beta(t)$ and $\delta\omega^i(t)$ are the coupling constant and the frequency fluctuation of the i^{th} site, respectively. For this vibrational Hamiltonian, the excitonic frequencies (eigenvalues) are given by:

$$\omega_{\pm} = \frac{2\omega_{10} + \delta\omega^1(t) + \delta\omega^2(t) \pm \sqrt{(\delta\omega^2(t) - \delta\omega^1(t))^2 + 4\beta(t)^2}}{2}$$

where $\omega_{\pm}$ represents the frequencies of the symmetric and asymmetric stretch combinations. Thus, the frequencies in the exciton representation do not have a direct correspondence with individual site frequency fluctuations. The lack of CLS change is not surprising since a similar behavior has been previously reported for CIPs involving an anion with strong coupled transitions.[172, 206] In contrast for the samples containing the TDI- mainly as free ions (i.e., LiTDI in BC), the low frequency transition of TDI- presents a slow, but observable, dynamics of the CLS (Figure 3.11 and Table 3.2). The slowdown of the CLS dynamics seen in BC might be associated to the formations of SSIPs, which limits the mobility of the solvent molecules in

Derivation of tau from linear fit

To obtain the time constant from a slow decaying FFCF, the procedure consisted on fitting the function a single exponential decay of the form:

$$y = Ae^{-t/\tau}$$

where A is the amplitude and t is characteristic time, in logarithmic scale. In this case, the exponential decay becomes

$$log(y) = log(A) - t/\tau$$

where the slope of the linear fit is the inverse of the characteristic time.

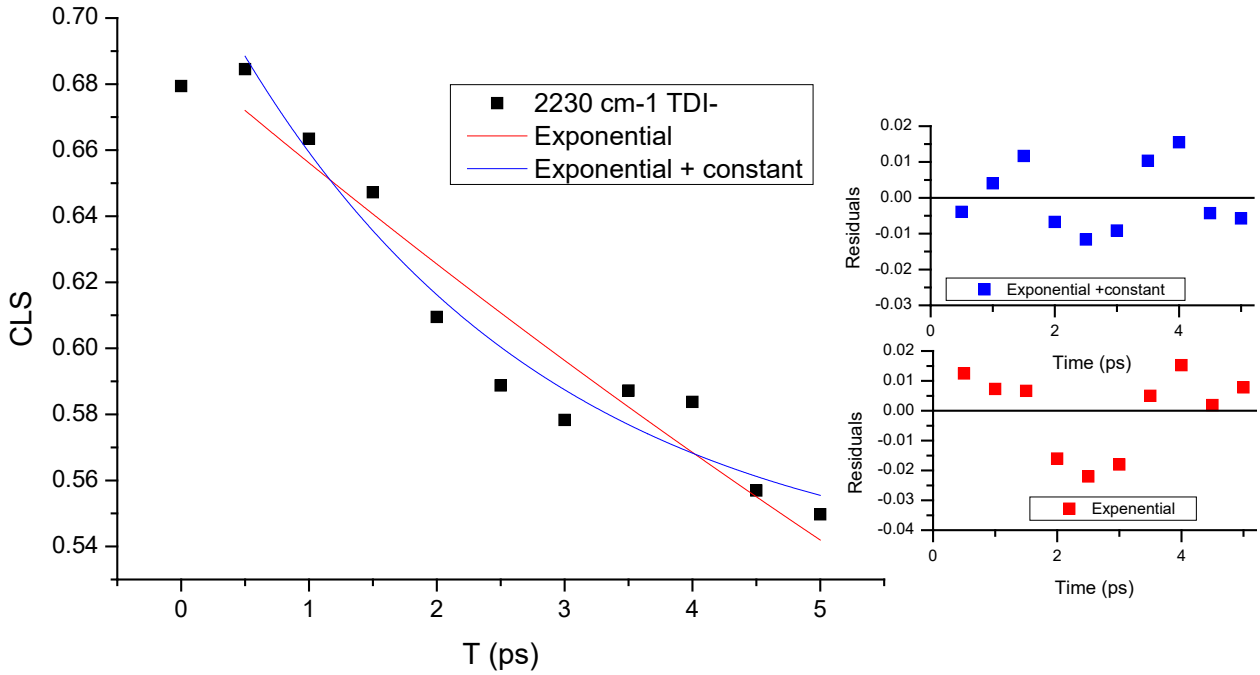

Figure 3.12. CLS fitting of the 2230 cm-1 of LiTDI in DMC. Red and blue represent the fittings with an exponential and an exponential plus a constant, respectively. The plots on the right side showcase the residuals of the fits.

between TDI- and Li+ and results in a slower solvent dynamics than that experienced by the free anion. Finally, the contact ion pairing band at 2245 cm^{-1} of LiTDI in BC shows the nearly constant dynamics, which is in direct correspondence to the observed timescales for the CIP in the DMC solution.

3.4.2. Solvent mixtures

In the previous section, it has been shown that the ability of LiTDI to form CIPs differs substantially by solvent structure (i.e., linear carbonate or cyclic carbonate). Thus, the effect of the solvent composition on the formation of CIPs is derived from the linear IR. The linear FTIR

spectra of LiTDI (X_{Li} = 0.05) for various solvent mixtures shows that the CIP band at 2247 cm^{-1} monotonically rises with increasing DMC composition (Figure 3.7). This result is expected since LiTDI forms a larger amount of CIPs in DMC than BC, as seen in the linear IR of the pure solvents (Figure 3.3). However, it is apparent that the growth of the high frequency band is not linear. The nonlinear behavior is confirmed by plotting the ratio of peak intensities for the high and low bands as a function of solvent composition (Figure 3.13). Remarkably, the amount of CIP appears to have two regions of linear regime. The first region comprises solvent composition from 0 to 0.6 molar fraction of DMC and has moderated change in the CIP concentration as a function of concentration of DMC.

In contrast, the second region ranging from 0.8 to 1 of molar fraction of DMC shows a drastic change, where the amount of CIP is almost double while the solvent composition is only changed by less than 10%. The result clearly indicates that the composition of the Li+ solvation shell significantly affects the formation of CIPs in carbonate mixtures. It is also possible to infer that the lack of cyclic carbonates capable of solvating the cation directly affect the energetics of CIP formation. In other words, the CIP formation is promoted, or becomes energetically more favorable, when the Li+ solvation shell is primarily composed of the linear carbonate.

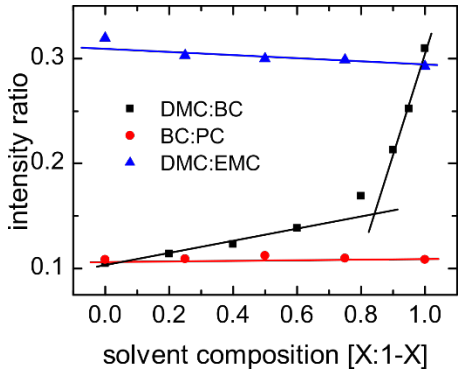

Figure 3.13. Plot of peak intensity ratio of high frequency band over low frequency band of the CN stretch of LiTDI as a function of the solvent composition for three different solvent mixtures: DMC:BC (black squares), BC:PC (red circles), and DMC:EMC (blue triangles). The plotted lines are guides to the eye.

The hypothesis of Li+ having a more favorable CIP energetics for linear carbonates is corroborated by the ratio of the CN stretch bands of TDI- (X_{Li} = 0.05) in mixtures of pure linear carbonates and pure cyclic carbonates (Figure 3.7). The peak intensity ratios for the different mixtures (Figure 3.13) reveal the compelling difference between mixtures of pure linear or pure cyclic carbonates, where the CIP concentration remains nearly constant for different solvent ratios of the BC/PC and DMC/EMC mixtures, versus the mixtures of linear and cyclic carbonates, which exhibit rapid growth of CIP concentration with increasing DMC concentration in the DMC/BC mixtures. These results confirm that the trend is the result of two distinct carbonates (i.e., cyclic and linear) affecting differently the formation of CIPs.

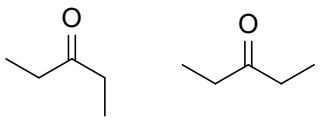

Scheme 3.2. Structure of cis-trans DMC (left) and cis-cis DMC (right).

Table 3.3. Li+ charge as a function of solvation shell composition computed by ab-initio simulations.

Composition	$Li(BC)_{4-X}(DMC)_X$	$Li(BC)_{4-X}(DMC)_X$	$Li(BC)_{4-X}(DMC)_X$	$Li(BC)_{4-X}(DMC)_X$	$Li(BC)_{4-X}(DMC)_X$
DMC	0	1	2	3	4
Li+ charge	0.67	0.67	0.67	0.67	0.69

The molecular mechanism behind the nonlinear trend seen in the CIP concentration as a function of the solvent composition is studied by DFT computations. One potential cause for explaining the difference in the CIP formation is the capacity of the solvent molecules to delocalize the charge of Li+. In other words, it is expected that the solvation shell that better delocalizes the positive charge of Li+ should be less susceptible to form CIPs. To test this possibility, the charge of Li+ in the five possible tetrahedral solvation shells was determined using natural bond orbital analysis (see methods section). The results (Table 3.3) show that there

is very little change in the charge of Li+ as a function of the composition of the solvation shell. Thus, it is unlikely that the observed trend is merely due to a charge delocalization.

Another possible explanation for the nonlinear growth of the CIP concentration in the solvent mixture is related to the energetics of CIP formation (i.e., Li+ + TDI- ↔ LiTDI). It has been previously inferred that the solvation shell composition plays a significant role in the energetics of CIP formation.[6, 50, 157, 209] Thus, to test this possibility the energy trends for the formation of CIP as a function of the solvation shell composition were computed using DFT calculations. The results of these energy calculations are summarized in Figure 3.14. In addition, Table 3.4 contains all possible solvation shells investigated. The energetics shows that the internal energy (ΔE) of CIP formation is highly influenced by the composition of the solvation shell, where larger amount of the linear carbonates in the Li+ solvation shell makes more favorable the CIP formation. This theoretical result is in line with the experimental observations. Moreover, the computations predict an energy difference of ~35 kJ/mol in the stabilization of the CIP when switching from a pure BC to a pure DMC solvation shell, which explains the difference in CIP concentration observed for LiTDI in the two pure carbonates. Additionally, the computational results (Figure 3.14) shows that decreasing BC participation in the Li+ solvation shell results in a non-linear decrease of ΔE of CIP formation.

The equilibrium constant K for CIP formation can be computed from the Gibbs free energy as:

$$K = exp(-\Delta G/RT) = \exp(-\frac{\Delta H}{RT} + \frac{\Delta S}{R})$$

where ΔH and ΔS are the change in enthalpy and entropy of the reaction. Assuming that ΔH≈ΔE and that the ΔS is the same for all the CIP formation reactions, the ratio of the two equilibrium constants associated with two different solvation shells is given by:

$$K_i/K_j = \exp(-\frac{\Delta E_i - \Delta E_j}{RT})$$

where *i* and *j* represent different conditions of the system. The value of the K_i/K_0, computed for the different energetic values corresponding to different solvent compositions and taking as reference the equilibrium constant of CIP formation (K_0) for pure BC, is presented in Figure 3.14. The K_i/K_0 for the different equilibrium constants shows an exponential increase with increasing DMC participation in the solvation shell, which mirrors the trend of the experimental data (Figure 3.13). These results confirm that number and structure of the carbonate in the Li+ solvation defines the energetics of CIP formation in LiTDI. Specifically, Li+ solvation shells with a greater concentration of DMC have the most energetically favorable CIP formation, while higher BC content in the Li+ solvation shell convenes a stabilization to the solvation shell against the CIP formation.

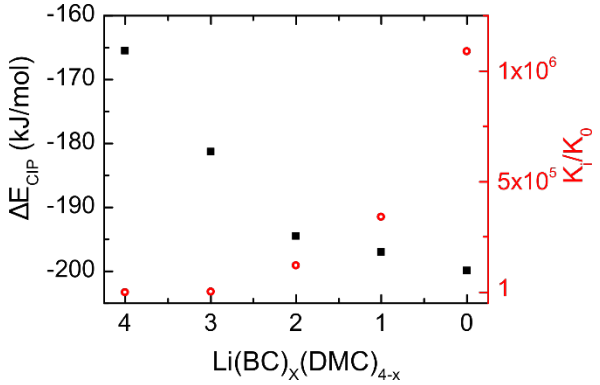

Figure 3.14. Energy and equilibrium constant of CIP formation as a function of solvation shell composition of the free ion. The change in internal energy is shown as black squares and the equilibrium constant is shown in red circles.

The result predicted via DFT computations is confirmed by FTIR spectroscopic experiments. In this case, the amount of CIP is derived from a sample containing LiTDI and LiTFSI in DMC (X_{Li} = 0.07 and X_{TDI}=0.05), where the excess of Li+ is expected to drive TDI- to form quantitative amounts of CIP. From the areas derived from fitting the spectra of X_{Li} = 0.05 LiTDI in DMC, X_{Li} = 0.05 LiTDI in BC, and X_{Li} = 0.07 LiTDI/LiTFSI in DMC (see Figure 3.9),

the corresponding equilibrium constants of CIP formation were calculated. The computed equilibrium constants from the experimental results are summarized in Table 3.5. Approximately 6% of the species in $X_{Li} = 0.05$ LiTDI in DMC are free ions, while the BC sample is dominated by free anions (74%). Thus, the experimental equilibrium constants show a change in two to

Table 3.4. Internal energy for the ion pair formation reaction as a function of the solvation shell structure and composition. DMC structures are located in Scheme 3.2. The values in red correspond to the lowest energy reaction for each case (Figure 3.14 of manuscript).

Reactions	ΔE (kJ/mol)
CIP formation via BC removal	ΔE (kJ/mol)
$Li(ct\text{-}DMC)_3BC^+ + TDI^- \rightarrow Li(ct\text{-}DMC)_3TDI + BC$	-177.86
$Li(ct\text{-}DMC)_2(BC)_2^+ + TDI^- \rightarrow Li(ct\text{-}DMC)_2(BC)TDI + BC$	-174.73
$Li(ct\text{-}DMC)_2(cc\text{-}DMC)(BC)^+ + TDI^- \rightarrow Li(ct\text{-}DMC)_2(cc\text{-}DMC)TDI + BC$	-181.02
$Li(ct\text{-}DMC)(cc\text{-}DMC)(BC)_2^+ + TDI^- \rightarrow Li(ct\text{-}DMC)(cc\text{-}DMC)(BC)TDI + BC$	-180.23
$Li(ct\text{-}DMC)(BC)_3^+ + TDI^- \rightarrow Li(ct\text{-}DMC)(BC)_2TDI + BC$	-170.10
$Li(cc\text{-}DMC)(BC)_3^+ + TDI^- \rightarrow Li(cc\text{-}DMC)(BC)_2TDI + BC$	-178.02
$Li(BC)_4^+ + TDI^- \rightarrow Li(BC)_3TDI + BC$	-165.48
CIP formation via ct-DMC removal	ΔE (kJ/mol)
$Li(ct\text{-}DMC)_4^+ + TDI^- \rightarrow Li(ct\text{-}DMC)_3TDI + ct\text{-}DMC$	-178.46
$Li(ct\text{-}DMC)_2(cc\text{-}DMC)(BC)^+ + TDI^- \rightarrow Li(ct\text{-}DMC)(cc\text{-}DMC)(BC)TDI + ct\text{-}DMC$	-185.01
$Li(ct\text{-}DMC)_3(BC)^+ + TDI^- \rightarrow Li(ct\text{-}DMC)_2(BC)TDI + ct\text{-}DMC$	-180.16
$Li(cc\text{-}DMC)(ct\text{-}DMC)(BC)_2^+ + TDI^- \rightarrow Li(cc\text{-}DMC)(BC)_2TDI + ct\text{-}DMC$	-182.43
$Li(ct\text{-}DMC)_2(BC)_2^+ + TDI^- \rightarrow Li(ct\text{-}DMC)(BC)_2TDI + ct\text{-}DMC$	-175.81
$Li(ct\text{-}DMC)(BC)_3^+ + TDI^- \rightarrow Li(BC)_3TDI + ct\text{-}DMC$	-169.28
CIP formation via cc-DMC removal	ΔE (kJ/mol)
$Li(ct\text{-}DMC)_3(cc\text{-}DMC)^+ + TDI^- \rightarrow Li(ct\text{-}DMC)_3TDI + cc\text{-}DMC$	-190.15
$Li(ct\text{-}DMC)_2(cc\text{-}DMC)(BC)^+ + TDI^- \rightarrow Li(ct\text{-}DMC)_2(BC)TDI + cc\text{-}DMC$	-187.87
$Li(ct\text{-}DMC)(cc\text{-}DMC)(BC)_2^+ + TDI^- \rightarrow Li(ct\text{-}DMC)_2(BC)TDI + cc\text{-}DMC$	-183.50
$Li(cc\text{-}DMC)(BC)_3^+ + TDI^- \rightarrow Li(BC)_3TDI + cc\text{-}DMC$	-178.29
CIP formation via ct-DMC removal and isomerization to cc-DMC	ΔE (kJ/mol)
$Li(ct\text{-}DMC)_4^+ + TDI^- \rightarrow Li(ct\text{-}DMC)_3TDI + cc\text{-}DMC$	-190.49
$Li(ct\text{-}DMC)_3(cc\text{-}DMC)^+ + TDI^- \rightarrow Li(ct\text{-}DMC)_2(cc\text{-}DMC)TDI + cc\text{-}DMC$	-199.92
$Li(ct\text{-}DMC)_2(cc\text{-}DMC)(BC)^+ + TDI^- \rightarrow Li(ct\text{-}DMC)(cc\text{-}DMC)(BC)TDI + cc\text{-}DMC$	-197.04
$Li(ct\text{-}DMC)_3(BC)^+ + TDI^- \rightarrow Li(ct\text{-}DMC)_2(BC)TDI + cc\text{-}DMC$	-192.20
$Li(ct\text{-}DMC)(cc\text{-}DMC)(BC)_2^+ + TDI^- \rightarrow Li\ (cc\text{-}DMC)(BC)_2TDI + cc\text{-}DMC$	-194.46
$Li(ct\text{-}DMC)_2(BC)_2^+ + TDI^- \rightarrow Li(ct\text{-}DMC)(BC)_2TDI + cc\text{-}DMC$	-187.85
$Li(ct\text{-}DMC)(BC)_3^+ + TDI^- \rightarrow Li(BC)_3TDI + cc\text{-}DMC$	-181.31

Table 3.5. Experimental fraction of free anion and equilibrium constants (K_{eq}) derived from ratio of FTIR areas.

X_{Li} = 0.05 LiTDI	Percent of free anion	K_{eq}
in DMC	6%	310
in BC	74%	0.5

three orders of magnitude. This result is in line with the DFT computations where a significant preference for CIP formation is observed for DMC over BC as seen by the computed equilibrium constant ratio. Note that the difference between the equilibrium constants computed from DFT and the experiments could arise from neglecting the entropic part of the Gibbs free energy, which might not be a good approximation in the case of linear carbonates since they can undergo conformational changes.

3.5. Summary

Our study shows that at relatively low concentration LiTDI solution, X_{Li}=0.05 which is approximately half the concentration of Li+ used in commercial batteries, the speciation of Li+ is highly dependent on the solvent molecular structure. In particular, when the solvent is a linear carbonate, the Li+ and TDI- exist predominantly as a CIP. In contrast for cyclic carbonates, Li+ and TDI- are primarily found as free ion and SSIP species. Interestingly, the speciation of Li+ is also highly dependent on the presence of cyclic components in mixtures of linear and cyclic carbonates. Specifically, there is a drastic increase of the CIP concentration with increasing concentration of the linear carbonate. The molecular origin of this behavior is obtained by DFT computations, which reveal that the energetics of ion pair formation is less favored when Li+ contains cyclic carbonates in its solvation shell. Overall, this study provides a molecular-level picture of ion pair formation and its relation to the solvent structure and composition. Thus, the

presented results are relevant to the energy storage industry, where mixtures of linear and cyclic organic carbonates are commonly used for making commercial lithium ion batteries.

CHAPTER 4. THE TALE OF A "NON-INTERACTING" ADDITIVE IN A LITHIUM ION ELECTROLYTE: EFFECT ON IONIC SPECIATION AND ELECTROCHEMICAL PROPERTIES

4.1. Introduction

Lithium ion batteries have become the dominant technology in portable energy storage due to their low weight, cost efficiency, and relatively-high energy density, since their introduction in 1991.[210] Current commercial lithium ion batteries, widely used in portable electronics, are based on a graphite anode, which lacks sufficient energy density to support more energy demanding applications, such as electric vehicles and power grid storage.[60, 211, 212] To this end, lithium metal has the potential of becoming an anode material due to its exceptionally high theoretical specific capacity (3860 $mA.h.g^{-1}$) and low negative electrochemical potential (-3.040 V vs SHE).[213] However, an anode consisting of metallic lithium has inherent problems including dendrite formation (short-circuiting) and unmitigated growth of the solid electrolyte interface (decreased cycling efficiency and increased resistance).[214-216] To solve these issues, highly concentrated lithium salt electrolytes have been proposed. These highly concentrated electrolytes not only inhibit dendrite formation, but also have other desirable properties, such as enhanced electrochemical stability, reduced corrosivity of the aluminum current collector, and the formation of a more stable solid electrolyte interface, so-called SEI.[81, 82, 217] However, highly concentrated electrolytes are not free of problems, since they have high viscosity, low ionic conductivity, and high cost, which hampers

Reprinted with permission from Rushing, J.C., Stern, C.M., Elgrishi, N., and Kuroda, D.G. Tale of a "Non-interacting" Additive in a Lithium-Ion Electrolyte: Effect on Ionic Speciation and Electrochemical Properties. *The Journal of Physical Chemistry C,* **2022,** *126* (4), 2141-2150.

their widespread adoption.[51, 83, 218, 219] One proposed alternative to suppress dendrite formation and reduce cost of the highly concentrated electrolyte is the introduction of a "co-solvent". An essential characteristic of the co-solvent should be to have minimum interactions with the electrolyte components. In other words, the co-solvent is expected to not directly interact with the lithium ion or its counter ion when added to the electrolyte. Previous works with co-solvents include the use of dioxolane, water, acetonitrile, propylene carbonate, diethyl carbonate, toluene, hydrofluroroethers, dichloromethane, hexafluoroisopropyl methyl ether, and 1,1,2,2-tetrafluoroethyl-2,2,3,3-tetrafluoropropylether as co-solvents to battery electrolytes.[22, 23, 28, 31, 84-88] It has been observed that in some cases the addition of co-solvents to highly concentrated electrolytes does not result in the total disruption of rigid three-dimensional structure and in turn creates pockets of highly concentrated electrolyte with increased mobility.[22, 23] For these reasons, these diluted electrolytes have been described as pseudo-concentrated electrolytes. Pseudo-concentrated electrolytes have particularly interesting properties such as enhanced ionic conductivity, lower viscosity, and lower cost when compared to highly concentrated electrolytes.[220] In addition, it has been recently shown the possibility of using these electrolytes for high-voltage lithium-ion batteries.[26, 31]

Highly-halogenated co-solvents have been used to create pseudo-concentrated electrolytes, since they are expected to lower the viscosity of the system without modifying the preexisting interactions among components of the electrolyte due to their chemical inertness. An example of such behavior has been demonstrated in the addition of dichloromethane to a highly concentrated electrolyte where the co-solvent did not alter the electrolyte interfacial properties (i.e., electrochemical stability), but decreased electrolyte viscosity.[24] However, recent work casts doubt on the non-interacting nature of the co-solvent since it revealed that the addition of a

highly fluorinated ether as a co-solvent to a concentrated electrolyte resulted in change of the interfacial and bulk properties of the electrolyte concomitant with a change in the anion speciation in the electrolyte.[26]

The literature of pseudo-concentrated electrolytes also presents conflicting accounts of the role of the co-solvent on the ionic speciation and interfacial and bulk properties of the diluted electrolytes. In a work on a system composed of lithium bis(trifluoromethanesulfonyl)imide (LiTFSI) in ethyl acetate, the addition of a dichloromethane co-solvent did not appear to alter the speciation, which exists primarily as contact ion pairs (CIP) and aggregates (AGG) in the diluted and pure electrolytes.[24] In contrast, an electrolyte consisting of lithium bis(fluorosulfonyl)imide (LiFSI) in dimethyl carbonate showed that the addition of a fluorinated co-solvent directly affects the speciation of the lithium ion by increasing the concentration of CIPs and AGGs in the diluted electrolyte.[25] Owing to these conflicting reports, further study of the solvation structure of the lithium ion when diluted with a "non-interactive" co-solvent is needed.

The focus of this study is to determine the possible molecular mechanisms by which a co-solvent affects the ionic speciation and the electrochemical properties of the system. Previous reports indicated that the chemical nature of the anion occupies a critical role in dictating speciation, so two different lithium salts are investigated to determine whether the identity of the anion plays any part in directing speciation.[152, 221] To this end, two commonly used lithium salts (lithium bis(trifluoromethanesulfonyl)imide, LiTFSI and lithium hexafluorophosphate, $LiPF_6$) in dimethyl carbonate (DMC) and a highly fluorinated solvent (1,1,1,3,3-pentafluorobutane, PFB) are used (Scheme 4.1). It has been demonstrated that both lithium salts are soluble in DMC, though not with the same degree of dissociation, and their use in previous

spectroscopic studies of electrolytes warrants their use here as representative lithium electrolytes.[17, 49, 50, 152, 160, 221-226] The use of PFB as co-solvent is based on the expectation that the solvent by itself will not affect the electrochemical window of the system due to its chemical inertness,[227, 228] but it will improve the transport properties because of its low viscosity.[229]Moreover, PFB is structurally similar to the widely used polymer poly(vinylidene fluoride) typically used as binder in lithium ion batteries. Hence, electrolyte samples with varying co-solvent concentration are examined experimentally via conductivity measurements, viscosity measurements, NMR spectroscopy, linear FTIR spectroscopy, and cyclic voltammetry and complemented by density functional theory (DFT) computations. In particular, previous works have shown the benefits of using IR and NMR characterizations synergistically to study the solvation structure of the lithium ion in solution.[17, 152, 187, 224-226, 230]

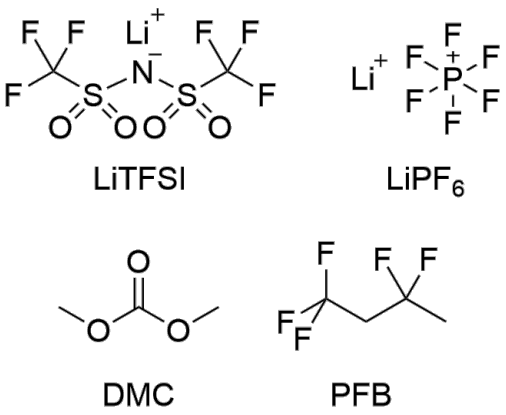

Scheme 4.1. Chemical structures of LiTFSI, $LiPF_6$, DMC, and PFB (from left to right).

4.2. Methods

4.2.1. Experimental methods

4.2.1.1. Sample preparation. Lithium hexafluorophosphate ($LiPF_6$, 98% Acros Organics) was used as received. Lithium bis(trifluoromethanesulfonyl)imide (LiTFSI, 99%) was dried at 140 °C

for 16 hours under vacuum before use. Both lithium salts were stored in a N_2-filled glovebox to avoid exposure to moisture. Dimethyl carbonate (DMC, 98% Acros Organics) and 1,1,1,3,3-pentafluorobutane (PFB, >99.5% Alfa Aesar) were dried under activated 4Å molecular sieves to remove any trace amounts of water before use and stored in a N_2-filled glovebox. Additionally, all solution preparation and sample cell assembly were conducted in the glovebox. The water content of these samples, tested via Karl Fischer titration, was determined to be 12 ppm. The solution concentrations in molarity and molality are included in Table 4.1.

Table 4.1. Molarity and molality of all samples tested.

	1:9:0	1:9:1	1:9:3	1:9:6	1:9:9
LiTFSI molarity	1.03M	0.92M	0.76M	0.60M	0.49M
LiPF6 molarity	1.16M	1.03M	0.83M	0.64M	0.52M
LiTFSI molality	0.91m	0.80m	0.65m	0.50m	0.41m
LiPF6 molality	1.04m	0.90m	0.71m	0.54m	0.44m

Sample cells assembled for FTIR of the carbonyl stretch region utilized a small volume of sample sandwiched between two CaF_2 windows in an O-ring sealed sample cell without a spacer to overcome the known issue of high absorbance for the carbonyl stretch in dimethyl carbonate; this results in a path length of approximately 1-2 μm.

4.2.1.2. FTIR spectroscopy. FTIR spectra were recorded with a Bruker Tensor 27 spectrometer with a liquid nitrogen cooled narrow band MCT detector. All samples were measured with a resolution of 0.5 cm^{-1} and were averaged from 40 scans at room temperature. Attenuated total reflectance FTIR (ATR-FTIR) spectra were recorded on a Bruker Tensor 27 spectrometer outfitted with a Pike Miracle ATR cell and diamond/ZeSn crystal. The ATR-FTIR spectra were

captured using a deuterated triglycine sulfate (DTGS) detector with a 4 cm^{-1} resolution, averaged over 16 scans.

4.2.1.3. Conductivity and viscosity measurements. Conductivity and viscosity measurements were taken with a YSI 3200 conductivity meter and a Brookfield DV-II+ Pro viscometer, respectively.

4.2.1.4. NMR spectroscopy. Nuclear magnetic resonance spectroscopy was taken on a Bruker AVIII 500 MHz spectrometer. Shimming was performed with a chloroform reference. Hexafluorobenzene (C_6F_6) was used as the reference standard in all samples; sealed capillary tubes of C_6F_6 were inserted into each NMR tube to ensure no direct interactions occur between the reference standard and the sample.

4.2.1.5. Electrochemical methods. Linear sweep voltammetry experiments were performed with an SP-300 Biologic potentiostat. The scans were conducted at a 100 mV/sec scan rate. For all the samples, the working and counter electrodes were made of platinum and Ag/Ag^+ was used as a pseudo-reference electrode. For comparison to the Li/Li^+ standard used in much electrochemical literature, scans were also conducted with the addition of a small amount of ferrocene (as an absolute internal standard) and referenced versus Li/Li^+ using a conversion as outlined in the literature.[231, 232] Onset potentials were determined as the intersection potential of the tangent lines to the capacitive and faradaic currents.

4.2.2. Theoretical methods

4.2.2.1. DFT calculations. Density functional theory (DFT) calculations were performed in the Gaussian 09 software to complement experimental NMR data.[188] Geometry optimizations and chemical shifts were computed using the PBE functional and the 6-311++G** basis set. The functional and basis set were chosen based on previous demonstration that they correctly model

lithium solvation shell and their speciation in solution.[13, 152, 157, 209, 233-235] NMR chemical shifts were calculated using the Gauge-Independent Atomic Orbital (GIAO) method.[236]

4.3. Results

4.3.1. FTIR spectroscopy

The FTIR spectra in the carbonyl stretch region (1650-1850 cm^{-1}) for the samples containing either $LiPF_6$ or LiTFSI in solvent mixtures with different molar ratios of DMC and PFB are shown in Figure 4.1. The spectra for both samples show two bands with a 2:1 intensity ratio separated by ~ 35 cm^{-1}. In LiTFSI samples, the high and low frequency bands are located at 1757 cm^{-1} and 1724 cm^{-1} respectively. The initial addition of PFB slightly decreases the height ratio between the high and low frequency bands, but it remains almost equal when the concentration of PFB is further increased. Similar spectra are observed for the $LiPF_6$ samples. However, the higher frequency band (1760 cm^{-1}) increases its intensity with the addition of PFB.

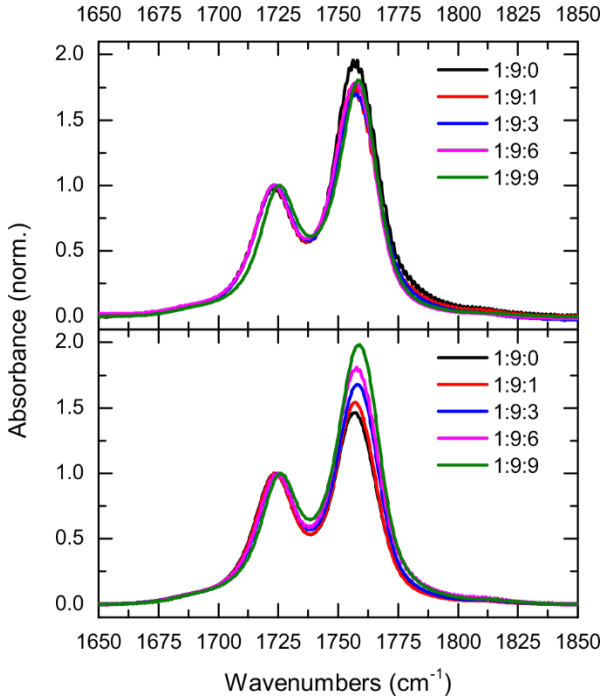

Figure 4.1. FTIR spectra of the carbonyl stretch region for LiTFSI:DMC:PFB samples (top) and $LiPF_6$:DMC:PFB samples (bottom) as a function of the PFB concentration.

Moreover, the lower frequency band (1725 cm^{-1}) shows a noticeable blueshift with increasing PFB concentration.

Complementarily, Figure 4.2 shows the ATR-FTIR spectra in the P-F stretch region for the $LiPF_6$ samples. There are five bands at 818 cm^{-1}, 844 cm^{-1}, 857 cm^{-1}, 863 cm^{-1}, and 885 cm^{-1} in these samples. While the bands at 844 cm^{-1} and 863 cm^{-1} are present at all compositions, the bands at 818 cm^{-1}, 857 cm^{-1}, and 885 cm^{-1} are only visible at PFB concentrations of 1:9:3 $LiPF_6$:DMC:PFB or greater. In addition, the peaks at 844 cm^{-1} and at 863 cm^{-1} blueshift with increasing PFB content, while the other three bands appear to only grow with increasing PFB content.

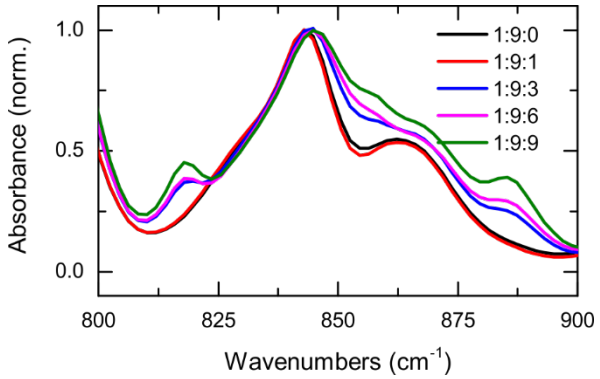

Figure 4.2. ATR-FTIR in the P-F stretch region for different $LiPF_6$:DMC:PFB samples.

4.3.2. NMR spectroscopy and electrochemical methods

NMR experiments were also performed to investigate the anion speciation using the ^{19}F nuclei, since the $TFSI^-$ does not have easily identifiable vibrational modes that change with speciation. The chemical shifts for both lithium salts in the different solvent mixtures are presented in Figure 4.3. The ^{19}F nuclei in $LiPF_6$ samples show a decrease of the chemical shift with increasing concentration. Conversely, the LiTFSI samples present an up-shift in the chemical shift with increasing PFB.

Additionally, the molal conductivity of $LiPF_6$:DMC:PFB and LiTFSI:DMC:PFB samples at several concentrations at room temperature was also studied, and the results are presented in Figure 4.4 with respect to both PFB concentration and Li concentration. The conductivity of the LiTFSI:DMC:PFB samples is almost constant at ~ 5 $mS \cdot cm^{-1} \cdot m^{-1}$, save for the 1:9:0 sample, which shows slightly lower conductivity. For the $LiPF_6$:DMC:PFB samples, the conductivity generally shows a steady increase with PFB concentration. The viscosity measurements of all samples are shown in Figure 4.4. The viscosity decreases with PFB concentration for all compositions for both LiTFSI and $LiPF_6$ samples.

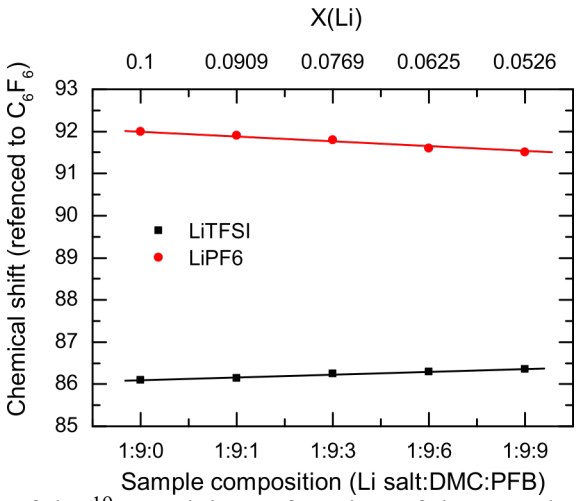

Figure 4.3. Chemical shift of the ^{19}F nuclei as a function of the sample composition (bottom axis) and molar fraction of lithium (X(Li), top axis) for both LiTFSI:DMC:PFB samples (black squares) and $LiPF_6$:DMC:PFB samples (red circles).

Finally, the electrochemical response of the samples was also studied via cyclic voltammetry (Figure 4.5). For this study, two different limiting PFB concentrations (1:9:0 and 1:9:9) were studied for both $LiPF_6$ and LiTFSI electrolytes. In the $LiPF_6$ samples, the voltage ranges show the onset of oxidation occurs at 6.48 V vs Li/Li^+ for the 1:9:0 concentration and 6.47 V vs Li/Li^+ for 1:9:9, while in the case of LiTFSI samples, oxidation occurs at 5.94 V vs Li/Li^+ for the 1:9:0 sample and 5.82 V vs Li/Li^+ for the 1:9:9 sample.

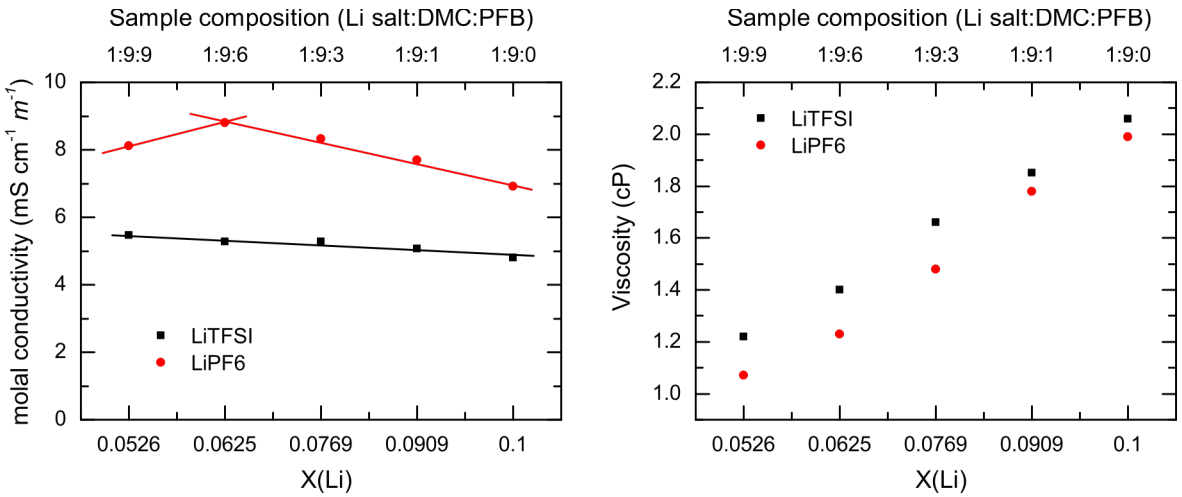

Figure 4.4. Left panel contains the molal conductivities of $LiPF_6$/DMC/PFB (red circles) and LiTFSI/DMC/PFB (black squares) samples with respect to sample composition (top axis) and molar fraction of lithium (X(Li), bottom axis). Right panel depicts the viscosities for LiTFSI and $LiPF_6$ samples with respect to sample composition (top axis) and molar fraction of lithium (X(Li), bottom axis). Conductivities were taken at room temperature, 25°C. Temperature was held at 23°C during viscosity measurements via a circulating chiller.

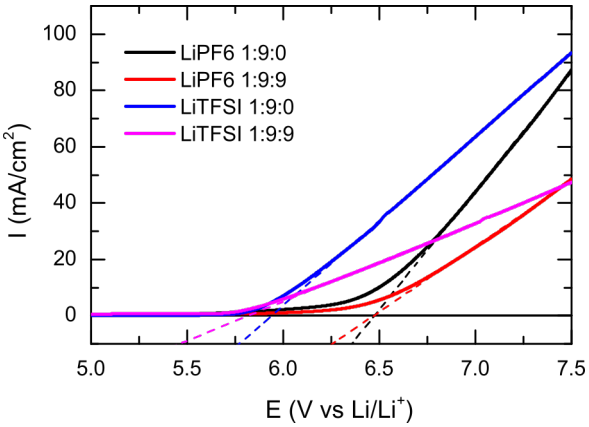

Figure 4.5. Linear sweep voltammogram for 1:9:0 and 1:9:9 compositions of the $LiPF_6$:DMC:PFB (black and red lines, respectively) and LiTFSI:DMC:PFB (blue and magenta lines, respectively) samples. The intersection of the dashed lines with I=0 mA/cm^2 provides a qualitative difference of the onset potential. The change in current density over a varied potential range is plotted for the oxidative scan of the first trace for each composition at a 100 mV/sec scan rate.

4.4. Discussion

4.4.1. Ionic speciation

The carbonyl stretching mode of the organic carbonate in the electrolytes has been previously used as a vibrational probe to study solvation shell structure and ion speciation

because of its sensitivity to local interactions.[237-241] In our study, the carbonyl stretching mode of DMC was used as a vibrational probe to investigate changes in the local lithium ion environment produced by the addition of PFB concentration, since the high and low frequency band (1757 cm^{-1} and 1724 cm^{-1}) have been assigned to the free carbonyl and lithium coordinated carbonyl stretches, respectively.[17, 117, 242] The linear FTIR spectra for LiTFSI and $LiPF_6$ samples (Figure 4) show definitely different trends in association of the solvent with the lithium ion for the two salts. In the case of the LiTFSI samples, the spectra reveal a downward trend where the amount of free carbonate is maximized for the sample without PFB, and the first addition of PFB slightly lowers the amount of free solvent, which then remains almost constant for all the different PFB concentrations. This trend implies that PFB is not likely to directly interact with Li^+; this interpretation is further strengthened by DFT results (see Figure 4.6), which predict IR signatures from the interaction between Li+ and PFB, which are not present in the experimental data.

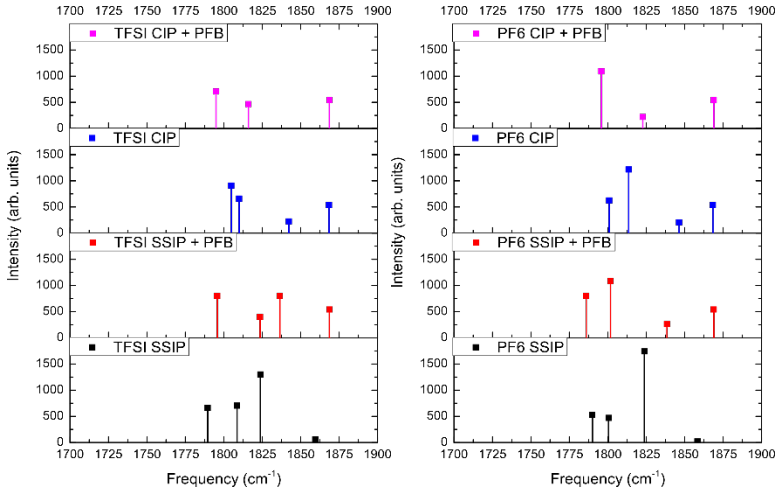

Figure 4.6. Calculated IR frequencies for carbonyl region of LiTFSI (left) and $LiPF_6$ (right) ion pair species with the addition of PFB (Scheme 4.2). The frequencies for the SSIP and CIP species without PFB are included for comparison.

However, it appears that the addition of PFB to the LiTFSI samples actually enhances the interaction of the organic carbonate with lithium ion. This is explained by the extremely poor

solubility of LiTFSI in PFB, even though PFB has a larger dielectric constant than DMC.[243] In regards to ion speciation, the changes in the carbonyl stretch band intensities indicate that in the absence of PFB (the 1:9:0 LiTFSI sample), some CIPs are present, but the addition of PFB (the 1:9:1 sample) is sufficient to disrupt such complexes, resulting in a higher coordination of lithium ions by carbonates, or equivalently, in the loss of intensity for the free carbonyl band (1757 cm^{-1}). Moreover, subsequent additions of PFB do not appear to change the free carbonate solvent molecules or the ionic speciation in the sample, since the ratio of the bands does not change. Note that the loss in intensity of the free carbonyl band could also be attributed to a change in the dielectric constant of the solution by the addition of PFB, but this is unlikely because the ratio of the bands intensity remains invariant even at very large concentrations of PFB. The solvation structures described are shown in Scheme 4.3.

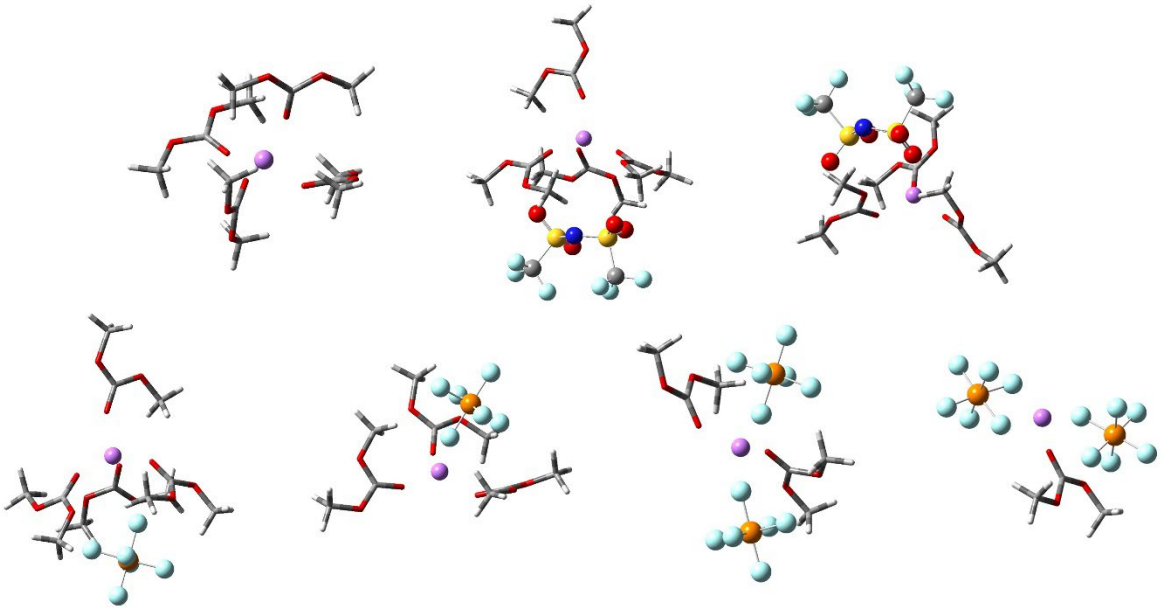

Scheme 4.3. Possible Solvation structures. Top row, from left to right: Solvated Li+, LiTFSI SSIP, LiTFSI CIP. Bottom row, from left to right: $LiPF_6$ SSIP, $LiPF_6$ CIP, $LiPF_6$ 2,2-AGG, $LiPF_6$ 1,2-AGG.

The linear IR spectra of the $LiPF_6$ samples (Figure 4) also show two bands in almost the same positions as the LiTFSI samples. Compared to the bands in the latter, the carbonyl stretch

bands are blueshifted by 1 cm^{-1} and 3 cm^{-1}, respectively. Interestingly, the trend observed for the peak intensity of the LiTFSI samples is completely different for the $LiPF_6$ samples, where a sustained growth of the free carbonyl band is observed with increasing PFB concentration. The trend in the carbonyl bands shows that more free solvent molecules are generated with increasing concentration of PFB. While the addition of PFB could significantly alter the oscillator strength of the carbonyl mode of DMC, this effect should be also noticeable in the LiPF6 samples. However, the PFB addition to the LiPF6 samples only produces a small solvatochromic shift of the carbonyl stretch frequency.[244] Thus changes in the environment do not appear to be caused by substantial change in the transition dipole magnitude of the carbonyl stretch. The effect of PFB can be explained by an increase in the interaction between the lithium ion and its counter ion, which results in more CIPs and AGGs in the $LiPF_6$ samples with increasing PFB concentration. The formation of more CIPs and AGGs is also supported by the broadening revealed in the high-frequency band with increasing PFB concentration, which may denote additional vibrational modes from CIPs or AGGs contributing to the high-frequency band.[50] This is reflected in the IR frequencies calculated from density functional theory (Figure 4.7), which shows that the high-frequency carbonyl band observed for the free species overlaps with bands predicted for the SSIP, CIP, and 2,2-aggregate species (structures B, C, and D in Scheme 4.4). Furthermore, previous experimental and computational studies on $LiPF_6$ in DMC suggest that the solution exists primarily SSIPs, such that stronger Li-anion interactions would result in aggregate species. [49, 50, 149]

The change in the speciation of the PF_6^- ion is further deduced from ATR-FTIR spectroscopy. The P-F stretches of the anion in the $LiPF_6$ in DMC/PFB samples (Figure 4.2) show that, in the absence of PFB (1:9:0 sample), the ATR-IR spectrum presents two broad

bands, one at 840 cm^{-1} and a second one at 860 cm^{-1}. This latter band has been previously linked to the presence of SSIPs.[17, 49, 152] At higher concentrations of PFB (1:9:3 and higher), three additional bands appear at 820 cm^{-1}, 857 cm^{-1} and 885 cm^{-1}, suggesting a change in the ionic speciation of PF_6^- . The proposed change in speciation is in agreement with a previous report which showed the appearance and growth of the same side P-F stretch bands at high concentrations of $LiPF_6$ in organic carbonates, where the interaction between the lithium ion and its counter ion is enhanced by concentration.[50]

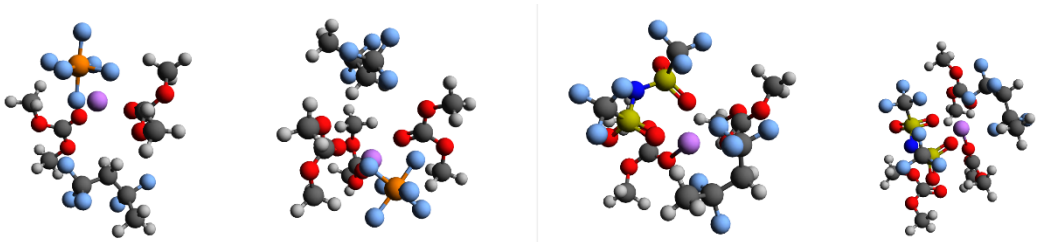

Scheme 4.2. Contact ion pair with the explicit carbonates and PFB in the solvation shell. From left to right: $LiPF_6$ CIP, $LiPF_6$ SSIP, LiTFSI CIP, LiTFSI SSIP.

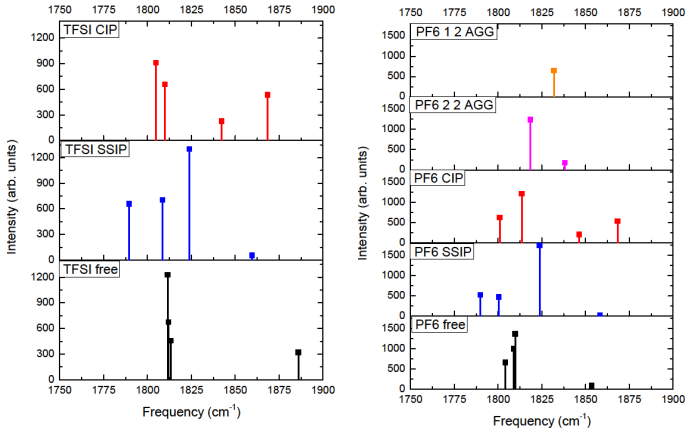

Figure 4.7. Calculated IR frequencies for the carbonyl stretch of the solvent for $LiPF_6$ and LiTFSI species without addition of PFB (all species are shown in Scheme 4.4).

Moreover, this previous study also assigned the same P-F stretch bands, observed for the 1:9:3 samples and beyond, to the formation of aggregates.[50] Hence, the $LiPF_6$/DMC/PFB samples show increased ionic interactions with higher PFB concentrations. This behavior is in agreement with the increase in free carbonate molecules seen in the carbonyl stretch band for the

samples with high PFB concentrations.[26] DFT frequency calculations for the different $LiPF_6$ species validate our assignment, since the P-F stretch region (Figure 4.8) has a better agreement

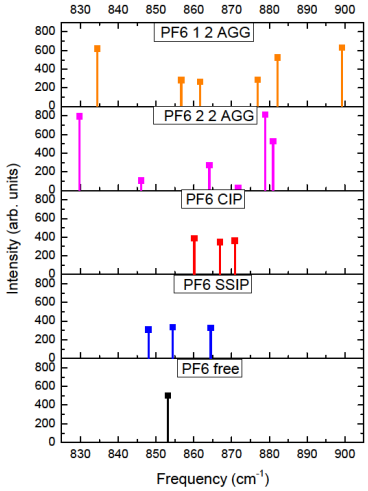

Figure 4.8. Calculated IR frequencies in the P-F stretching region for different $LiPF_6$ speciation (Scheme 4.4).

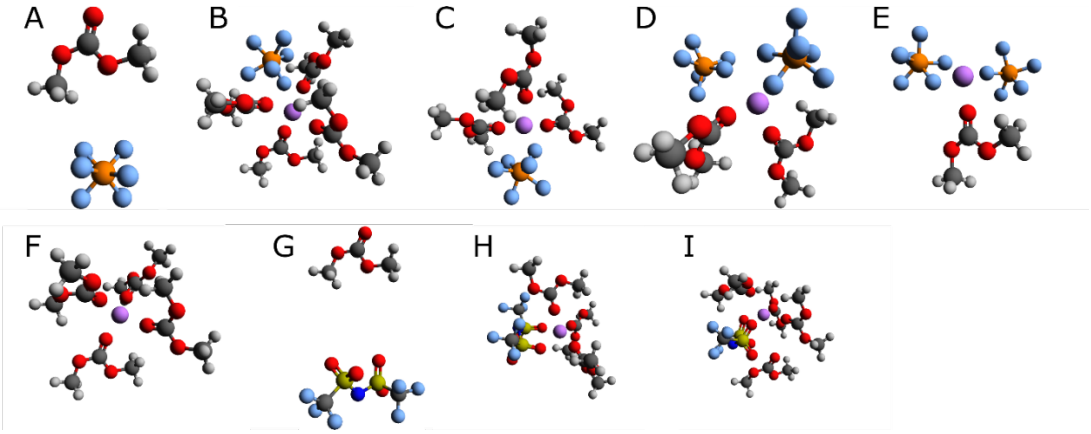

Scheme 4.4. All species investigate via DFT computations: Free PF_6^- anion (A), $LiPF_6$ SSIP (B), $LiPF_6$ CIP (C), $LiPF_6$ 2,2-AGG (D), $LiPF_6$ 1,2-AGG (E), solvated Li^+ cation (F), free TFSI- anion (G), LiTSFI CIP (H), and LiTFSI SSIP (I).

for frequencies of the free anion and the SSIP than for those of the CIP. Furthermore, the calculations also reveal the IR bands seen in FTIR (Figure 4) and the three additional IR bands observed in ATR (Figure 4.2) spectra with increasing PFB concentration are better represented by the carbonyl and P-F stretches arising from the 2,2-aggregate, rather than from the 1,2-aggregate (structures D and E in Scheme 4.4). In summary, the change in the speciation of PF_6^-

is consistent with behavior in pseudo-concentrated electrolytes, wherein the presence of a non-interacting co-solvent strengthens the cation-anion interactions.[25, 26]

The anion speciation was also inferred from the fluorine nuclei chemical shifts. As seen in the IR spectroscopic data, the LiTFSI and $LiPF_6$ samples present opposite trends for the change in the chemical shift (Figure 4.3). While the PF_6^- fluorine nuclei decrease their chemical shift (increasingly shielding) with PFB concentration, the TFSI fluorine atoms increase their chemical shift (less shielding). From the perspective of the sample concentration, an increase in the lithium concentration should lead to a decrease of the chemical shift (increasingly shielding) due to the stronger interaction between the anion and the cation as previously demonstrated for a TFSI-based ionic liquid doped with LiTFSI.[245] DFT calculations (Figure 4.9) validates the concentration effect in the NMR chemical shift since the formation of a CIP results in a decrease of the chemical shift (more shielded) of anion fluorine nuclei in either sample. Moreover, the addition of an explicit solvation shell for Li^+ does not modify the chemical shift trend (Figure 4.9). Hence, the DFT results confirm our interpretation of the IR data for both the PF_6^- and $TFSI^-$. In other words, the addition of PFB to the $LiPF_6$ sample leads to a stronger lithium-anion interaction, resulting in more shielding of the fluorine nuclei (lower chemical shift) and more free carbonates. In contrast, the addition of PFB to the LiTFSI sample results in a weaker interaction between the cation and $TFSI^-$, or equivalently, higher chemical shift (less shielding) in agreement with disappearance of free carbonates in the sample as seen from the IR results. So far, two key conclusions can be extracted from the experimental IR and NMR data and the computational results. First, the addition of PFB appears to affect the Li-anion interaction differently for the two samples. Second, the presence of the co-solvent has a stronger effect on the formation of CIPs and AGGs than lowering the lithium concentration. Hence, the addition of

the co-solvent affects the speciation of the two electrolytes differently, which points to different molecular interactions between PFB and either anion. DFT calculations (see Table 4.2) revealed that the interaction between the most energetically favored conformation of $TFSI^-$ and PFB is favored by ~3.6 kJ/mol over the interaction between PF_6^- and PFB (see Scheme 4.5).

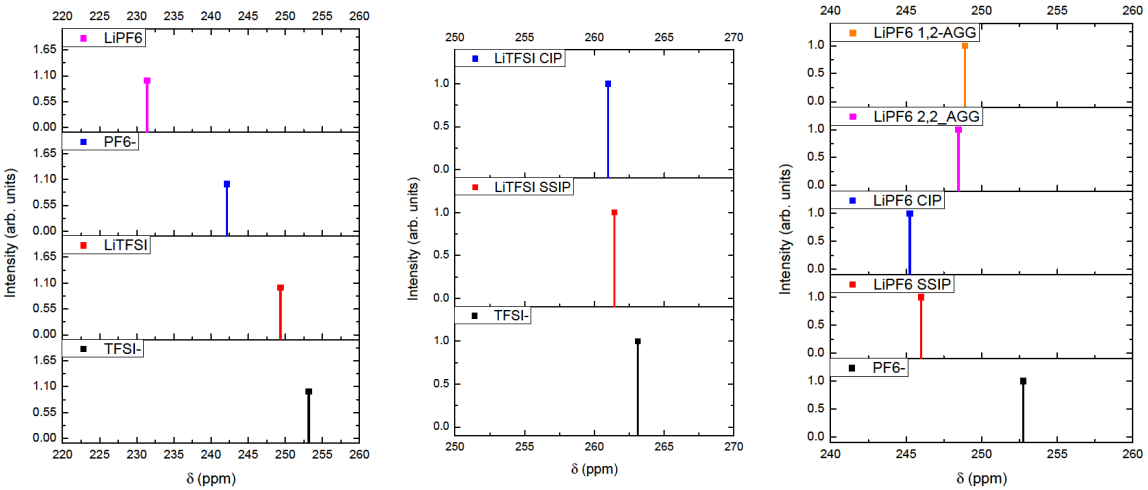

Figure 4.9. Calculated NMR shielding for the addition of Li^+ to PF_6^- and TFSI- anions. Left panel without solvent, and middle and right panels with explicit solvent (as shown in Scheme 4.4).

Previous work has shown the existence of weak hydrogen bonds between C-H donors and the O atom of acceptors.[246-250] These CH…O hydrogen bonds have energetics on the order of 1 kcal/mol, different C-H bond lengths as compared to non-forming hydrogen bonded species, and nearly linear CH…O geometries.[246, 247, 251, 252] The PFB-TFSI interaction show similar energetics of ~0.86 kcal/mol to the CH…O hydrogen bond. Additionally, bond lengths for the C-H bonds of PFB and C-H-O bond angles (Table 4.3) mirror results previously seen in other systems (see ref. [251] and [247], respectively). Thus, the DFT results strongly suggest that the formation of weak hydrogen bonds between PFB and the $TFSI^-$ might be the cause for the dissociation of the CIPs in the LiTFSI/DMC samples. Overall, the juxtaposing results from IR, NMR, and DFT data provide a unified picture of the molecular-level

interactions in these systems. The IR experiments show more free solvent molecules with increasing co-solvent concentration for the $LiPF_6$/DMC system due to enhanced interactions between the PF_6^- and the lithium cation. Conversely, for the LiTFSI/DMC system, there is a slight loss of free solvent molecules with the initial introduction of PFB, indicating that the co-solvent dissociates ion pairs (SSIPs and CIPs) and forces the carbonate solvent to solvate Li^+. In the case of the PF_6^- sample, the enhanced cation-anion interactions are also observed through both the down shift of fluorine chemical shift and the appearance of new bands in the P-F stretch IR region. In contrast, the weakening of Li^+-anion interaction produced by the presence of the co-solvent in the LiTFSI/DMC sample is directly observed from the up shift of the fluorine chemical shift. The NMR and IR spectra for these samples calculated with DFT strengthen the interpretation of these interactions, denoting the existence of free $TFSI^-$ and SSIPs in the LiTFSI samples and free PF_6^-, SSIP, and 2,2-aggregate species in the $LiPF_6$ samples.

4.4.2. Macroscopic properties

The electrophysico-chemical properties of these systems also present interesting trends. The molal conductivity of both systems shows that the value remains nearly constant with a slight increase for those samples containing PFB for the LiTFSI samples. In contrast, the $LiPF_6$ samples present a maximum around the 1:9:6 sample, but all the samples containing PFB have a larger conductivity than the pure electrolyte (1:9:0 sample). In these electrolytes, the conductivity mechanism is expected to be driven by the mobility of free ions, the viscosity, and the lithium salt concentration.[6] The formation of CIPs and AGGs should limit the number of charge carriers and thereby lower the conductivity of the system. However, the addition of a co-solvent to an electrolyte not only changes the number of charged species, but also alters the

viscosity of the system. Thus, a lower viscosity in the sample should facilitate a faster diffusion of the charge carriers, which is observed behavior for pseudo-concentrated electrolytes.[23, 25]

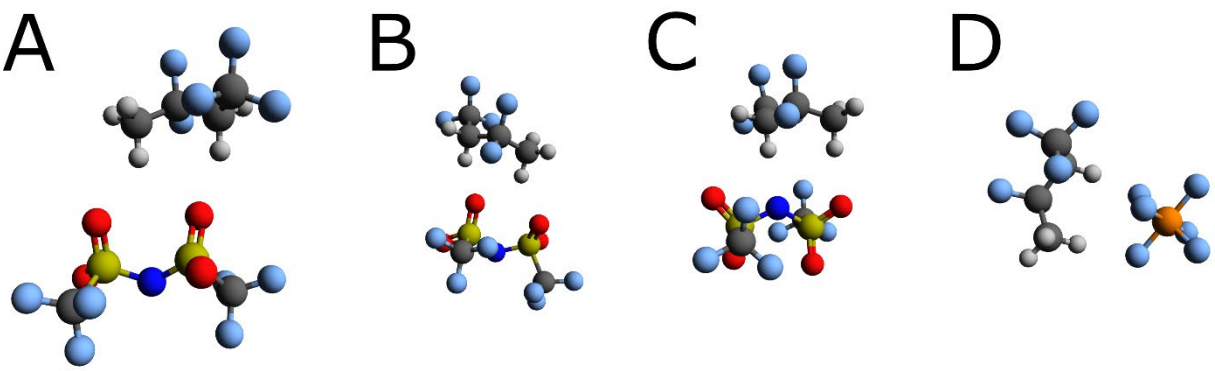

Scheme 4.4. The atomistic structures used to investigate the hydrogen bond energetics for each anion (Table 4.2).

Table 4.2. Energetics for the interaction between PFB and each anion (Scheme 4.5).

Interaction	ΔE (vs cis-cis TFSI-)	ΔE (vs cis-trans TFSI-)	ΔE (vs PF_6^-)
(A)PFB(H) --- ccTFSI(O)	-51.43 kJ/mol	-48.05 kJ/mol	-
(B) PFB(H) --- ccTFSI(O)	-53.84 kJ/mol	-50.45 kJ/mol	-
(C) PFB(H) --- ctTFSI(O and N)	-59.02 kJ/mol	-55.64 kJ/mol	-
(D) PFB(H) --- PF_6(F)	-	-	-55.40 kJ/mol

Table 4.3. C-H bond lengths and bond angles (C-H-O and C-H-N) for the most favorable TFSI-PFB interaction (C in Scheme 4.5). C-H bond lengths in non-interacting TFSI- are included for comparison.

Sample	C-H bond length (CH_2)	C-H bond length (CH_3)	C-H-O bond angle	C-H-N bond angle
TFSI-	1.0921 Å	1.0908 Å	---	---
TFSI-PFB	1.0955 Å	1.0922 Å	165°	170°

The viscosity of the studied electrolytes as a function of the PFB concentration in either sample displays a monotonic decrease of the viscosity with the addition of co-solvent. Since viscosity and conductivity are inversely related, a monotonic decrease in viscosity should be reflected as an increase in the conductivity when the ionic speciation in the sample remains unaltered. This is the case for the LiTFSI samples, where the addition of PFB leads to a linear

increase in the conductivity. However, the trend does not explain the conductivity of the $LiPF_6$ samples, which exhibits nonlinear behavior, likely due to a change in the ionic speciation as previously concluded.[253] Moreover, the viscosity of the $LiPF_6$ samples does not follow an ideal behavior in which the viscosity of the system is defined exclusively by the viscosity of the components and their molar fractions. The non-ideal behavior is seen when comparing the real and ideal viscosity of the mixtures (Figure 4.10), in which the latter was computed using the viscosity of the pure electrolytes and pure PFB.[228] In this case, it is observed that the experimental viscosities for the LiTFSI samples matches well with the value of the viscosity predicted for the ideal case. In contrast, the experimental viscosity for the $LiPF_6$ samples presents a much lower value than that of the ideal case. Thus, the viscosity evidences a change in the cohesive forces of the electrolyte likely arising from the change in the ionic speciation of the $LiPF_6$ sample due to the presence of PFB.

The effect of dilution in the samples on the ion transport is better observed using the viscosity weighted conductivity (Walden product, Figure 4.10) as a function of the PFB concentration. Because the Walden product removes the viscosity effect, one can use this metric to evaluate the changes in the number of charge carriers.[254] For the LiTFSI sample, the Walden product (Figure 4.10) decreases monotonically, since it is directly influenced by the change in the number of charge carriers produced by the addition of the co-solvent; i.e., dilution. Contrarily, the Walden product (Figure 4.10) for the $LiPF_6$ samples does not follow the same trend as LiTFSI, indicating that there is another underlying molecular mechanism, beyond simple dilution, altering the properties of the system. This mechanism is the change in ionic speciation of the two systems as derived from the IR and NMR experiments. Hence, the Walden products assert that PFB plays a different role in the solvation of these $LiPF_6$ and LiTFSI electrolytes and

their dilutions. In the case of the LiTFSI system, PFB has a minimal effect on the conductivity of the system and only serves as a co-solvent, while in the $LiPF_6$ system, PFB creates a pseudo-concentrated electrolyte with enhanced conductivity by altering the ionic speciation of the electrolytes; i.e., creating more aggregates.

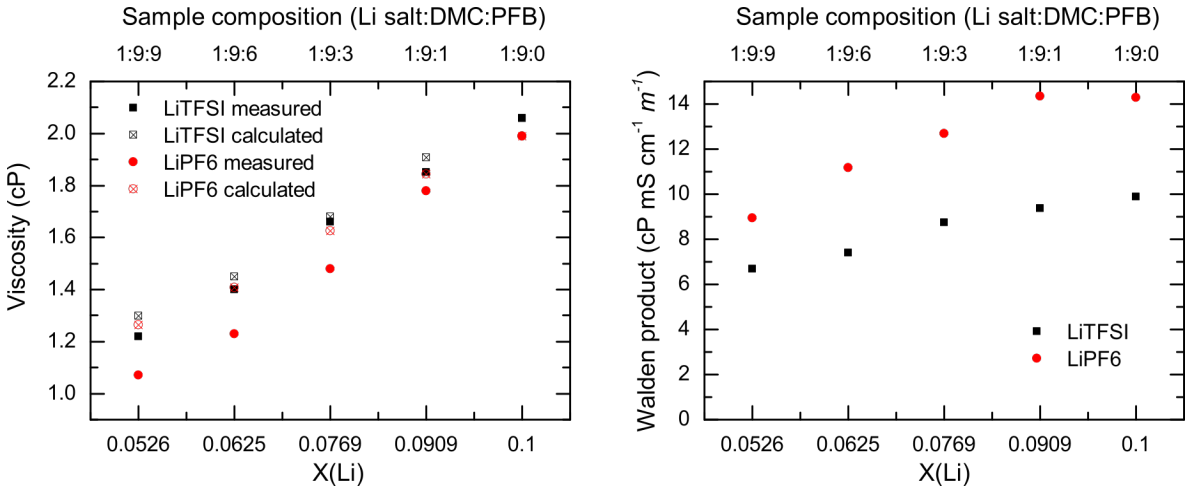

Figure 4.10. Left panel depicts the measured and calculated viscosities for LiTFSI/DMC/PFB (black full and crossed squares) and $LiPF_6$/DMC/PFB (red full and crossed circles) samples. Right panel shows the Walden product for LiTFSI and $LiPF_6$ samples at all compositions.

Finally, the effect of PFB on the electrochemical stability of the electrolyte was also evaluated from cyclic voltammetry. It has been previously shown that there is a relationship between enhanced ionic conductivity and a change in electrochemical stability of the electrolytes, in which a higher concentration of the lithium salt typically leads to larger electrochemical stability.[82, 85, 87] The linear sweep voltammogram (Figure 4.5) for $LiPF_6$ sample without (1:9:0) and with (1:9:9) PFB shows that the onset potential for oxidation is 6.48 V and 6.47 V for the two samples, respectively. The results indicate a negligible (~ 10 mV) change in the electrochemical window upon addition of PFB for the $LiPF_6$ electrolyte. The LiTFSI samples show a completely different behavior, where the onset oxidation potential is found to be 5.94 V and 5.82 V for the pure (1:9:0) and diluted (1:9:9) sample, respectively. Thus in the LiTFSI electrolyte, the electrochemical stability window is reduced by ~120 mV when

PFB is added. Addition of PFB lowers the oxidative current densities in both electrolytes, however the effect of PFB addition on the onset potentials differs depending on the lithium salt in the electrolyte. The electrochemical results appear to be conflicting, but the change in the bulk ionic speciation of the samples explains the observed electrochemical behavior, since it has been previously observed that an increase in the cation-anion interaction leads to a larger electrochemical window of the electrolyte.[82, 108]

Table 4.4. The HOMO-LUMO gap, computed via DFT, for different species of LiTFSI and $LiPF_6$.

Species	HOMO-LUMO gap
Free $TFSI^-$	2.51 eV
LiTFSI SSIP	7.23 eV
LiTFSI CIP	7.51 eV
Free PF_6^-	3.92 eV
$LiPF_6$ SSIP	8.10 eV
$LiPF_6$ CIP	8.57 eV
$LiPF_6$ 2,2-AGG	8.05 eV
$LiPF_6$ 1,2-AGG	4.98 eV

To find a possible link and rationalize the effect of the bulk ionic speciation on the observed electrochemical behavior, the HOMO-LUMO gap of the different ionic species deduced from the experiments is calculated using DFT computations (see methods). This method is used because it has been previously shown that the HOMO-LUMO gap is correlated with the electrochemical stability.[255-257] The HOMO-LUMO gap for the free anion, SSIP, and CIP of both salts, as well as aggregate species are shown in Table 4.4. In the species related to LiTFSI, the HOMO-LUMO gap is found to be similar for the CIP and SSIP, but significantly smaller for the free $TFSI^-$. A similar trend is seen for the $LiPF_6$ species (free PF_6^- < 1,2-AGG < 2,2-AGG ≈ SSIP ≈ CIP), albeit the consideration of aggregates as previously demonstrated. Thus, the electrochemical data allow us to deduce the same molecular mechanism resulting from the

addition of PFB to the two electrolytes. In the case of the LiTFSI sample, a weaker interaction between Li^+ and its counter ion resulting in less ion pairs (both SSIPs and CIPs) and more free ions is observed when PFB is added. These changes in speciation cause a decrease in the electrochemical window. In contrast, the addition of the co-solvent leads to a stronger Li-anion interaction in the $LiPF_6$ electrolyte, which leads to the formation of more CIP and AGGs in the sample and maintains the electrochemical window constant. Overall, the contrasting behaviors observed in the electrochemical stability of the samples reflect a shift in speciation toward more free ions (with reduced electrochemical stability) in the case of the LiTFSI electrolytes and a shift towards aggregates (with similar electrochemical stability) in the case of the $LiPF_6$ electrolytes.

4.5. Summary

Two non-aqueous lithium ion electrolytes and their dilutions with a co-solvent were characterized using experimental and computational methods. Complementary IR and NMR spectroscopies showed a different speciation for the two electrolytes with increasing concentration of the co-solvent. In the case of the $LiPF_6$ electrolyte, the anion forms aggregates when PFB is added, while the addition of co-solvent actually dissociates CIPs in the LiTFSI electrolyte. The change in the speciation is also observed in the different electrophysico-chemical properties of the systems. The stronger Li-anion interactions in the $LiPF_6$ electrolyte result in a higher conductivity, lower viscosity, and no change in the electrochemical window with the addition of the co-solvent. In contrast, the conductivity of the LiTFSI electrolyte remains fairly constant irrespective of the PFB concentration, while the addition of co-solvent decreases both the viscosity and the electrochemical window. The lower oxidative stability is in agreement with the change in the speciation and their computed electrochemical stability via the

HOMO-LUMO gap. The difference in speciation appears to be caused by the formation of a strong hydrogen bond between the $TFSI^-$ and the co-solvent. In short, this study establishes that the addition of a co-solvent, usually considered inert, can alter ionic speciation of the electrolyte species, and attempts to improve the transport properties through a decrease in viscosity could inadvertently impact the electrochemical properties of the system.

CHAPTER 5. INTERESTING STRUCTURE AND UNUSUAL DYNAMICS: IMPACT OF POLYMER CONCENTRATION ON PROPERTIES OF A POLYMER GEL ELECTROLYTE

5.1. Introduction

In the decades since their introduction, lithium ion batteries have emerged as the dominant energy storage technology for modern applications such as portable electronics, electric vehicles, and energy storage for power grids.[1, 2, 5, 6, 12] However, serious safety concerns remain concerning the flammable carbonate solvents used in many commercial non-aqueous lithium ion electrolytes, which has led to substantial interest in the development of safer alternatives.[258, 259] One solution to these pressing safety concerns has been the development of gel polymer electrolytes (GPEs), wherein a non-aqueous lithium ion electrolyte is suspended within a polymer matrix that stabilizes the system.[91-93] The complex composition of these electrolytes raises heretofore unanswered questions about the interactions within the system and how the electrolyte properties are impacted.

A survey of past research prompts the question of whether the polymer in these gels systems acts as an inert, stabilizing scaffold for the electrolyte or whether interactions with the polymer actually alter the physical and chemical properties of the system. Indeed, there is evidence to suggest that the identity of the polymer plays a key role in dictating its interactions with the electrolyte, such that different properties can be expected from gels electrolytes comprised of different polymers. Several studies have highlighted the different effects of three commonly-used polymers for electrolytes: polyethylene oxide (PEO), poly(methyl methacrylate) (PMMA), and polyacrylonitrile (PAN). In PAN polymer gel electrolytes, greater formation of ion pairs has been observed.[33, 34, 97] Conversely, PEO gels dissociate the lithium salt better than organic nonaqueous electrolytes, such that less ion pairs are found in a PEO-based gel.[94,

95] In contrast, no changes in speciation are observed for the polymer gels comprised of PMMA.[35, 96] The three polymers also display different lithium transport behavior. In PMMA gels, the addition of the polymer has no impact on ion dynamics, such that no interactions between the lithium and polymer are expected.[35, 37, 97, 99, 102, 103] Contrarily, in PEO gels, the lithium conductivity is shown to be coupled to the segmental motions of the polymer chain.[36, 98, 100, 101] Accordingly, PMMA and PEO fulfill opposite roles in their corresponding gels as an inert host with no impact on dynamics and an interacting medium whose chain motions directly impact the flow of ions, respectively. Interestingly, PAN occupies a role between these two extremes, wherein the polymer has clear interactions with the electrolyte, but the conductivity of the system is independent of the segmental motions of the polymer backbone.[33, 103-105] Of particular interest, it has previously been observed that the addition of PAN to a liquid lithium ion electrolyte increases the conductivity, which points to the polymer not only interacting with the electrolyte, but also playing an active role in enhancing conductivity.[33]

It remains unclear what molecular-level changes in the PAN gel lead to the enhanced conductivity. The decoupling of the diffusive behavior from the segmental motions of the polymer, observed for PMMA gels, implies the conductivity is controlled by diffusion, but this effect alone does not explain the observed increase in conductivity.[37, 103] It has been proposed that stronger dissociation of the lithium salt by the plasticizer plays a part in the larger conductivity observed in gel electrolytes.[260] However, this explanation is at odds with another study which found that interactions between the lithium and nitrile groups of polymer simultaneously enhanced the conductivity and promoted the formation of ion pairs.[33] The role of PAN in facilitating $LiClO_4$ ion pair formation is backed by multiple other studies, citing a

much weaker perturbation of the anion by the PAN nitriles compared to the plasticizer.[34, 261, 262] A separate Raman study showed that the polymer enhances the ion-solvent interactions.[97] Furthermore, the increased conductivity has been justified on the basis of a hopping mechanism, where the dissociated Li+ moves between positions along both the polymer backbone and the solvent separate from the anion.[104, 261, 262] This complicates interpretation, since several studies have shown that the presence of PAN strengthens ion pair formation in these electrolytes and that the anion appears predominantly within the vicinity of the cation.[34, 97] Another work argued that the enhanced conductivity is the result of greater mobility of the anion rather than the cation, since the cation presents a similar transference number for several different salts.[263] This matches one interpretation of the ion transport, wherein the lithium ion is confined to jumping along the polymer chain, but the anion moves outside the channel in the gel state.[262] Further conflicts surround the solvent interactions in these gels. Some research suggests strong dipolar interactions between the polymer nitriles and cyclic carbonates, leading to preferential solvation of the PAN nitriles instead of the cation.[96, 264, 265] Other research indicates Li+ interacts with both the solvent and nitrile groups of the polymer in gel electrolytes.[104, 261, 266] Accordingly, the ability of the lithium to associate with both polymer and solvent could explain the increased ion mobility, but the variety of interactions available to the lithium cation complicates interpretation, creating a murky molecular picture.

The conflicting interpretations of the association within the gels warrant further exploration of the structure and dynamics in these complex systems. In this work, a polymer gel electrolyte comprised of a lithium-ion electrolyte dispersed in a polyacrylonitrile (PAN) polymer matrix was proposed, and its properties were studied with various experimental methods. Three electrolyte samples of lithium perchlorate ($LiClO_4$) dissolved in a cyclic carbonate mixture

(EC:PC 1:1 by mass) with 0%, 5%, and 10% polyacrylonitrile by weight were studied to determine the effect of polymer content on the structure and properties of the system (Scheme 5.1). The nitrile stretch has been previously utilized to study structure in polymer electrolytes, implicating it as a useful probe for investigating structural changes around the functional group of the polymer.[34, 104, 261, 262, 267] Structure and picosecond dynamics were further explored using 2DIR spectroscopy with lithium thiocyanate (LiSCN) as a vibrational probe. The thiocyanate ion has previously been used as an infrared probe due to the strong infrared absorption and long vibrational lifetime of its nitrile mode and its small size, which enables the anion to probe confined domains without steric hindrance.[120, 133, 268, 269] In addition to infrared characterization, viscosity testing and differential scanning calorimetry were performed to supplement the results. DSC is a powerful technique for studying the structure of polymers, and the use of modulated DSC bears the distinct advantage of distinguishing between the kinetic and thermal transitions contributing to the total heat flow.[33, 265, 270-273] A picture of the differences in molecular structure with increasing polymer concentration is proposed.

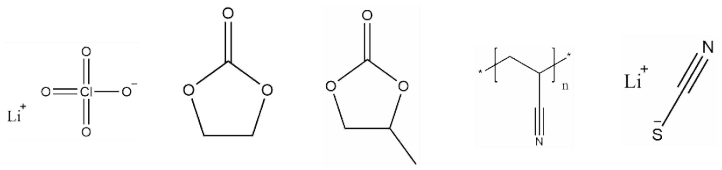

Scheme 5.1. Structures of all substances used. From left to right: lithium perchlorate ($LiClO_4$), ethylene carbonate (EC), propylene carbonate (PC), polyacrylonitrile (PAN), and lithium thiocyanate (LiSCN).

5.2. Methods

5.2.1. Sample preparation

To remove any dust or contaminants, polyacrylonitrile (PAN, Scientific Polymer Products, MW ~150,000) was dissolved in dimethylformamide, then the resulting solution was filtered through a syringe filter with a 0.2 μm PTFE membrane into 18MΩ water. The polymer

was then dried at 39C in a vacuum oven for 24 hours. Lithium perchlorate ($LiClO_4$, Aldrich) was dried at 140C in a vacuum oven for 24 hours prior to use. Propylene carbonate (PC, Acros Organics, 99.5%) was dried under activated 4Å molecular sieves prior to use. Ethylene carbonate (EC, Acros Organics, 99+%) was used as received without further purification. All reagents and prepared samples were stored in a N_2-filled glovebox. Sample cells utilized in FTIR and 2DIR spectroscopy comprised a small amount of sample compressed between two CaF_2 window with no spacer hosted in an O-ring sealed sample cell. All sample cells were prepared in a glovebox purged with nitrogen. The three concentrations studied via 2DIR spectroscopy contained 0% PAN, 5% PAN, and 10% PAN by mass; the ratio of lithium salt to coordinating units (solvent + polymer) was kept constant across samples.

5.2.2. FTIR spectroscopy.

FTIR spectra were recorded on a Bruker Tensor 27 spectrometer outfitted with a mercury cadmium telluride (MCT) detector cooled via liquid nitrogen. The same 0.5 cm^{-1} resolution was used for each sample, and all measurements were averaged from 40 scans. All standard measurements were taken at room temperature. For temperature-dependent FTIR measurements, the sample was held between two CaF_2 windows in a Harrick temperature-controlled sample cell, which was attached to a Pharmacia Biotech circulating bath.

5.2.3. Two-dimensional (2D) IR spectroscopy.

The setup used for recording 2DIR spectroscopy measurements has been described previously in the literature, so only a short summary is provided here.[38, 142] A Ti:sapphire amplifier (comprised of a Spectra Physics Mai Tai oscillator and Spitfire Ace regenerative amplifier) with a 5 kHz repetition rate was used in conjunction with an optical parametric amplifier (OPA-800C) and difference frequency generation crystal to give broadband infrared

pulses. Three replica IR pulses were focused on the sample in the boxcars geometry, generating the photon echo signal in the phase matching direction $-\mathbf{k}_1 + \mathbf{k}_2 + \mathbf{k}_3$, which was subsequently overlapped with a fourth local oscillator pulse for heterodyne detection.[38] After dispersion on a Triax monochromator, the heterodyned signal was measured by a 64 element MCT array detector (Infrared Systems Development). The signal was measured with respect to three time intervals: the coherence time τ (the separation between pulses 1 and 2), the waiting time T_w (the separation between pulse 2 and 3), and the coherence time t (the separation between pulse 3 and the signal). Each interval was set via computer-controlled translation stages. For each waiting time, 2DIR spectra were collected by scanning τ from -4 ps to +4 ps with a 5 fs step; both the rephrasing and nonrephasing data were collected by switching the time ordering.[38] The local oscillator always preceded the detected signal by ~0.7 ps. Spectra were collected for waiting times ranging from 0 to 100 ps in an exponential timestep (22 total steps). The time domain signal, collected as a function of (τ, T_w, λ_t) via a monochromator-array detection, was transformed into the 2DIR spectra (ω_τ, T, ω_t) via Fourier transforms, which has been thoroughly detailed elsewhere.[148]

5.2.4. Viscosity measurements.

Viscosity measurements were recorded on a Brookfield DV-II+ Pro viscometer. The low viscosity samples (0% PAN and 5% PAN) were measured with the SPE-40 spindle, while the higher viscosity sample (10% PAN) necessitated the use of the SPE-52 spindle.

5.2.5. Differential scanning calorimetry.

Differential scanning calorimetry (DSC) measurements were performed on a Discovery DSC 250 (TA Instruments) using an empty pan as reference. The samples (~10 mg) were hermitically sealed in alodined aluminum pans using a sample encapsulation press, and all

samples were prepared inside a nitrogen-purged glovebox to minimize exposure to moisture. The DSC samples were cooled to -40 °C and allowed to equilibrate for 5 minutes before heating at a rate of 3 °C per minute until 140 °C. The system was purged with nitrogen at a rate of 50 mL/min.

5.3. Results

5.3.1. FTIR spectroscopy

The FTIR spectra for the polymer nitrile region (2210-2290 cm-1) for three polymer gel samples with varying concentration of lithium salt are shown in Figure 5.1. For all samples, the spectra show a low frequency band at 2244 cm-1, which is here used for normalization. With the addition of lithium salt, a higher frequency band is observed at 2270 cm-1; this band grows with lithium salt concentration and is not present at all in the electrolyte sample without lithium salt (0:30:26:2.5). These two bands are separated by 26 cm-1, and neither shows an appreciable shift in frequency with salt concentration. The intensity of the bands varies significantly with lithium salt concentration. In the 7:30:26:2.5 sample, the intensity of the high frequency band is lower than the low frequency band. However, for the 14:30:26:2.5 sample, the intensities are inverted with a greater intensity for the high frequency band.

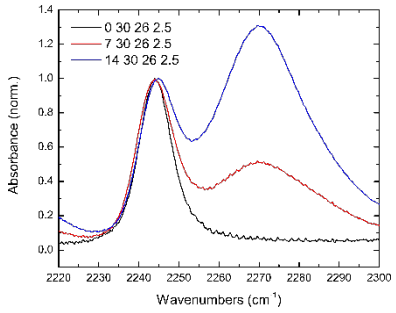

Figure 5.1. FTIR spectra of the nitrile stretch region for LiClO4:EC:PC:PAN samples as a function of lithium salt concentration.

Concentration-dependent FTIR of the polymer nitrile region was also taken with respect to the polymer concentration to observe the effect of varying the polymer content. These samples were characterized by percent mass of polymer from 2.5% through 15% PAN with the ratio of lithium salt to coordinating unit (polymer + solvents) held constant (the molar concentration is 7 $LiClO_4$: 56-X EC+PC : X PAN, where the solvent is inversely scaled with PAN concentration). The resulting spectra are given in Figure 5.2. Each spectrum showed two infrared bands: an intense, low frequency band at 2244 cm-1 and a higher frequency band with less intensity at 2269 cm-1. The data was normalized with respect to the low frequency band, which appears to broaden slightly with increasing polymer concentration. Interestingly, the high frequency band changes with polymer concentration but not monotonically. The high frequency band grows with polymer concentration until a maximum for 5% PAN, then the intensity decreases through 15% PAN.

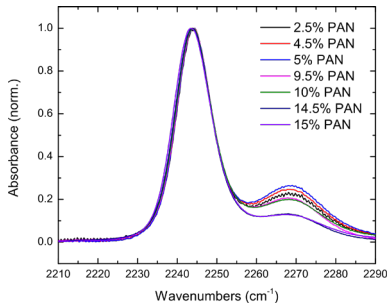

Figure 5.2. FTIR spectra of the nitrile stretch region for LiClO4:EC:PC:PAN samples as a function of PAN concentration.

Temperature-dependent FTIR spectra were taken for the 5% and 10% polymer samples to compare the effect of changing temperature at different concentrations. This data is compiled in Figure 5.3. Both samples present the same peaks observed in the concentration-dependent FTIR spectra: an intense low frequency peak at 2244 cm-1 and a weaker, high frequency peak at 2270 cm-1. Comparing the two spectra, both spectra are redshifted with increasing temperature. The

high frequency band is more intense in the 5% sample at all temperatures, and the high frequency band also exhibits greater change with temperature in the 5% sample than observed for the 10% sample. The intensity of the high frequency band grows with temperature in the 5% sample but loses intensity in the 10% sample.

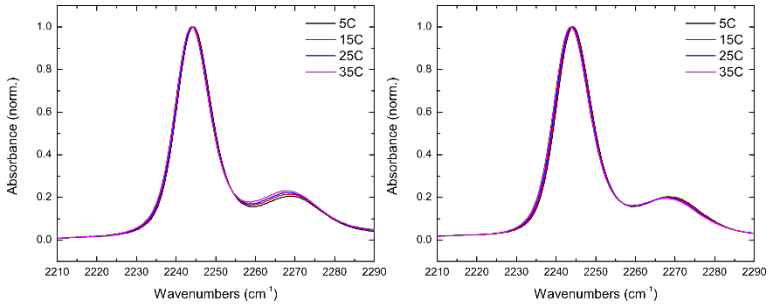

Figure 5.3. FTIR spectra for the nitrile stretch region for LiClO4:EC:PC:PAN samples as a function of temperature. Left panel depicts the 5% PAN sample, while right panel depicts the 10% PAN sample.

5.3.2. 2DIR spectroscopy

Two-dimensional infrared (2DIR) spectroscopy was also used to study the system at three concentrations: 0% PAN (pure electrolyte), 5% PAN, and 10% PAN by mass. Structure and dynamics were probed as a function of waiting time T_w using a small amount of lithium thiocyanate (LiSCN). Figure 5.4 shows the 2DIR spectra across T_w for the different polymer concentrations. The red positive peaks located along the diagonal at [$\omega_\tau = 2076$ cm^{-1} , $\omega_t = 2072$ cm^{-1}] arise from the transitions between the ground state ($\nu = 0$) and the first excited state ($\nu = 1$), while the negative blue peaks positioned at [$\omega_\tau = 2076$ cm^{-1} , $\omega_t = 2046$ cm^{-1}] represent the transitions between the first excited state ($\nu = 1$) and second excited state ($\nu = 2$).[38] The blue peaks are redshifted by 26 cm^{-1} for each sample due to the anharmonicity of the nitrile stretch in thiocyanate, as previously observed.[198] Both peaks for the 10% PAN sample are slightly blueshifted to [$\omega_\tau = 2078$ cm^{-1} , $\omega_t = 2076$ cm^{-1}] and [$\omega_\tau = 2077$ cm^{-1} , $\omega_t = 2051$ cm^{-1}] compared to the lower concentration samples. For all three concentrations, the frequencies are initially

elongated along the diagonal (black line where $\omega_\tau = \omega_t$), and the peaks broaden with increasing waiting time, losing the initial tilt along the diagonal. As molecules move in solution, there is a loss of correlation between the initial (pump, ω_τ) and final (probe, ω_t) frequencies; this spectral diffusion alters the 2DIR spectra, resulting in the broadening observed in Figure 5.4 with T_w.[38] The pure electrolyte sample appears to decorrelate slightly faster than the other samples, adopting a more upright peak shape at 70 ps than either sample with polymer possesses. Otherwise, the data is similar for the three concentrations through T_w = 70 ps.

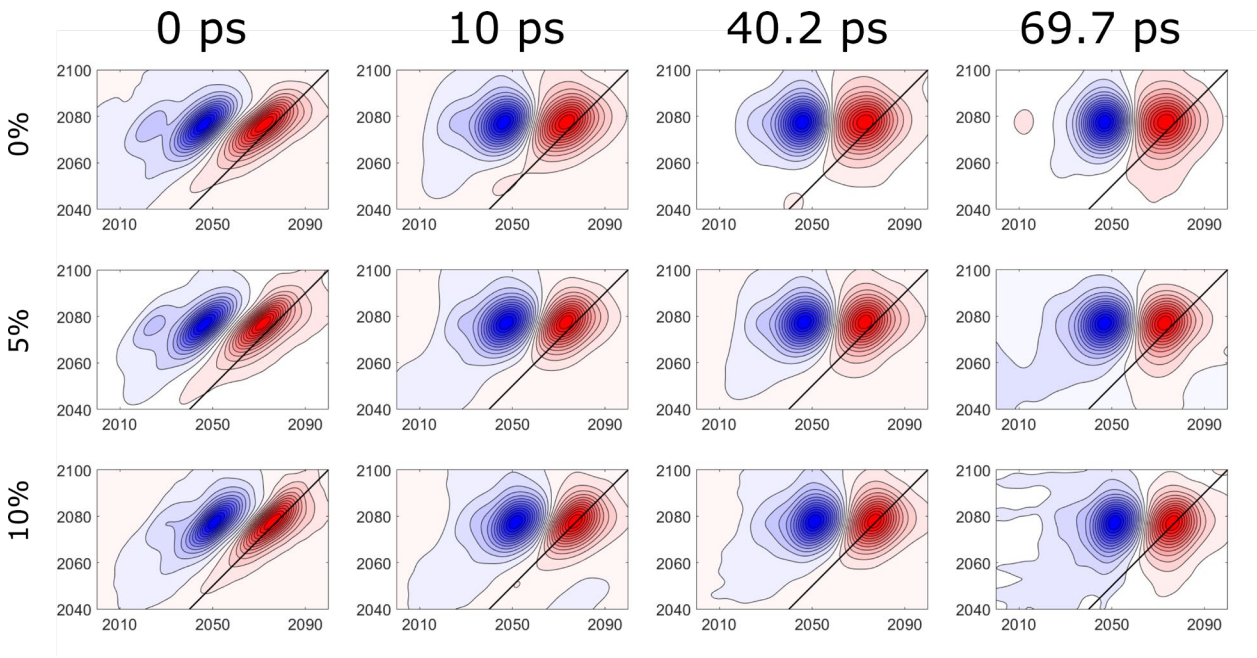

Figure 5.4. 2DIR spectra for 0% PAN (top row), 5% PAN (middle row), and 10% PAN (bottom row) as a function of waiting time, T_w. The plotted spectra (from left to right) were captured at T_w = 0ps, 10 ps, 40.2 ps, and 69.7 ps.

5.4. Discussion

5.4.1. Structure and dynamics

The FTIR spectra in Figure 5.1 show the nitrile stretch region of the polymer as a function of lithium salt concentration. Two bands are detected in the polymer nitrile region, one of which grows with increasing lithium salt concentration; these bands are assigned to the free nitrile stretch (low frequency, 2244 cm-1) and the nitrile stretch coordinated to the lithium cation

(high frequency, 2269 cm-1) in accordance with the assignments made in previous studies.[34, 104, 266, 274, 275] The concentration of lithium salt controls the equilibrium between free and coordinated nitrile, since the intensity of the coordinated band changes with concentration of lithium salt.[261, 262, 266] Conversely, the FTIR spectra collected by varying the polymer concentration (Figure 5.2) show that a majority of the polymer nitrile groups exist as free species regardless of concentration; there is no polymer concentration that favors the formation of more coordinated nitriles than free, in contrast to the trend from lithium salt concentration. Previous literature has noted the concentration-dependent Raman and FTIR data of similar gels, but the concentrations used herein are unreported.[34, 96, 261, 266] Moreover, the coordination of nitrile groups is not monotonically linked to polymer concentration. The high frequency band, denoting the coordination of the polymer nitrile to the cation, is maximized for the 5% polymer sample, and the intensity decreases for all concentrations greater or lower than 5% polymer. Thus, the addition of more polymer past 5% mass does not result in further coordination to the lithium cation but instead in the presence of more free nitrile bands. Increasing the polymer concentration does not continuously enhance the coordination as seen when increasing the lithium salt concentration. Non-monotonic coordination has been reported previously for a $LiClO_4$:PC:PAN electrolyte; however, the polymer concentration was much higher than the present study.[261] This unusual trend cannot be explained by concentration alone and likely denotes additional structural differences. The temperature-dependent FTIR spectra underscore this result, showing opposite trends in the growth of the coordinated band with temperature (Figure 5.3). At 5% polymer concentration, the coordinated nitrile band grows with temperature; at 10% polymer concentration, the coordinated band shrinks with temperature. This interesting result implies a structural change with temperature in the 5% sample to enhance lithium-polymer

interactions, which is not seen at higher polymer concentrations. To probe these underlying differences, differential scanning calorimetry (DSC) measurements were taken for the 5% and 10% polymer samples, the results of which are listed in Figure 5.5. For the 5% polymer gel, the DSC results show two changes in the heat flow in the range of 50-100°C, separated by 10°C, both of which are derived from the non-reversing heat flow, indicating kinetic processes underlying both transitions. The DSC results for the 10% polymer gel reveal two transitions instead separated by 40°C. When the heat flow is decomposed into reversing and non-reversing components, one feature is due to the non-reversing heat flow, while the other represents the reversing heat flow. In contrast to the 5% polymer sample, the 10% gel manifests a large change in the reversing heat flow, associated with thermal changes. The extra thermal peak implies the melting of a structure only present in the 10% PAN sample, while the extra kinetic peak in the 5% PAN sample suggests greater mobility of the polymer nitriles. These key differences bolster the interpretation of different structures with polymer concentration.

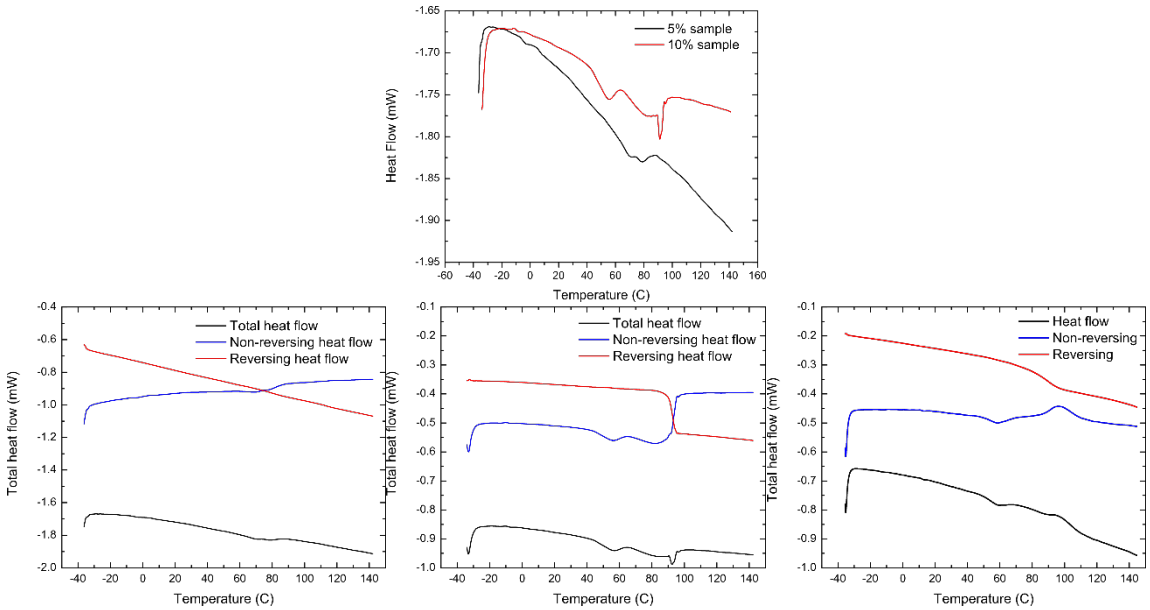

Figure 5.5. Differential scanning calorimetry results. Comparison of DSC for 5% and 10% samples, adjusted to the same scale (top). Modulated DSC of the 5% sample (bottom left). Modulated DSC of the 10% sample (bottom middle). Modulated DSC of PAN without electrolyte (bottom right).

The linear FTIR spectrum of the thiocyanate stretch (Figure 5.6) looks similar at each concentration probed. Analysis of the spectrum shows no change in the central vibrational frequency with increasing polymer concentration, indicating that the average environment sensed by the thiocyanate is the same regardless of sample. Voigt modeling reveals a slight broadening in the absorbance for the 10% PAN concentration (see Figure 5.6). The width of the IR spectrum is related to the distribution of environments sampled, so the thiocyanate appears to sense environments at the 10% PAN concentration that were not present at lower concentrations.[136, 276, 277] However, previous research shows that the nitrile stretch frequency is sensitive to structural changes in the local environment, so any structural changes sensed by the probe should be reflected in both the broadening of the width and a shift in the central frequency.[205, 278-279] The underlying cause of this broadening (dynamics vs structural changes) cannot be distinguished by FTIR spectroscopy, which necessitates the use of ultrafast 2DIR spectroscopy.

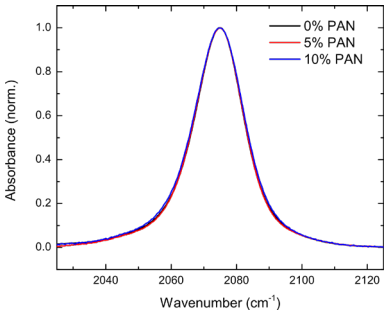

Sample	FWHM (cm^{-1})
0% PAN	19.7
5% PAN	19.9
10% PAN	20.6

Figure 5.6. FTIR spectra (left) of the nitrile region of the thiocyanate ion as a function of polymer concentration. The full width at half maxima (FWHM) from the Voigt fitting of each sample is also listed in the table (right).

The time evolution of the 2DIR spectra (Figure 5.4), characterized by the frequency-frequency correlation function (FFCF), shows the loss of correlation between the initial (ω_τ) and final (ω_t) frequencies with T_w.[38, 136, 277, 280] This decorrelation reflects changes in the dynamics or the environment, i.e., spectral diffusion.[38] The loss of correlation is analyzed by

the nodal line slope method (Figure 5.7) and provides the characteristic timescales of the motions sensed by the SCN- probe.[281] The fitted FFCF in Table 5.1 shows that the SCN- probe senses two distinct timescales: one motion occurs within 3 ps (t_1), and the other motion takes 30 ps for the pure electrolyte and 60 ps for both polymer samples, an order of magnitude slower (t_2). Previous studies using SCN- to probe ionic liquids and glyme-based electrolytes have attributed similar motions to two different processes: the short rattling-in-cage motions and the longer reorganization of the complex.[123, 133] Similarly, the dynamics in these systems is ascribed to two processes: a fast, restricted motion of SCN- near the lithium cation and a slower total reorganization of the system. The restricted motion has the same characteristic time regardless of sample, while the reorganization motion is faster in the pure electrolyte (0% PAN) than either polymer sample, which matches the observation of slightly faster decorrelation in the 2DIR spectra of the 0% sample (Figure 5.4). Surprisingly, doubling the polymer concentration does not impact the reorganization dynamics.

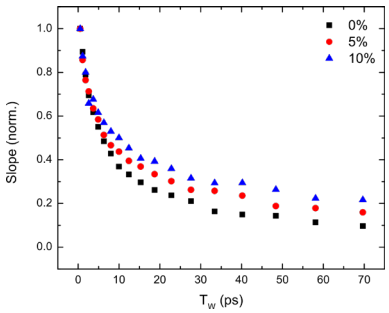

Figure 5.7. Decay of the nodal line slope for the 0% PAN (black), 5% PAN (red), and 10% PAN (blue) samples as a function of waiting time, T_w.

To explain the significance of the dynamics results, Figure 5.8 shows the physical appearance of all three samples: pure electrolyte, 5% polymer sample, and 10% polymer sample. At room temperature, the pure electrolyte is a flowing liquid, the 5% sample is a viscous liquid, and the 10% sample is a gel. The dynamics therefore implies similar motions for the liquid phase 5% sample and the gel 10% sample. It is also worth noting that the 10% sample has less coordinated

nitrile groups than the 5% sample (evidenced by Figure 5.2) with little impact on the dynamics. The measured viscosity, showcased in Table 5.3, further complicates the interpretation of these systems. The viscosity of the 5% polymer sample is two orders of magnitude greater than the pure electrolyte, yet the dynamics do not reflect a substantial slowdown in the dynamics. In addition, the viscosity of the 10% sample is roughly two orders of magnitude greater than the already high-viscosity 5% sample, and their dynamics are nearly identical. Increasing the polymer concentration leads to completely different morphologies and a drastic increase in viscosity, but the polymer concentration has little impact on the system dynamics.

Table 5.1. Characteristic times t_1 (fast motion) and t_2 (slow motion) calculated from the NLS analysis of the experimental 2DIR spectra.

Sample	t_1 (ps)	t_2 (ps)
0% PAN	3.1 ± 0.3	32 ± 3
5% PAN	3.4 ± 0.4	57 ± 6
10% PAN	3.1 ± 0.6	67 ± 9

Table 5.2. Full fitting parameters for the nodal line slope analysis of the experimental 2DIR spectra (Figure 5.4). t_1 and t_2 are the characteristic times of the two distinct motions, and A_1 and A_2 are their amplitudes, respectively. The decay of the frequency-frequency correlation function with waiting time T_w was fit with an exponential of the form:

$$y = A_1 e^{\frac{-Tw}{t1}} + A_2 e^{\frac{-Tw}{t2}}.$$

Sample	t_1 (ps)	A_1	t_2 (ps)	A_2
0%	3.1 ± 0.3	0.6 ± 0.1	32 ± 3	0.5 ± 0.1
5%	3.4 ± 0.4	0.6 ± 0.1	57 ± 6	0.5 ± 0.1
10%	3.1 ± 0.6	0.5 ± 0.1	67 ± 9	0.5 ± 0.1

Table 5.3. The viscosity of each sample collected at 20 °C.

Sample	Viscosity (cP)
0% PAN	11.9 cP
5% PAN	2965 cP
10% PAN	>93,000 cP

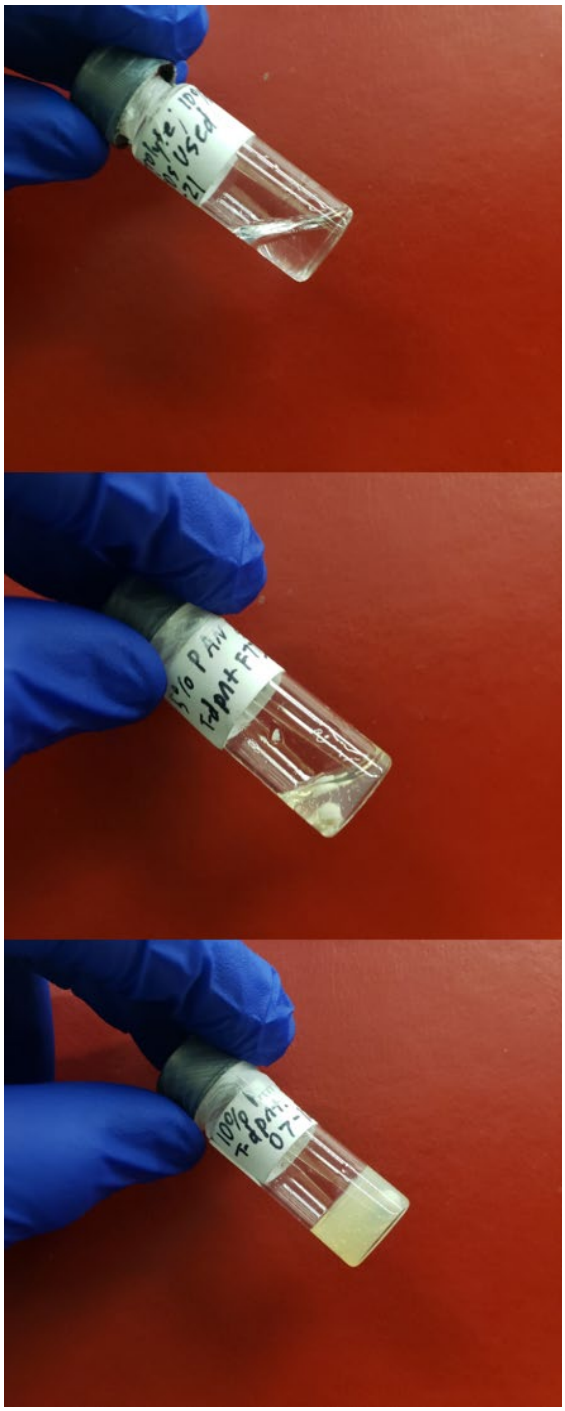

Figure 5.8. Images of all three samples: 0% PAN (top), 5% PAN (middle), 10% PAN (bottom).

A connection has been proposed between the time scale of the structural reorganization and the viscosity in imidazolium ionic liquids, which is rationalized by a simple Stokes-Einstein diffusion model.[133, 282] If the viscosity ratio matches the ratio of vibrational lifetimes, the

reorganization of the complex is the initiating event which activates diffusion and hence controls the viscosity. For the PAN samples, the dynamics ratios (1.8 for $\frac{5\%}{0\%}$, 1.2 for $\frac{10\%}{5\%}$) differ significantly from the viscosity ratios (250 for $\frac{5\%}{0\%}$, 31 for $\frac{10\%}{5\%}$), suggesting that the ion motions are decoupled from the bulk viscosity.[37, 99, 102, 283] To explain this, the polymer is proposed to form channels with the polymer sidechains oriented along the perimeter of the cavity, while the solvated Li+ travels through the center of the channel. Previous modeling of PAN showed intramolecular repulsion between parallel adjacent nitriles forcing the adoption of an irregular helix to minimize nitrile-nitrile interactions.[284, 285] Additionally, previous studies showed the transition from a hexagonal to orthorhombic packing of PAN chains with the addition of PC, which results in cavities large enough for the intercalation of solvent molecules into the polymer matrix.[265, 271] The mobility of Li+ through these helical tunnels is further supported by previous studies, so the Li+ diffusion should depend on the solvent diffusion rather than the mobility of the polymer.[286-288] The diffusion is thereby decoupled from the bulk viscosity as expected from the discrepancy between the dynamics and viscosity ratios.[37, 102] Previous studies in PMMA electrolytes showed the system behaves like a liquid electrolyte held in a polymer matrix at low PMMA concentration (<30% wt. PMMA), while at high polymer concentration (≥30 wt. PMMA), interactions between polymer and electrolyte increase the viscosity, thereby decreasing the conductivity.[99, 283] Neither picture matches the reported behavior for PAN gel electrolytes, where the addition of PAN to a liquid electrolyte enhances the conductivity; this suggests that interactions between the polymer nitriles and Li+ play an important role in strengthening the conductivity.[33] One study proposed the formation of a complex between Li+ and PAN nitriles above a concentration ratio (0.7 PAN:$LiClO_4$ by mass), where ion mobility depends on both solvent diffusion and Li+ hopping along polymer chains,

while at lower PAN concentration, ion mobility is related only to diffusion.[289] However, the proportion of cations coordinated to the nitriles is small (5%, see Figure 5.9), which contradicts the proposal of a strong transport contribution from Li+ hopping.[290] Instead, the proposed mobility involves a partially solvated lithium interacting with the polymer nitriles while diffusing thorough the cavity. The motion of the cation is still dependent on solvent diffusion, but this favorable interaction with the polymer sidechains could explain the enhanced conductivity through solvating the lithium to facilitate faster diffusion. Previous work has posited the cation is solvated by the polymer nitrile and multiple solvent molecules; in addition, a computational study showed a strong preference for lithium binding to EC over PMMA but similar preference for EC and PAN.[33, 34, 96, 289]

To summarize the results thus far presented: first, the interactions between the lithium cation and polymer are not monotically enhanced by higher polymer concentration but are rather maximized for the 5% polymer sample. Second, the different concentrations present opposite trends in Li-polymer interaction with temperature, implying different structures in the polymer samples, which is supported by DSC results. Third, the SCN- senses two dynamics processes: a fast caged motion in the vicinity of the cation and a slower reorganization of the complex. Fourth, increasing the polymer concentration has drastic consequences on the sample topology and viscosity but little impact on the dynamics at the molecular level, which suggests the motions are decoupled from the bulk viscosity. To clarify the complex interactions leading to these results, a molecular picture is proposed in the following section.

5.4.2 Molecular picture

In developing a description of the interactions at the molecular level, it is conducive to re-examine all characterization data presented thus far in tandem. Comparing Figure 5.1 and Figure

5.2, the ratio of free nitrile to coordinated nitrile exhibits stronger changes as a function of lithium concentration rather than polymer content. At the maximum concentration of coordinated nitriles (5% PAN sample) in Figure 5.2, only 12% of the nitriles are coordinated to lithium (see Figure 5.9). Comparison with Figure 5.3 indicates that this speciation changes only marginally with temperature; most of the polymer nitriles remain uncoordinated to lithium. Since the concentration of lithium salt is constant across polymer samples, an apparent contradiction presents itself: as nitriles become increasingly available with higher polymer concentration, how can the sample have less interactions between the lithium cation and polymer nitrile? Furthermore, as discussed above, the 5% PAN and 10% PAN samples display opposite coordination behavior with temperature (Figure 5.3). This paints a picture of two distinctly different systems; the 5% sample has more lithium-nitrile interactions and gains even more with increasing temperature, while the 10% sample has less lithium-nitrile interactions and loses even more as a function of temperature. The broadening of the FTIR spectrum for LiSCN in the 10% sample also evidenced different structures, since the dynamics were identical for the two polymer samples. Combined, these results indicate that some of the lithium cations are interacting with either the solvent or the perchlorate anion in place of the polymer nitrile and that the favorability of these interactions is dependent on both polymer concentration and temperature. It has been shown previously that that the nitrile-solvent interactions in polyacrylonitrile gel systems are favored over interactions between the nitrile and lithium cation, which informs the interpretation of the molecular species.[34, 96, 264, 265] Interactions between the polymer nitriles and solvent molecules are rationalized via the amount of free nitrile present at all concentrations of polymer, as well as previously observed dipolar ordering of carbonate solvents with polar functional groups along the polymer backbone.[34, 264, 265] The dynamics

of these two systems is identical, implying that the cation diffuses the same way in both samples regardless of polymer concentration and coordination; however, the interactions described thus far also do not account for the large discrepancy in viscosity.

To explain the increase in viscosity, interactions between nitriles of adjacent polymer chains are proposed at 10% PAN concentration; this should lead to a rigid polymer framework without changing the diffusion. The 10% sample has twice the polymer content of the 5% sample, so interactions between nitriles should be more favorable at higher concentration. Moreover, interactions between nitriles solves the apparent mystery of less Li-polymer interactions with higher polymer content. This molecular picture is supported by the DSC results, which showed different underlying processes contributing to the total heat flow for the 5% PAN and 10% PAN samples. A large thermal process occurs in the 10% sample, which matches the thermogram for pure PAN (see Figure 5.5) indicating the breaking of nitrile-nitrile interactions. In the 5% sample, a kinetic change is present at higher temperature; greater free rotation of the polymer sidechains would explain well the ability of Li+ to form more interactions with the nitriles with temperature. This kinetic peak is not observed in the 10% sample due to the more rigid, ordered structure imposed through nitrile-nitrile interactions. The differences in molecular structure across polymer concentration are illustrated in Scheme 5.2. Ions diffuse freely in the 0% polymer sample. The presence of polymer chains only slightly hinders diffusion in the 5% sample. For the 10% PAN sample, the high polymer concentration allows the formation of rationale behind the similar dynamics across samples in spite of large changes in viscosity.

Previous work suggests that a lithium coordinated to a nitrile will also be solvated by multiple EC/PC, while a single solvent molecule is sufficient to solvate an uncoordinated

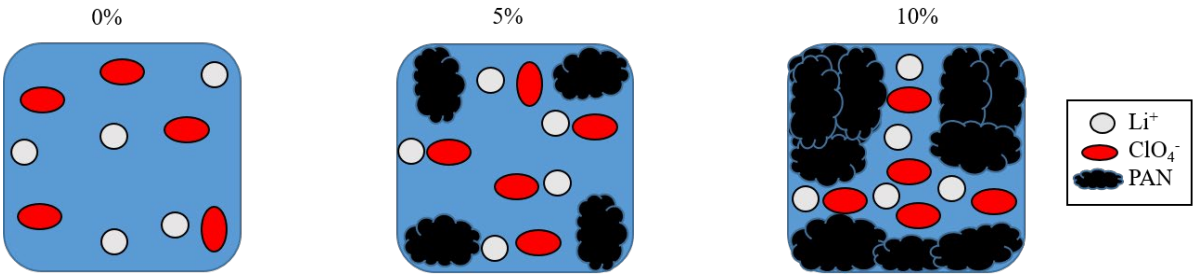

Scheme 5.2. Cartoon depiction of molecular structure with increasing polymer concentration. The PAN concentration increases from 0% (left) to 5% (center) to 10% (right) by mass.

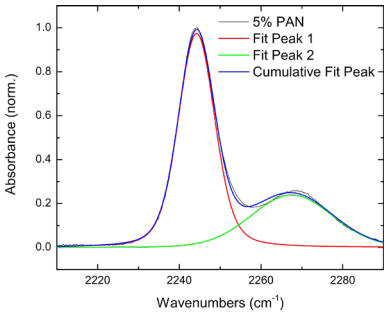

Parameter	Low frequency peak	High frequency peak
central frequency	2244.3 ± 0.2	2267.9 ± 0.5
area	12.3 ± 0.2	6.2 ± 0.3
Gaussian width	9.0 ± 0.2	20.6 ± 1
Lorentzian width	3.0 ± 0.2	3.5 ± 2
FWHM	12.2	26.2

Figure 5.9. FTIR spectra (left) of the polymer nitrile stretch region for the 5% PAN sample, fit with 2 Voigt profiles. The fitting parameters are given in the table (right). The area of each peak gives a qualitative assessment of the speciation in solution; however, this disregards the contribution of the transition dipole moment, μ_{ij}, to the lineshape. To more accurately describe the species, the ratio of the transition dipole moments was taken from the work of Chen [320]:

$$\frac{c_a\mu_a^2}{c_b\mu_b^2} = 1.75 \qquad \frac{c_a\mu_a^4}{c_b\mu_b^4} = 0.615 \qquad \frac{\frac{c_a\mu_a^2}{c_b\mu_b^2}}{\frac{c_a\mu_a^4}{c_b\mu_b^4}} = \frac{\mu_b^2}{\mu_a^2} = \frac{1.75}{0.615} = 2.85$$

The Voigt fittings attribute 33% of the total area to the coordinated peak. The molar concentration of the sample is 7:30:26:6 $LiClO_4$:EC:PC:PAN. The area of the coordinated peak is divided by the ratio of transition dipole moments to give the correct amount of coordinated nitriles:

$$\frac{33\%}{2.85} = 11.6\%$$

The amount of coordinated nitriles can then be used to calculate the amount of lithium cations coordinated to the nitriles, since the concentrations of both are known:

$$\frac{x}{c_1} = \frac{11.6\%}{100\%} \rightarrow \frac{x}{6} = \frac{11.6\%}{100\%} \rightarrow x = 0.696 \rightarrow x \cdot c_2 = x \cdot 7 = 4.9 \approx 5\%$$

Only 5% of the lithium cations in the 5% sample are coordinated to the polymer nitriles; it is therefore unlikely that the Li+ hopping mechanism contributes significantly to the ion transport. It is noted that the 5% sample has the most coordination of all concentrations. Additionally, this calculation assumes each coordinated Li+ to interact with only one nitrile; in reality, the cation may interact with multiple nitriles, such that the percentage of interacting cations is even smaller.

nitrile.[33, 265, 271] The 5% sample, which has more lithium-nitrile interactions, should have less available free solvent than the 10% sample. Previous research has found cyclic carbonates in two different environments within gel electrolytes: as coordinated solvent molecules, which interact with the polymer and cation, and as a confined domain of solvent molecules trapped within the interior of the polymer chain, which experiences no interactions with the lithium salt nor polymer nitriles.[33] Interestingly, the amount of solvent trapped in the interior cavity changes with concentration: as the ratio of PAN:lithium salt increases, less solvent molecules are trapped in the interior. This matches nicely the description of the 10% PAN sample, where less confined solvent molecules interact with the polymer nitriles and lithium cations, minimizing direct interactions between the lithium and polymer from both sides. The 5% sample, with more solvent molecules confined to the interior of the polymer channels, sees more lithium-nitrile interactions, which is reflected in the linear IR results (Figure 5.2). Additionally, several studies indicate that among the interactions described, interactions between the polymer nitrile and carbonate solvents are most favored, as opposed to lithium-polymer or lithium-solvent interactions.[96, 264, 265] This reflects an important consequence of the solvent confinement on the samples at different concentrations. With increasing temperature, both the 5% and 10% PAN samples should dissociate ion pairs into free ions. The 10% PAN sample has more free solvent, which solvates the dissociated lithium, mitigating lithium-nitrile interactions. In the 5% PAN sample, more solvent is confined to the interior of the sample, such that excess solvent is not present. Thus, the lack of nitrile-solvent interactions enables the newly-freed lithium cations to interact with the polymer instead. The enhanced lithium-nitrile interactions depend not on polymer concentration but on solvent confinement, explaining the unusual non-monotonic behavior of the FTIR spectra with polymer content (Figure 5.2).

5.5. Summary

Two polymer electrolytes and an organic lithium ion electrolyte were characterized via experimental methods, and a molecular description of the interactions was proposed. FTIR spectroscopy revealed non-monotonic coordination between the lithium and polymer with polymer concentration, and opposite coordination trends were observed with temperature. The viscosities of these samples differed by orders of magnitude, and the state changed drastically from a flowing liquid electrolyte (0% PAN) to a viscous liquid (5% PAN) to a solid gel (10% PAN); interestingly, the dynamics of these three systems were not significantly different. These cumulative findings were rationalized via a molecular picture wherein the lithium cation interacts with both the solvent and the polymer nitriles. The solvent exists in two domains: as an interacting species with both the nitriles and cations and as a confined species which only interacts with other solvent molecules. Ion transport, coupled to the solvent diffusion, is proposed to occur through channels formed by parallel polymer chains. The ion motions are independent of the polymer motions, which rationalizes the similar dynamics in spite of the different viscosities. The lithium polymer interactions differ across concentration due to both differences in solvent confinement as well as nitrile-nitrile interactions within the 10% PAN sample. DSC results further supported different interactions at the molecular level with increasing polymer concentration.

CHAPTER 6. CONCLUSIONS

The impact of different molecular interactions on the macroscopic properties was explored across three different lithium ion electrolytes with unexpected results. The molecular speciation changed dramatically as a function of solvent composition. The ratio of linear to cyclic carbonates predicted an exponential preference for the formation of contact ion pairs, such that the species completely inverted from 74% free anion to 95% contact ion pair. A highly fluorinated co-solvent was added to two different lithium ion electrolytes, which displayed opposite trends from spectroscopic data and electrochemical properties with co-solvent concentration; critically, the only difference between the electrolytes was the choice of anion. The anion identity proved crucial in directing the speciation; one anion selectively formed hydrogen bonds with the co-solvent, which impacted its association to the lithium cation. This anion-dependent interaction dictates the species in solution, resulting in completely different electrolyte properties. The impact of polymer concentration on electrolyte properties was further scrutinized. The viscosity of the samples increased by several orders of magnitude with polymer concentration as expected; however, the dynamics derived from 2DIR spectroscopy interestingly show similar dynamics across all concentrations. This surprising result implies that the ion flow is identical in a liquid electrolyte and a gel, in spite of their different viscosities. The high concentration gel sample is proposed to form channels that facilitate ion flow, explaining the unusual dynamics. The study of these three electrolytes highlights the importance of characterizing the interactions of each electrolyte component and the far-reaching consequences of individual interactions on the macroscopic properties of the electrolyte.

APPENDIX A. COPYRIGHT INFORMATION FOR CHAPTER 3

Effect of Solvation Shell Structure and Composition on Ion Pair Formation: The Case Study of LiTDI in Organic Carbonates

Rushing, J.C., Leonik, F.M., and Kuroda, D.G., *The Journal of Physical Chemistry C* 2019, 123 41, 25102-25112.

DOI: 10.1021/acs.jpcc.9b07469

https://pubs.acs.org/doi/abs/10.1021/acs.jpcc.9b07469

Requests for further permissions should be directed to the American Chemical Society.

The following is proof of copyright permissions:

1/31/22, 12:54 PM Rightslink® by Copyright Clearance Center

CCC RightsLink®

Home | Help | Live Chat | Sign in | Create Account

ACS Publications
Most Trusted. Most Cited. Most Read.

Effect of Solvation Shell Structure and Composition on Ion Pair Formation: The Case Study of LiTDI in Organic Carbonates

Author: Jeramie C. Rushing, Fedra M. Leonik, Daniel G. Kuroda
Publication: The Journal of Physical Chemistry C
Publisher: American Chemical Society
Date: Oct 1, 2019

Copyright © 2019, American Chemical Society

PERMISSION/LICENSE IS GRANTED FOR YOUR ORDER AT NO CHARGE

This type of permission/license, instead of the standard Terms and Conditions, is sent to you because no fee is being charged for your order. Please note the following:

- Permission is granted for your request in both print and electronic formats, and translations.
- If figures and/or tables were requested, they may be adapted or used in part.
- Please print this page for your records and send a copy of it to your publisher/graduate school.
- Appropriate credit for the requested material should be given as follows: "Reprinted (adapted) with permission from {COMPLETE REFERENCE CITATION}. Copyright {YEAR} American Chemical Society." Insert appropriate information in place of the capitalized words.
- One-time permission is granted only for the use specified in your RightsLink request. No additional uses are granted (such as derivative works or other editions). For any uses, please submit a new request.

If credit is given to another source for the material you requested from RightsLink, permission must be obtained from that source.

BACK CLOSE WINDOW

APPENDIX B. COPYRIGHT INFORMATION FOR CHAPTER 4

Tale of a "Non-interacting" Additive in a Lithium-Ion Electrolyte: Effect on Ionic Speciation and Electrochemical Properties

Rushing, J.C., Stern, C.M., Elgrishi, N., and Kuroda, D.G., *The Journal of Physical Chemistry C* 2022, 126 (4), 2141-2150.

DOI: 10.1021/acs.jpcc.1c09193

https://pubs.acs.org/doi/full/10.1021/acs.jpcc.1c09193

Requests for further permissions should be directed to the American Chemical Society.

The following is proof of copyright permissions:

2/9/22, 3:01 PM Mail - Jeramie C Rushing - Outlook

Reuse of own publication for dissertation -- DOI: 10.1021/acs.jpcc.1c09193

ACS Publications <support@services.acs.org>
Wed 2/9/2022 1:27 PM
To: Jeramie C Rushing <jrush16@lsu.edu>

Dear Jeramie Rushing,

Your permission requested is granted and there is no fee for this reuse. In your planned reuse, you must cite the ACS article as the source, add this direct link https://pubs.acs.org/doi/full/10.1021/acs.jpcc.1c09193, and include a notice to readers that further permissions related to the material excerpted should be directed to the ACS.

If you need further assistance, please let me know.

Best regards,
Raquel

~~~~~~~~~~~~~~~~~~~~~~~~~~~~~~~~~~~~
Raquel Picar-Simpson
ACS Publications Support
Customer Services & Information
Website: https://acs.service-now.com/acs
Email: support@services.acs.org
Phone: 800-227-9919 | 202-872-(HELP) 4357
~~~~~~~~~~~~~~~~~~~~~~~~~~~~~~~~~~~~

LIST OF REFERENCES

1. Aifantis, K.E., S.A. Hackney, and R.V. Kumar, *High energy density lithium batteries*. 2010: Wiley Online Library.

2. Armand, M. and J.-M. Tarascon, *Building better batteries.* nature, 2008. **451**(7179): p. 652-657.

3. Nagaura, T., *Proceedings of the 5th International Seminar on lithium battery technology and applications.* 1990.

4. Divya, K. and J. Østergaard, *Battery energy storage technology for power systems—An overview.* Electric power systems research, 2009. **79**(4): p. 511-520.

5. Dunn, B., H. Kamath, and J.-M. Tarascon, *Electrical energy storage for the grid: a battery of choices.* Science, 2011. **334**(6058): p. 928-935.

6. Xu, K., *Electrolytes and Interphases in Li-Ion Batteries and Beyond.* Chemical Reviews, 2014. **114**(23): p. 11503-11618.

7. Ding, F., et al., *Dendrite-free lithium deposition via self-healing electrostatic shield mechanism.* Journal of the American Chemical Society, 2013. **135**(11): p. 4450-4456.

8. Han, G.-B., et al., *Enhanced cycling performance of lithium metal secondary batteries with succinic anhydride as an electrolyte additive.* Electrochimica Acta, 2014. **115**: p. 525-530.

9. Markevich, E., et al., *Very stable lithium metal stripping–plating at a high rate and high areal capacity in fluoroethylene carbonate-based organic electrolyte solution.* ACS Energy Letters, 2017. **2**(6): p. 1321-1326.

10. Zhang, X.Q., et al., *Fluoroethylene carbonate additives to render uniform Li deposits in lithium metal batteries.* Advanced Functional Materials, 2017. **27**(10): p. 1605989.

11. Zhang, Y., et al., *Dendrite-free lithium deposition with self-aligned nanorod structure.* Nano letters, 2014. **14**(12): p. 6889-6896.

12. Xu, K., *Nonaqueous liquid electrolytes for lithium-based rechargeable batteries.* Chemical reviews, 2004. **104**(10): p. 4303-4418.

13. Delp, S.A., et al., *Importance of reduction and oxidation stability of high voltage electrolytes and additives.* Electrochimica Acta, 2016. **209**: p. 498-510.

14. von Wald Cresce, A., O. Borodin, and K. Xu, *Correlating Li+ solvation sheath structure with interphasial chemistry on graphite.* The Journal of Physical Chemistry C, 2012. **116**(50): p. 26111-26117.

15. Aroca, R., et al., *Vibrational spectra and ion-pair properties of lithium hexafluorophosphate in ethylene carbonate based mixed-solvent systems for lithium batteries.* Journal of Solution Chemistry, 2000. **29**(10): p. 1047-1060.

16. Giorgini, M.G., et al., *Solvation structure around the Li+ ion in mixed cyclic/linear carbonate solutions unveiled by the Raman noncoincidence effect.* The Journal of Physical Chemistry Letters, 2015. **6**(16): p. 3296-3302.

17. Seo, D.M., et al., *Role of Mixed Solvation and Ion Pairing in the Solution Structure of Lithium Ion Battery Electrolytes.* The Journal of Physical Chemistry C, 2015. **119**(25): p. 14038-14046.

18. Jeong, S.-K., et al., *Electrochemical intercalation of lithium ion within graphite from propylene carbonate solutions.* Electrochemical and Solid State Letters, 2002. **6**(1): p. A13.

19. McMillan, R., et al., *Fluoroethylene carbonate electrolyte and its use in lithium ion batteries with graphite anodes.* Journal of Power Sources, 1999. **81**: p. 20-26.

20. Janssen, P., et al., *Fluorinated electrolyte compound as a bi-functional interphase additive for both, anodes and cathodes in lithium-ion batteries.* Journal of the Electrochemical Society, 2018. **165**(14): p. A3525.

21. Li, T., et al., *Fluorinated solid-electrolyte interphase in high-voltage lithium metal batteries.* Joule, 2019. **3**(11): p. 2647-2661.

22. Cuisinier, M., et al., *Unique behaviour of nonsolvents for polysulphides in lithium–sulphur batteries.* Energy & Environmental Science, 2014. **7**(8): p. 2697-2705.

23. Dokko, K., et al., *Solvate ionic liquid electrolyte for Li–S batteries.* Journal of The Electrochemical Society, 2013. **160**(8): p. A1304.

24. Dong, X., et al., *High-energy rechargeable metallic lithium battery at− 70 C enabled by a cosolvent electrolyte.* Angewandte Chemie, 2019. **131**(17): p. 5679-5683.

25. Huang, F., et al., *Enhancing metallic lithium battery performance by tuning the electrolyte solution structure.* Journal of Materials Chemistry A, 2018. **6**(4): p. 1612-1620.

26. Piao, N., et al., *Countersolvent Electrolytes for Lithium-Metal Batteries.* Advanced Energy Materials, 2020. **10**(10): p. 1903568.

27. Qiu, F., et al., *A concentrated ternary-salts electrolyte for high reversible Li metal battery with slight excess Li.* Advanced Energy Materials, 2019. **9**(6): p. 1803372.

28. Chen, S., et al., *High-voltage lithium-metal batteries enabled by localized high-concentration electrolytes.* Advanced Materials, 2018. **30**(21): p. 1706102.

29. Yu, L., et al., *A localized high-concentration electrolyte with optimized solvents and lithium difluoro (oxalate) borate additive for stable lithium metal batteries.* ACS Energy Letters, 2018. **3**(9): p. 2059-2067.

30. Zheng, J., et al., *High-fluorinated electrolytes for Li–S batteries.* Advanced energy materials, 2019. **9**(16): p. 1803774.

31. Ma, G., et al., *Pseudoconcentrated electrolyte with high ionic conductivity and stability enables high-voltage lithium-ion battery chemistry.* ACS Applied Energy Materials, 2018. **1**(10): p. 5446-5452.

32. Webber, A., *Conductivity and Viscosity of Solutions of LiCF3 SO 3, Li (CF 3 SO 2) 2 N, and Their Mixtures.* Journal of the Electrochemical Society, 1991. **138**(9): p. 2586.

33. Jayathilaka, P., et al., *Dielectric relaxation, ionic conductivity and thermal studies of the gel polymer electrolyte system PAN/EC/PC/LiTFSI.* Solid State Ionics, 2003. **156**(1-2): p. 179-195.

34. Ostrovskii, D., et al., *Molecular and ionic interactions in poly (acrylonitrile)-and poly (methylmetacrylate)-based gel electrolytes.* The Journal of chemical physics, 1998. **109**(17): p. 7618-7624.

35. Ostrovskii, D., M. Edvardsson, and P. Jacobsson, *Weak polymer–electrolyte interaction revealed by Fermi resonance perturbed Raman bands.* Journal of Raman Spectroscopy, 2003. **34**(1): p. 40-49.

36. Karan, N., et al., *Solid polymer electrolytes based on polyethylene oxide and lithium trifluoro-methane sulfonate (PEO–LiCF3SO3): Ionic conductivity and dielectric relaxation.* Solid State Ionics, 2008. **179**(19-20): p. 689-696.

37. Svanberg, C., et al., *Diffusive and segmental dynamics in polymer gel electrolytes.* The Journal of Chemical Physics, 1999. **111**(24): p. 11216-11221.

38. Hamm, P. and M. Zanni, *Concepts and methods of 2D infrared spectroscopy*. 2011: Cambridge University Press.

39. Jeener, J., et al., *Investigation of exchange processes by two-dimensional NMR spectroscopy.* The Journal of chemical physics, 1979. **71**(11): p. 4546-4553.

40. Zanni, M.T. and R.M. Hochstrasser, *Two-dimensional infrared spectroscopy: a promising new method for the time resolution of structures.* Current opinion in structural biology, 2001. **11**(5): p. 516-522.

41. Mukamel, S., *Multidimensional femtosecond correlation spectroscopies of electronic and vibrational excitations.* Annual review of physical chemistry, 2000. **51**(1): p. 691-729.

42. Abramczyk, H., *Introduction to laser spectroscopy*. 2005: Elsevier.

43. Kwak, K., et al., *Frequency-frequency correlation functions and apodization in two-dimensional infrared vibrational echo spectroscopy: A new approach.* The Journal of chemical physics, 2007. **127**(12): p. 124503.

44. Kwac, K. and M. Cho, *Molecular dynamics simulation study of N-methylacetamide in water. II. Two-dimensional infrared pump–probe spectra.* The Journal of chemical physics, 2003. **119**(4): p. 2256-2263.

45. Lim, J., et al., *Two-dimensional infrared spectroscopy and molecular dynamics simulation studies of nonaqueous lithium ion battery electrolytes.* The Journal of Physical Chemistry B, 2019. **123**(31): p. 6651-6663.

46. Yuan, R. and M.D. Fayer, *Dynamics of water molecules and ions in concentrated lithium chloride solutions probed with ultrafast 2D IR spectroscopy.* The Journal of Physical Chemistry B, 2019. **123**(35): p. 7628-7639.

47. Ji, M., S. Park, and K.J. Gaffney, *Dynamics of ion assembly in solution: 2DIR spectroscopy study of LiNCS in benzonitrile.* The Journal of Physical Chemistry Letters, 2010. **1**(12): p. 1771-1775.

48. Chen, X., et al., *Structure and Dynamics of the Lithium-Ion Solvation Shell in Ureas.* The Journal of Physical Chemistry B, 2019. **123**(46): p. 9889-9898.

49. Fulfer, K.D. and D.G. Kuroda, *Solvation Structure and Dynamics of the Lithium Ion in Organic Carbonate-Based Electrolytes: A Time-Dependent Infrared Spectroscopy Study.* The Journal of Physical Chemistry C, 2016. **120**(42): p. 24011-24022.

50. Fulfer, K.D. and D.G. Kuroda, *Ion speciation of lithium hexafluorophosphate in dimethyl carbonate solutions: an infrared spectroscopy study.* Physical Chemistry Chemical Physics, 2018. **20**(35): p. 22710-22718.

51. Galle Kankanamge, S.R. and D.G. Kuroda, *Molecular structure, chemical exchange, and conductivity mechanism of high concentration LiTFSI electrolytes.* The Journal of Physical Chemistry B, 2020. **124**(10): p. 1965-1977.

52. Fong, R., U. Von Sacken, and J.R. Dahn, *Studies of lithium intercalation into carbons using nonaqueous electrochemical cells.* Journal of The Electrochemical Society, 1990. **137**(7): p. 2009.

53. Girishkumar, G., et al., *Lithium− air battery: promise and challenges.* The Journal of Physical Chemistry Letters, 2010. **1**(14): p. 2193-2203.

54. Goodenough, J.B. and Y. Kim, *Challenges for rechargeable Li batteries.* Chemistry of materials, 2010. **22**(3): p. 587-603.

55. Manthiram, A., Y. Fu, and Y.-S. Su, *Challenges and prospects of lithium–sulfur batteries.* Accounts of chemical research, 2013. **46**(5): p. 1125-1134.

56. Ohzuku, T. and R.J. Brodd, *An overview of positive-electrode materials for advanced lithium-ion batteries.* Journal of Power Sources, 2007. **174**(2): p. 449-456.

57. Chan, C.K., et al., *High-performance lithium battery anodes using silicon nanowires.* Nature nanotechnology, 2008. **3**(1): p. 31-35.

58. Kasavajjula, U., C. Wang, and A.J. Appleby, *Nano-and bulk-silicon-based insertion anodes for lithium-ion secondary cells.* Journal of power sources, 2007. **163**(2): p. 1003-1039.

59. Cheng, X.-B., et al., *Toward safe lithium metal anode in rechargeable batteries: a review.* Chemical reviews, 2017. **117**(15): p. 10403-10473.

60. Lin, D., Y. Liu, and Y. Cui, *Reviving the lithium metal anode for high-energy batteries.* Nature nanotechnology, 2017. **12**(3): p. 194.

61. Ozawa, K., *Lithium-ion rechargeable batteries with LiCoO2 and carbon electrodes: the LiCoO2/C system.* Solid State Ionics, 1994. **69**(3-4): p. 212-221.

62. Nishi, Y., H. Azuma, and A. Omaru, *Non aqueous electrolyte cell*. 1990, Google Patents.

63. Krause, L.J., et al., *Corrosion of aluminum at high voltages in non-aqueous electrolytes containing perfluoroalkylsulfonyl imides; new lithium salts for lithium-ion cells.* Journal of power sources, 1997. **68**(2): p. 320-325.

64. Ue, M., *Mobility and ionic association of lithium and quaternary ammonium salts in propylene carbonate and γ-butyrolactone.* Journal of the electrochemical society, 1994. **141**(12): p. 3336.

65. Ue, M. and S. Mori, *Mobility and ionic association of lithium salts in a propylene carbonate-ethyl methyl carbonate mixed solvent.* Journal of the Electrochemical Society, 1995. **142**(8): p. 2577.

66. Barthel, J. and R. Neueder, *Electrolyte data collection*. 1992: Dechema.

67. Lide, D.R. and G.W. Milne, *Handbook of data on common organic compounds*. 1995: CRC press.

68. Ue, M., K. Ida, and S. Mori, *Electrochemical properties of organic liquid electrolytes based on quaternary onium salts for electrical double-layer capacitors.* Journal of the Electrochemical Society, 1994. **141**(11): p. 2989.

69. Guyomard, D. and J. Tarascon, *Rechargeable Li1+ x Mn2 O 4/Carbon Cells with a New Electrolyte Composition: Potentiostatic Studies and Application to Practical Cells.* Journal of the electrochemical society, 1993. **140**(11): p. 3071.

70. Tarascon, J. and D. Guyomard, *New electrolyte compositions stable over the 0 to 5 V voltage range and compatible with the Li1+ xMn2O4/carbon Li-ion cells.* Solid State Ionics, 1994. **69**(3-4): p. 293-305.

71. Pistoia, G., M. De Rossi, and B. Scrosati, *Study of the behavior of ethylene carbonate as a nonaqueous battery solvent.* J. Electrochem. Soc.;(United States), 1970. **117**(4).

72. Bogle, X., et al., *Understanding Li+–solvent interaction in nonaqueous carbonate electrolytes with 17O NMR.* The Journal of Physical Chemistry Letters, 2013. **4**(10): p. 1664-1668.

73. Skarmoutsos, I., et al., *Li+ Solvation in Pure, Binary, and Ternary Mixtures of Organic Carbonate Electrolytes.* The Journal of Physical Chemistry C, 2015. **119**(9): p. 4502-4515.

74. von Cresce, A. and K. Xu, *Preferential solvation of Li+ directs formation of interphase on graphitic anode.* Electrochemical and Solid State Letters, 2011. **14**(10): p. A154.

75. Wang, J., et al., *Ion–molecule interactions in solutions of lithium perchlorate in propylene carbonate+ diethyl carbonate mixtures: an IR and molecular orbital study.* Spectrochimica Acta Part A: Molecular and Biomolecular Spectroscopy, 2002. **58**(10): p. 2097-2104.

76. Chen, S., et al., *High-efficiency lithium metal batteries with fire-retardant electrolytes.* Joule, 2018. **2**(8): p. 1548-1558.

77. Doi, T., et al., *Low-viscosity γ-butyrolactone-based concentrated electrolyte solutions for LiNi0. 5Mn1. 5O4 positive electrodes in lithium-ion batteries.* ChemElectroChem, 2017. **4**(9): p. 2398-2403.

78. Yoshida, K., et al., *Oxidative-stability enhancement and charge transport mechanism in glyme–lithium salt equimolar complexes.* Journal of the American Chemical Society, 2011. **133**(33): p. 13121-13129.

79. Ding, F., et al., *Effects of carbonate solvents and lithium salts on morphology and coulombic efficiency of lithium electrode.* Journal of The Electrochemical Society, 2013. **160**(10): p. A1894.

80. Qian, J., et al., *Anode-free rechargeable lithium metal batteries.* Advanced Functional Materials, 2016. **26**(39): p. 7094-7102.

81. Qian, J., et al., *High rate and stable cycling of lithium metal anode.* Nature communications, 2015. **6**(1): p. 1-9.

82. Wang, J., et al., *Superconcentrated electrolytes for a high-voltage lithium-ion battery.* Nature communications, 2016. **7**(1): p. 1-9.

83. Yamada, Y., et al., *Advances and issues in developing salt-concentrated battery electrolytes.* Nature Energy, 2019. **4**(4): p. 269-280.

84. Doi, T., et al., *Dilution of highly concentrated LiBF4/propylene carbonate electrolyte solution with fluoroalkyl ethers for 5-V LiNi0. 5Mn1. 5O4 positive electrodes.* Journal of The Electrochemical Society, 2017. **164**(1): p. A6412.

85. Moon, H., et al., *Solvent activity in electrolyte solutions controls electrochemical reactions in Li-ion and Li-sulfur batteries.* The Journal of Physical Chemistry C, 2015. **119**(8): p. 3957-3970.

86. Ueno, K., et al., *Li+ solvation and ionic transport in lithium solvate ionic liquids diluted by molecular solvents.* The Journal of Physical Chemistry C, 2016. **120**(29): p. 15792-15802.

87. Ueno, K., et al., *A design approach to lithium-ion battery electrolyte based on diluted solvate ionic liquids.* Journal of The Electrochemical Society, 2016. **164**(1): p. A6088.

88. Wang, H., et al., *A reversible dendrite-free high-areal-capacity lithium metal electrode.* Nature communications, 2017. **8**(1): p. 1-9.

89. Eshetu, G.G., et al., *Fire behavior of carbonates-based electrolytes used in Li-ion rechargeable batteries with a focus on the role of the LiPF6 and LiFSI salts.* Journal of Power Sources, 2014. **269**: p. 804-811.

90. Ribière, P., et al., *Investigation on the fire-induced hazards of Li-ion battery cells by fire calorimetry.* Energy & Environmental Science, 2012. **5**(1): p. 5271-5280.

91. Cheng, X., et al., *Gel polymer electrolytes for electrochemical energy storage.* Advanced Energy Materials, 2018. **8**(7): p. 1702184.

92. Ngai, K.S., et al., *A review of polymer electrolytes: fundamental, approaches and applications.* Ionics, 2016. **22**(8): p. 1259-1279.

93. Stephan, A.M., *Review on gel polymer electrolytes for lithium batteries.* European polymer journal, 2006. **42**(1): p. 21-42.

94. Aihara, Y., S. Arai, and K. Hayamizu, *Ionic conductivity, DSC and self diffusion coefficients of lithium, anion, polymer, and solvent of polymer gel electrolytes: the structure of the gels and the diffusion mechanism of the ions.* Electrochimica acta, 2000. **45**(8-9): p. 1321-1326.

95. Kumar, R. and S. Sekhon, *Evidence of ion pair breaking by dispersed polymer in polymer gel electrolytes.* Ionics, 2004. **10**(1): p. 10-16.

96. Johansson, P., et al., *Mixed solvent and polymer coordination in PAN and PMMA gel polymer electrolytes studied by ab initio calculations and Raman spectroscopy.* The Journal of Physical Chemistry B, 2003. **107**(46): p. 12622-12627.

97. Ostrovskii, D., et al., *An electrochemical and Raman spectroscopical study of gel polymer electrolytes for lithium batteries.* Solid State Ionics, 1998. **106**(1-2): p. 19-24.

98. Bamford, D., et al., *Ionic conductivity, glass transition, and local free volume in poly (ethylene oxide) electrolytes: Single and mixed ion conductors.* The Journal of chemical physics, 2003. **118**(20): p. 9420-9432.

99. Bohnke, O., et al., *Fast ion transport in new lithium electrolytes gelled with PMMA. 2. Influence of lithium salt concentration.* Solid State Ionics, 1993. **66**(1-2): p. 105-112.

100. Croce, F., et al., *Nanocomposite polymer electrolytes for lithium batteries.* Nature, 1998. **394**(6692): p. 456-458.

101. Croce, F., et al., *Physical and chemical properties of nanocomposite polymer electrolytes.* The Journal of Physical Chemistry B, 1999. **103**(48): p. 10632-10638.

102. Ericson, H., et al., *Poly (methyl methacrylate)-based protonic gel electrolytes: a spectroscopic study.* Electrochimica acta, 2000. **45**(8-9): p. 1409-1414.

103. Panero, S. and B. Scrosati, *Gelification of liquid–polymer systems: a valid approach for the development of various types of polymer electrolyte membranes.* Journal of power sources, 2000. **90**(1): p. 13-19.

104. Huang, B., et al., *The mechanism of lithium ion transport in polyacrylonitrile-based polymer electrolytes.* Solid State Ionics, 1996. **91**(3-4): p. 279-284.

105. Stallworth, P., et al., *Sodium-23 NMR and complex impedance studies of gel electrolytes based on poly (acrylonitrile).* Solid State Ionics, 1994. **73**(1-2): p. 119-126.

106. Ding, M.S., *Conductivity and viscosity of PC-DEC and PC-EC solutions of LiBF4.* Journal of the Electrochemical Society, 2003. **151**(1): p. A40.

107. Ding, M.S. and T.R. Jow, *How Conductivities and Viscosities of PC-DEC and PC-EC Solutions of LiBF4, LiPF6, LiBOB, Et4 NBF 4, and Et4 NPF 6 Differ and Why.* Journal of the Electrochemical Society, 2004. **151**(12): p. A2007.

108. Yamada, Y., et al., *Unusual stability of acetonitrile-based superconcentrated electrolytes for fast-charging lithium-ion batteries.* Journal of the American Chemical Society, 2014. **136**(13): p. 5039-5046.

109. Berhaut, C.L., et al., *Ionic association analysis of LiTDI, LiFSI and LiPF 6 in EC/DMC for better Li-ion battery performances.* RSC advances, 2019. **9**(8): p. 4599-4608.

110. Humbert, M.T., Y. Zhang, and E.J. Maginn, *Assessing the reliability of computing ion pair lifetimes and self-diffusivity to predict experimental viscosity trends of ionic liquids.* Molecular Systems Design & Engineering, 2017. **2**(3): p. 293-300.

111. Zhang, Y. and E.J. Maginn, *Direct correlation between ionic liquid transport properties and ion pair lifetimes: A molecular dynamics study.* The journal of physical chemistry letters, 2015. **6**(4): p. 700-705.

112. Hamm, P., M. Lim, and R.M. Hochstrasser, *Non-Markovian dynamics of the vibrations of ions in water from femtosecond infrared three-pulse photon echoes.* Physical review letters, 1998. **81**(24): p. 5326.

113. Fayer, M., *Dynamics of liquids, molecules, and proteins measured with ultrafast 2D IR vibrational echo chemical exchange spectroscopy.* Annual review of physical chemistry, 2009. **60**: p. 21-38.

114. Nagayama, K., et al., *Experimental techniques of two-dimensional correlated spectroscopy.* Journal of Magnetic Resonance (1969), 1980. **40**(2): p. 321-334.

115. Khalil, M., N. Demirdöven, and A. Tokmakoff, *Coherent 2D IR spectroscopy: Molecular structure and dynamics in solution.* The Journal of Physical Chemistry A, 2003. **107**(27): p. 5258-5279.

116. Griffiths, P.R. and J.A. De Haseth, *Fourier transform infrared spectrometry*. Vol. 171. 2007: John Wiley & Sons.

117. Barthel, J., R. Buchner, and E. Wismeth, *FTIR spectroscopy of ion solvation of LiClO4 and LiSCN in acetonitrile, benzonitrile, and propylene carbonate.* Journal of Solution Chemistry, 2000. **29**(10): p. 937-954.

118. Guerin, A.C., et al., *Determining the energetics of the hydrogen bond through ftir: A hands-on physical chemistry lab experiment.* Journal of Chemical Education, 2016. **93**(6): p. 1124-1129.

119. Ma, J., et al., *Unusual molecular mechanism behind the thermal response of polypeptoids in aqueous solutions.* Physical Chemistry Chemical Physics, 2017. **19**(17): p. 10878-10888.

120. Cui, Y., et al., *Solvation dynamics of an ionic probe in choline chloride-based deep eutectic solvents.* Physical Chemistry Chemical Physics, 2016. **18**(46): p. 31471-31479.

121. Cui, Y. and D.G. Kuroda, *Evidence of molecular heterogeneities in amide-based deep eutectic solvents.* The Journal of Physical Chemistry A, 2018. **122**(5): p. 1185-1193.

122. Cui, Y., et al., *Molecularly heterogeneous structure of a nonionic deep eutectic solvent composed of n-methylacetamide and lauric acid.* The Journal of Physical Chemistry B, 2019. **123**(18): p. 3984-3993.

123. Kankanamge, S.R.G. and D.G. Kuroda, *Molecular structure and ultrafast dynamics of sodium thiocyanate ion pairs formed in glymes of different lengths.* Physical Chemistry Chemical Physics, 2019. **21**(2): p. 833-841.

124. Kim, Y.S. and R.M. Hochstrasser, *Applications of 2D IR spectroscopy to peptides, proteins, and hydrogen-bond dynamics.* The Journal of Physical Chemistry B, 2009. **113**(24): p. 8231-8251.

125. Baiz, C.R., et al., *A molecular interpretation of 2D IR protein folding experiments with Markov state models.* Biophysical journal, 2014. **106**(6): p. 1359-1370.

126. Baiz, C.R., et al., *Coherent two-dimensional infrared spectroscopy: Quantitative analysis of protein secondary structure in solution.* Analyst, 2012. **137**(8): p. 1793-1799.

127. Gobeze, H.B., et al., *Bottom-Up Approach to Assess the Molecular Structure of Aqueous Poly (N-Isopropylacrylamide) at Room Temperature via Infrared Spectroscopy.* The Journal of Physical Chemistry B, 2020. **124**(51): p. 11699-11710.

128. Kelsheimer, C. and S. Garrett-Roe, *Intramolecular Vibrational Energy Relaxation of CO2 in Cross-Linked Poly (ethylene glycol) Diacrylate-Based Ion Gels.* The Journal of Physical Chemistry B, 2020. **125**(5): p. 1402-1415.

129. Kim, H. and M. Cho, *Infrared probes for studying the structure and dynamics of biomolecules.* Chemical reviews, 2013. **113**(8): p. 5817-5847.

130. Lee, K.-K., et al., *Ion-pairing dynamics of Li+ and SCN− in dimethylformamide solution: Chemical exchange two-dimensional infrared spectroscopy.* The Journal of chemical physics, 2011. **134**(6): p. 064506.

131. Peng, Y. and P. Wu, *A two dimensional infrared correlation spectroscopic study on the structure changes of PVDF during the melting process.* Polymer, 2004. **45**(15): p. 5295-5299.

132. Ren, Z., et al., *Thiocyanate as a Local Probe of Ultrafast Structure and Dynamics in Imidazolium-Based Ionic Liquids: Water-Induced Heterogeneity and Cation-Induced Ion Pairing.* The Journal of Physical Chemistry B, 2015. **119**(13): p. 4699-4712.

133. Ren, Z., et al., *Ultrafast structure and dynamics in ionic liquids: 2D-IR spectroscopy probes the molecular origin of viscosity.* The journal of physical chemistry letters, 2014. **5**(9): p. 1541-1546.

134. Sun, B., et al., *A FTIR and 2D-IR spectroscopic study on the microdynamics phase separation mechanism of the poly (N-isopropylacrylamide) aqueous solution.* Macromolecules, 2008. **41**(4): p. 1512-1520.

135. Yan, C., et al., *Water dynamics in polyacrylamide hydrogels.* Journal of the American Chemical Society, 2018. **140**(30): p. 9466-9477.

136. Kubo, R., *A stochastic theory of line shape.* Stochastic processes in chemical physics, 1969. **15**: p. 101-127.

137. Asaki, M.T., et al., *Generation of 11-fs pulses from a self-mode-locked Ti: sapphire laser.* Optics letters, 1993. **18**(12): p. 977-979.

138. Baumgartner, R. and R. Byer, *Optical parametric amplification.* IEEE Journal of Quantum Electronics, 1979. **15**(6): p. 432-444.

139. Tokmakoff, A., C. Marshall, and M.D. Fayer, *Optical parametric amplification of 1-kHz high-energy picosecond midinfrared pulses and application to infrared transient-grating experiments on diamond.* JOSA B, 1993. **10**(9): p. 1785-1791.

140. Tsuda, S., et al., *Mode-locking ultrafast solid-state lasers with saturable Bragg reflectors.* IEEE Journal of Selected Topics in Quantum Electronics, 1996. **2**(3): p. 454-464.

141. Wynne, K., G.D. Reid, and R.M. Hochstrasser, *Regenerative amplification of 30-fs pulses in Ti: sapphire at 5 kHz.* Optics letters, 1994. **19**(12): p. 895-897.

142. Asplund, M., M.T. Zanni, and R.M. Hochstrasser, *Two-dimensional infrared spectroscopy of peptides by phase-controlled femtosecond vibrational photon echoes.* Proceedings of the National Academy of Sciences, 2000. **97**(15): p. 8219-8224.

143. Eckbreth, A.C., *BOXCARS: Crossed-beam phase-matched CARS generation in gases.* Applied Physics Letters, 1978. **32**(7): p. 421-423.

144. Lepetit, L., G. Chériaux, and M. Joffre, *Linear techniques of phase measurement by femtosecond spectral interferometry for applications in spectroscopy.* JOSA B, 1995. **12**(12): p. 2467-2474.

145. DeFlores, L.P., R.A. Nicodemus, and A. Tokmakoff, *Two-dimensional Fourier transform spectroscopy in the pump-probe geometry.* Optics letters, 2007. **32**(20): p. 2966-2968.

146. Kuo, C.-H., et al., *Correlation of the Vibrations of the Aqueous Azide Ion with the O− H Modes of Bound Water Molecules.* The Journal of Physical Chemistry B, 2007. **111**(50): p. 14028-14033.

147. Dorrer, C., et al., *Spectral resolution and sampling issues in Fourier-transform spectral interferometry.* JOSA B, 2000. **17**(10): p. 1795-1802.

148. Kim, Y.S., J. Wang, and R.M. Hochstrasser, *Two-dimensional infrared spectroscopy of the alanine dipeptide in aqueous solution.* The journal of physical chemistry B, 2005. **109**(15): p. 7511-7521.

149. Zhang, X.L. and D.G. Kuroda, *An ab initio molecular dynamics study of the solvation structure and ultrafast dynamics of lithium salts in organic carbonates: A comparison between linear and cyclic carbonates.* Journal of Chemical Physics, 2019. **150**(18): p. 184501.

150. Ding, M.S., *Electrolytic conductivity and glass transition temperature as functions of salt content, solvent composition, or temperature for LiPF6 in propylene carbonate plus diethyl carbonate.* Journal of Chemical and Engineering Data, 2003. **48**(3): p. 519-528.

151. Ding, M.S., et al., *Change of conductivity with salt content, solvent composition, and temperature for electrolytes of LiPF6 in ethylene carbonate-ethyl methyl carbonate.* Journal of the Electrochemical Society, 2001. **148**(10): p. A1196-A1204.

152. Chapman, N., et al., *Spectroscopic and Density Functional Theory Characterization of Common Lithium Salt Solvates in Carbonate Electrolytes for Lithium Batteries.* The Journal of Physical Chemistry C, 2017. **121**(4): p. 2135-2148.

153. Xu, K. and A. Von Cresce, *Li+-Solvation Structure Directs Interphasial Processes on Graphitic Anodes.* ECS Transactions, 2012. **41**(41): p. 187-193.

154. Morita, M., et al., *A Raman spectroscopic study of organic electrolyte solutions based on binary solvent systems of ethylene carbonate with low viscosity solvents which dissolve different lithium salts.* Journal of the Chemical Society, Faraday Transactions, 1998. **94**(23): p. 3451-3456.

155. Hyodo, S.A. and K. Okabayashi, *Raman Intensity Study of Local-Structure in Non-Aqueous Electrolyte-Solutions .2. Cation Solvent Interaction in Mixed-Solvent Systems and Selective Solvation.* Electrochimica Acta, 1989. **34**(11): p. 1557-1561.

156. Brodin, A. and P. Jacobsson, *Dipolar interaction and molecular ordering in liquid propylene carbonate: Anomalous dielectric susceptibility and Raman non-coincidence effect.* Journal of Molecular Liquids, 2011. **164**(1): p. 17-21.

157. Borodin, O., et al., *Competitive lithium solvation of linear and cyclic carbonates from quantum chemistry.* Physical Chemistry Chemical Physics, 2016. **18**(1): p. 164-175.

158. Xu, K., et al., *Solvation sheath of Li+ in nonaqueous electrolytes and its implication of graphite/electrolyte interface chemistry.* The Journal of Physical Chemistry C, 2007. **111**(20): p. 7411-7421.

159. Maeda, S., et al., *Local Structure of Li+ in Concentrated Ethylene Carbonate Solutions Studied by Low-Frequency Raman Scattering and Neutron Diffraction with Li-6/Li-7 Isotopic Substitution Methods.* The Journal of Physical Chemistry B, 2017. **121**(48): p. 10979-10987.

160. Fulfer, K.D. and D.G. Kuroda, *A comparison of the solvation structure and dynamics of the lithium ion in linear organic carbonates with different alkyl chain lengths.* Physical Chemistry Chemical Physics, 2017. **19**(36): p. 25140-25150.

161. Dranka, M., et al., *An insight into coordination ability of dicyanoimidazolato anions toward lithium in presence of acetonitrile. Crystal structures of novel lithium battery electrolyte salts.* Polyhedron, 2013. **51**: p. 111-116.

162. Scheers, J., et al., *Ion-ion and ion-solvent interactions in lithium imidazolide electrolytes studied by Raman spectroscopy and DFT models.* Physical Chemistry Chemical Physics, 2011. **13**(23): p. 11136-11147.

163. Niedzicki, L., et al., *Liquid electrolytes based on new lithium conductive imidazole salts.* Journal of Power Sources, 2011. **196**(3): p. 1386-1391.

164. Niedzicki, L., et al., *Modern generation of polymer electrolytes based on lithium conductive imidazole salts.* Journal of Power Sources, 2009. **192**(2): p. 612-617.

165. Jankowski, P., et al., *Understanding of Lithium 4,5-Dicyanoimidazolate-Poly(ethylene oxide) System: Influence of the Architecture of the Solid Phase on the Conductivity.* The Journal of Physical Chemistry C, 2016. **120**(41): p. 23358-23367.

166. Niedzicki, L., et al., Optimization of the lithium-ion cell electrolyte composition through the use of the LiTDI salt. Electrochimica Acta, 2014. 117: p. 224-229.

167. Niedzicki, L., et al., *Lithium cation conducting TDI anion-based ionic liquids.* Physical Chemistry Chemical Physics, 2014. **16**(23): p. 11417-11425.

168. Scheers, J., et al., *Benzimidazole and imidazole lithium salts for battery electrolytes.* Journal of Power Sources, 2010. **195**(18): p. 6081-6087.

169. McOwen, D.W., et al., *Anion Coordination Interactions in Solvates with the Lithium Salts LiDCTA and LiTDI.* The Journal of Physical Chemistry C, 2014. **118**(15): p. 7781-7787.

170. Niedzicki, L., et al., *New covalent salts of the 4+V class for Li batteries.* Journal of Power Sources, 2011. **196**(20): p. 8696-8700.

171. Berhaut, C.L., et al., *LiTDI as electrolyte salt for Li-ion batteries: transport properties in EC/DMC.* Electrochimica Acta, 2015. **180**: p. 778-787.

172. Kuroda, D.G. and R.M. Hochstrasser, *Two-dimensional infrared spectral signature and hydration of the oxalate dianion.* Journal of Chemical Physics, 2011. **135**(20): p. 204502.

173. Cui, Y.W. and D.G. Kuroda, *Evidence of Molecular Heterogeneities in Amide-Based Deep Eutectic Solvents.* The Journal of Physical Chemistry A, 2018. **122**(5): p. 1185-1193.

174. Vorobyev, D.Y., et al., *Water-Induced Relaxation of a Degenerate Vibration of Guanidium Using 2D IR Echo Spectroscopy.* The Journal of Physical Chemistry B, 2010. **114**(8): p. 2944-2953.

175. Hunt, N.T., *2D-IR spectroscopy: ultrafast insights into biomolecule structure and function.* Chemical Society Reviews, 2009. **38**(7): p. 1837-1848.

176. Sun, Z., et al., *Contact Ion Pair Formation between Hard Acids and Soft Bases in Aqueous Solutions Observed with 2DIR Spectroscopy.* The Journal of Physical Chemistry B, 2013. **117**(49): p. 15306-15312.

177. Park, K.H., et al., *Real-Time Probing of Ion Pairing Dynamics with 2DIR Spectroscopy.* Chemphyschem, 2010. **11**(17): p. 3632-3637.

178. Ji, M.B., S. Park, and K.J. Gaffney, *Dynamics of Ion Assembly in Solution: 2DIR Spectroscopy Study of LiNCS in Benzonitrile.* Journal of Physical Chemistry Letters, 2010. **1**(12): p. 1771-1775.

179. Bian, H.T., et al., *Cation Effects on Rotational Dynamics of Anions and Water Molecules in Alkali (Li+, Na+, K+, Cs+) Thiocyanate (SCN-) Aqueous Solutions.* The Journal of Physical Chemistry B, 2013. **117**(26): p. 7972-7984.

180. Yuan, R.F., C. Yan, and M. Fayer, *Ion-Molecule Complex Dissociation and Formation Dynamics in LiCl Aqueous Solutions from 2D IR Spectroscopy.* The Journal of Physical Chemistry B, 2018. **122**(46): p. 10582-10592.

181. Roy, V.P. and K.J. Kubarych, *Interfacial Hydration Dynamics in Cationic Micelles Using 2D-IR and NMR.* The Journal of Physical Chemistry B, 2017. **121**(41): p. 9621-9630.

182. Kuroda, D.G., et al., *Vibrational dynamics of a non-degenerate ultrafast rotor: The (C12,C13)-oxalate ion.* Journal of Chemical Physics, 2013. **139**(16): p. 164514.

183. Johansson, P., et al., *Spectroscopic and theoretical study of the 1,2,3-Triazole-4,5-dicarbonitrile anion and its lithium ion pairs.* Solid State Ionics, 2003. **156**(1-2): p. 129-139.

184. Stoyanov, S.S., *Scaling of Computed Cyano-Stretching Frequencies and IR Intensities of Nitriles, Their Anions, and Radicals.* The Journal of Physical Chemistry A, 2010. **114**(15): p. 5149-5161.

185. Xuan, X.P., et al., *Vibrational spectroscopic and density functional studies on ion solvation and association of lithium tetrafluorobrate in acetonitrile.* The Journal of Physical Chemistry A, 2004. **108**(37): p. 7513-7521.

186. Coetzee, J.F. and W.R. Sharpe, *Solute-Solvent Interactions. VII. Proton Magnetic Resonance and Infrared Study of Ion Solvation in Dipolar Aprotic Solvents.* Journal of Solution Chemistry, 1972. **1**(1): p. 77-91.

187. Niedzicki, L., et al., *New type of imidazole based salts designed specifically for lithium ion batteries.* Electrochimica Acta, 2010. **55**(4): p. 1450-1454.

188. Frisch, M.J., et al., *Gaussian 09*. 2016: Wallingford, CT.

189. Bauschlicher, C.W., et al., *Structure and Energetics of Li+-(BF4-)(n ') Li+-(FSI-)(n '), and Li+-(TFSI-)(n): Ab Initio and Polarizable Force Field Approaches.* The Journal of Physical Chemistry B, 2014. **118**(36): p. 10785-10794.

190. Korsun, O.M., et al., *Ion Association in Aprotic Solvents for Lithium Ion Batteries Requires Discrete-Continuum Approach: Lithium Bis(oxalato)borate in Ethylene Carbonate Based Mixtures.* Journal of Physical Chemistry C, 2016. **120**(30): p. 16545-16552.

191. Jiang, B., et al., *The Anion Effect on Li+ Ion Coordination Structure in Ethylene Carbonate Solutions.* The Journal of Physical Chemistry Letters, 2016. **7**(18): p. 3554-3559.

192. Ponnuchamy, V., S. Mossa, and I. Skarmoutsos, *Solvent and Salt Effect on Lithium Ion Solvation and Contact Ion Pair Formation in Organic Carbonates: A Quantum Chemical Perspective.* The Journal of Physical Chemistry C, 2018. **122**(45): p. 25930-25939.

193. Foster, J.P. and F. Weinhold, *Natural Hybrid Orbitals.* Journal of the American Chemical Society, 1980. **102**(24): p. 7211-7218.

194. Rives, A.B. and F. Weinhold, *Natural Hybrid Orbitals - Abinitio Scf and Ci Results for Co and Nico.* International Journal of Quantum Chemistry, 1980. **17**: p. 201-209.

195. Reed, A.E. and F. Weinhold, *Natural Bond Orbital Analysis of near-Hartree-Fock Water Dimer.* Journal of Chemical Physics, 1983. **78**(6): p. 4066-4073.

196. Ghosh, A., et al., *2D IR photon echo spectroscopy reveals hydrogen bond dynamics of aromatic nitriles.* Chemical Physics Letters, 2009. **469**(4-6): p. 325-330.

197. Golonzka, O., et al., *Coupling and orientation between anharmonic vibrations characterized with two-dimensional infrared vibrational echo spectroscopy.* Journal of Chemical Physics, 2001. **115**(23): p. 10814-10828.

198. Ohta, K. and K. Tominaga, *Vibrational population relaxation of thiocyanate ion in polar solvents studied by ultrafast infrared spectroscopy.* Chemical Physics Letters, 2006. **429**(1-3): p. 136-140.

199. Lee, K.K., et al., *Ion-pairing dynamics of Li+ and SCN- in dimethylformamide solution: Chemical exchange two-dimensional infrared spectroscopy.* Journal of Chemical Physics, 2011. **134**(6): p. 064506.

200. Zhang, X., R. Kumar, and D.G. Kuroda, *Acetate ion and its interesting solvation shell structure and dynamics.* The Journal of Chemical Physics, 2018. **148**(9): p. 094506.

201. Hefter, G., *When spectroscopy fails: The measurement of ion pairing.* Pure and Applied Chemistry, 2006. **78**(8): p. 1571-1586.

202. Wang, P.M. and A. Anderko, *Computation of dielectric constants of solvent mixtures and electrolyte solutions.* Fluid Phase Equilibria, 2001. **186**(1-2): p. 103-122.

203. Marcus, Y. and G. Hefter, *Ion pairing.* Chemical Reviews, 2006. **106**(11): p. 4585-4621.

204. Prue, J.E., *Ion Pairs and Complexes - Free Energies Enthalpies and Entropies.* Journal of Chemical Education, 1969. **46**(1): p. 12.

205. Kim, Y.S. and R.M. Hochstrasser, *Chemical exchange 2D IR of hydrogen-bond making and breaking.* Proceedings of the National Academy of Sciences of the United States of America, 2005. **102**(32): p. 11185-11190.

206. Kuroda, D.G. and R.M. Hochstrasser, *Dynamic structures of aqueous oxalate and the effects of counterions seen by 2D IR.* Physical Chemistry Chemical Physics, 2012. **14**(18): p. 6219-6224.

207. He, X.M., et al., *Efficient Vibrational Energy Transfer through Covalent Bond in Indigo Carmine Revealed by Nonlinear IR Spectroscopy.* The Journal of Physical Chemistry B, 2017. **121**(40): p. 9411-9421.

208. Wong, D.B., et al., *Dynamics of Isolated Water Molecules in a Sea of Ions in a Room Temperature Ionic Liquid.* The Journal of Physical Chemistry B, 2013. **117**(2): p. 623-635.

209. Borodin, O. and G.D. Smith, *Quantum Chemistry and Molecular Dynamics Simulation Study of Dimethyl Carbonate: Ethylene Carbonate Electrolytes Doped with LiPF6.* The Journal of Physical Chemistry B, 2009. **113**(6): p. 1763-1776.

210. Tarascon, J.M. and M. Armand, *Issues and challenges facing rechargeable lithium batteries.* Nature, 2001. **414**(6861): p. 359-367.

211. Choi, J.W. and D. Aurbach, *Promise and reality of post-lithium-ion batteries with high energy densities.* Nature Reviews Materials, 2016. **1**(4): p. 1-16.

212. Mizushima, K., et al., *Lixcoo2 "(Oless-Thanxless-Than-or-Equal-To1) - a New Cathode Material for Batteries of High-Energy Density.* Materials Research Bulletin, 1980. **15**(6): p. 783-789.

213. Xu, W., et al., *Lithium metal anodes for rechargeable batteries.* Energy & Environmental Science, 2014. **7**(2): p. 513-537.

214. Liang, X., et al., *A facile surface chemistry route to a stabilized lithium metal anode.* Nature Energy, 2017. **2**(9): p. 17119.

215. Lin, D., et al., *Nanoscale perspective: Materials designs and understandings in lithium metal anodes.* Nano Research, 2017. **10**(12): p. 4003-4026.

216. Niu, C., et al., *High-energy lithium metal pouch cells with limited anode swelling and long stable cycles.* Nature Energy, 2019. **4**(7): p. 551-559.

217. Suo, L., et al., *A new class of solvent-in-salt electrolyte for high-energy rechargeable metallic lithium batteries.* Nature communications, 2013. **4**(1): p. 1-9.

218. Zheng, J., et al., *Research progress towards understanding the unique interfaces between concentrated electrolytes and electrodes for energy storage applications.* Advanced Science, 2017. **4**(8): p. 1700032.

219. Yamada, Y. and A. Yamada, *Superconcentrated electrolytes for lithium batteries.* Journal of The Electrochemical Society, 2015. **162**(14): p. A2406.

220. Wang, L. and X. He, *Nonflammable Pseudoconcentrated Electrolytes for Batteries.* Current Opinion in Electrochemistry, 2021: p. 100783.

221. Nie, M. and B.L. Lucht, *Role of lithium salt on solid electrolyte interface (SEI) formation and structure in lithium ion batteries.* Journal of The Electrochemical Society, 2014. **161**(6): p. A1001.

222. Dahbi, M., et al., *Comparative study of EC/DMC LiTFSI and LiPF6 electrolytes for electrochemical storage.* Journal of Power Sources, 2011. **196**(22): p. 9743-9750.

223. Xin, N., et al., *Solubilities of six lithium salts in five non-aqueous solvents and in a few of their binary mixtures.* Fluid Phase Equilibria, 2018. **461**: p. 1-7.

224. Parimalam, B.S. and B.L. Lucht, *Reduction reactions of electrolyte salts for lithium ion batteries: LiPF6, LiBF4, LiDFOB, LiBOB, and LiTFSI.* Journal of The Electrochemical Society, 2018. **165**(2): p. A251.

225. Seo, D.M., et al., *Reduction reactions of carbonate solvents for lithium ion batteries.* ECS Electrochemistry Letters, 2014. **3**(9): p. A91.

226. Xu, M., et al., *Investigation and application of lithium difluoro (oxalate) borate (LiDFOB) as additive to improve the thermal stability of electrolyte for lithium-ion batteries.* Journal of Power Sources, 2011. **196**(16): p. 6794-6801.

227. Zheng, J., et al., *High-Fluorinated Electrolytes for Li-S Batteries.* Advanced Energy Materials, 2019. **9**(16): p. 1803774.

228. Wohlfarth, C., et al., *Viscosity of Pure Organic Liquids and Binary Liquid Mixtures*. 2001, Germany: Springer Berlin Heidelberg.

229. Wohlfarth, C., *Viscosity of 1, 1, 1, 3, 3-pentafluorobutane.* Landolt Börnstein, 2009. **25**: p. 195.

230. Gao, H.-q., et al., *Structure characterization and electrochemical properties of new lithium salt LiODFB for electrolyte of lithium ion batteries.* Journal of Central South University of Technology, 2008. **15**(6): p. 830-834.

231. Laoire, C.O., et al., *Electrochemical studies of ferrocene in a lithium ion conducting organic carbonate electrolyte.* Electrochimica Acta, 2009. **54**(26): p. 6560-6564.

232. Mozhzhukhina, N. and E.J. Calvo, *Perspective—the correct assessment of standard potentials of reference electrodes in non-aqueous solution.* Journal of The Electrochemical Society, 2017. **164**(12): p. A2295.

233. Leung, K. and J.L. Budzien, *Ab initio molecular dynamics simulations of the initial stages of solid–electrolyte interphase formation on lithium ion battery graphitic anodes.* Physical Chemistry Chemical Physics, 2010. **12**(25): p. 6583-6586.

234. Ganesh, P., D.-e. Jiang, and P. Kent, *Accurate static and dynamic properties of liquid electrolytes for Li-ion batteries from ab initio molecular dynamics.* Journal of Physical Chemistry B, 2011. **115**(12): p. 3085-3090.

235. Pollard, T.P. and T.L. Beck, *Structure and polarization near the Li+ ion in ethylene and propylene carbonates.* Journal of Chemical Physics, 2017. **147**(16): p. 161710.

236. Wolinski, K., J.F. Hinton, and P. Pulay, *Efficient implementation of the gauge-independent atomic orbital method for NMR chemical shift calculations.* Journal of the American Chemical Society, 1990. **112**(23): p. 8251-8260.

237. Pinchas, S. and D. Ben-Ishai, *The carbonyl absorption of carbamates and 2-oxazolidones in the infrared region.* Journal of the American Chemical Society, 1957. **79**(15): p. 4099-4104.

238. Nyquist, R. and W. Potts, *Infrared absorptions characteristic of organic carbonate derivatives and related compounds.* Spectrochimica Acta, 1961. **17**(7): p. 679-697.

239. Fulfer, K.D., et al., *Elucidating the mechanism behind the infrared spectral features and dynamics observed in the carbonyl stretch region of organic carbonates interacting with lithium ions.* Journal of Chemical Physics, 2021. **154**(23): p. 234504.

240. Chen, X.B., et al., *Structure and Dynamics of the Lithium-Ion Solvation Shell in Ureas.* Journal of Physical Chemistry B, 2019. **123**(46): p. 9889-9898.

241. Rushing, J.C., F.M. Leonik, and D.G. Kuroda, *Effect of Solvation Shell Structure and Composition on Ion Pair Formation: The Case Study of LiTDI in Organic Carbonates.* Journal of Physical Chemistry C, 2019. **123**(41): p. 25102-25112.

242. Brooksby, P.A. and W.R. Fawcett, *Infrared (attenuated total reflection) study of propylene carbonate solutions containing lithium and sodium perchlorate.* Spectrochimica Acta, Part A, 2006. **64**(2): p. 372-382.

243. Ribeiro, A., et al., *Relative Permittivities of 1, 1, 1, 2, 3, 3, 3-Heptafluoropropane (HFC-227ea), 1, 1, 1, 2, 3, 3-Hexafluoropropane (HFC-236ea), and 1, 1, 1, 3, 3-Pentafluorobutane (HFC-365mfc) in the Liquid Phase.* Journal of Chemical & Engineering Data, 2007. **52**(5): p. 2041-2049.

244. Fried, S.D., S. Bagchi, and S.G. Boxer, *Measuring electrostatic fields in both hydrogen-bonding and non-hydrogen-bonding environments using carbonyl vibrational probes.* Journal of the American Chemical Society, 2013. **135**(30): p. 11181-11192.

245. Wu, T.-Y., et al., *Influence of LiTFSI Addition on Conductivity, Diffusion Coefficient, Spin–Lattice Relaxation Times, and Chemical Shift of One-Dimensional NMR Spectroscopy in LiTFSI-Doped Dual-Functionalized Imidazolium-Based Ionic Liquids.* Journal of Chemical & Engineering Data, 2015. **60**(3): p. 471-483.

246. Arunan, E., et al., *Definition of the hydrogen bond (IUPAC Recommendations 2011).* Pure and applied chemistry, 2011. **83**(8): p. 1637-1641.

247. Desiraju, G., *Distinction between the weak hydrogen bond and the van der Waals interaction.* Chemical Communications, 1998(8): p. 891-892.

248. Gu, Y., T. Kar, and S. Scheiner, *Fundamental properties of the CH⊙⊙⊙O interaction: is it a true hydrogen bond?* Journal of the American Chemical Society, 1999. **121**(40): p. 9411-9422.

249. Itoh, Y., et al., *N+-CH··· O Hydrogen bonds in protein-ligand complexes.* Scientific reports, 2019. **9**(1): p. 1-12.

250. Scheiner, S. and T. Kar, *Spectroscopic and structural signature of the CH− O hydrogen bond.* The Journal of Physical Chemistry A, 2008. **112**(46): p. 11854-11860.

251. Hobza, P., et al., *Anti-hydrogen bond between chloroform and fluorobenzene.* Chemical physics letters, 1999. **299**(2): p. 180-186.

252. Kankanamge, S.R.G., et al., *Proving and Probing the Presence of the Elusive C-H...O Hydrogen Bond in Liquid Solutions at Room Temperature.* Angewandte Chemie-International Edition, 2020. **59**(39): p. 17012-17017.

253. Kankanamge, S.R.G., et al., *Mechanism behind the Unusually High Conductivities of High Concentrated Sodium Ion Glyme-Based Electrolytes.* Journal of Physical Chemistry C, 2018. **122**(44): p. 25237-25246.

254. Smedley, S.I., *The interpretation of ionic conductivity in liquids*. 1980, New York: Plenum Press. xvi, 195 p.

255. Peljo, P. and H.H. Girault, *Electrochemical potential window of battery electrolytes: the HOMO–LUMO misconception.* Energy & Environmental Science, 2018. **11**(9): p. 2306-2309.

256. Méndez-Hernández, D.D., et al., *Building and testing correlations for the estimation of one-electron reduction potentials of a diverse set of organic molecules.* Journal of Physical Organic Chemistry, 2015. **28**(5): p. 320-328.

257. Gauthier, M., et al., *Electrode–electrolyte interface in Li-ion batteries: current understanding and new insights.* Journal of physical chemistry letters, 2015. **6**(22): p. 4653-4672.

258. Nazri, G.-A. and G. Pistoia, *Lithium batteries: science and technology*. 2008: Springer Science & Business Media.

259. Scrosati, W.A.v.S.B., *Advances in lithium-ion batteries*. 2002: Springer Science & Business Media.

260. Abraham, K. and M. Alamgir, *Room temperature polymer electrolytes and batteries based on them.* Solid State Ionics, 1994. **70**: p. 20-26.

261. Wang, Z., et al., *Competition Between the Plasticizer and Polymer on Associating with Li+ Ions in Polyacrylonitrile-Based Electrolytes.* Journal of the Electrochemical Society, 1997. **144**(3): p. 778.

262. Wang, Z., et al., *Spectroscopic investigation of interactions among components and ion transport mechanism in polyacrylonitrile based electrolytes.* Solid State Ionics, 1999. **121**(1-4): p. 141-156.

263. Choe, H., et al., *Characterization of some polyacrylonitrile-based electrolytes.* Chemistry of materials, 1997. **9**(1): p. 369-379.

264. Bashir, Z., S. Church, and D. Price, *The formation of polymer-solvent complexes of polyacrylonitrile from organic solvents containing carbonyl groups.* Acta polymerica, 1993. **44**(5): p. 211-218.

265. Bashir, Z., *Thermoreversible gels of polyacrylonitrile.* Journal of Polymer Science Part B: Polymer Physics, 1992. **30**(11): p. 1299-1304.

266. Wang, Z., et al., *Investigation of the position of Li+ ions in a polyacrylonitrile-based electrolyte by Raman and infrared spectroscopy.* Electrochimica acta, 1996. **41**(9): p. 1443-1446.

267. Ferry, A., et al., *NMR and Raman studies of a novel fast-ion-conducting polymer-in-salt electrolyte based on LiCF3SO3 and PAN.* Electrochimica acta, 2000. **45**(8-9): p. 1237-1242.

268. Tamimi, A., H.E. Bailey, and M.D. Fayer, *Alkyl chain length dependence of the dynamics and structure in the ionic regions of room-temperature ionic liquids.* The Journal of Physical Chemistry B, 2016. **120**(30): p. 7488-7501.

269. Dahl, K., et al., *Vibrational spectroscopy and dynamics of small anions in ionic liquid solutions.* The Journal of chemical physics, 2005. **123**(8): p. 084504.

270. Bashir, Z., *The hexagonal mesophase in atactic polyacrylonitrile: a new interpretation of the phase transitions in the polymer.* Journal of Macromolecular Science, Part B, 2001. **40**(1): p. 41-67.

271. Bashir, Z., S. Atureliya, and S. Church, *Production of oriented polyacrylonitrile films by flow-induced chain extension and crystallization from solution.* Journal of materials science, 1993. **28**(10): p. 2721-2732.

272. Bashir, Z. and S. Rastogi, *The Explanation of the Increase in Slope at the Tg in the Plot of d-Spacing Versus Temperature in Polyacrylonitrile.* Journal of Macromolecular Science, Part B, 2005. **44**(1): p. 55-78.

273. Reading, M., D. Elliot, and V. Hill. *Some aspects of the theory and practice of modulated differential scanning calorimetry*. in *Proceedings of the 21st North American thermal analysis society conference, Atlanta, Georgia*. 1992.

274. Huang, Y. and J. Koenig, *Raman spectra of polyacrylonitrile.* Applied Spectroscopy, 1971. **25**(6): p. 620-622.

275. Huang, B., et al., *Lithium ion conduction in polymer electrolytes based on PAN.* Solid State Ionics, 1996. **85**(1-4): p. 79-84.

276. Oxtoby, D.W., D. Levesque, and J.J. Weis, *A molecular dynamics simulation of dephasing in liquid nitrogen.* The Journal of Chemical Physics, 1978. **68**(12): p. 5528-5533.

277. Ter, H.D., *Fluctuation, Relaxation, and Resonance in Magnetic Systems*. Vol. 2. 1962: Oliver and Boyd.

278. Oh, K.-I., et al., *Nitrile and thiocyanate IR probes: Molecular dynamics simulation studies.* The Journal of chemical physics, 2008. **128**(15): p. 154504.

279. Maienschein-Cline, M.G. and C.H. Londergan, *The CN stretching band of aliphatic thiocyanate is sensitive to solvent dynamics and specific solvation.* The Journal of Physical Chemistry A, 2007. **111**(40): p. 10020-10025.

280. Demirdöven, N., M. Khalil, and A. Tokmakoff, *Correlated vibrational dynamics revealed by two-dimensional infrared spectroscopy.* Physical review letters, 2002. **89**(23): p. 237401.

281. Kwac, K. and M. Cho, *Two-color pump− probe spectroscopies of two-and three-level systems: 2-dimensional line shapes and solvation dynamics.* The Journal of Physical Chemistry A, 2003. **107**(31): p. 5903-5912.

282. Brinzer, T. and S. Garrett-Roe, *Temperature and chain length dependence of ultrafast vibrational dynamics of thiocyanate in alkylimidazolium ionic liquids: A random walk on a rugged energy landscape.* The Journal of chemical physics, 2017. **147**(19): p. 194501.

283. Bohnke, O., et al., *Fast ion transport in new lithium electrolytes gelled with PMMA. 1. Influence of polymer concentration.* Solid State Ionics, 1993. **66**(1-2): p. 97-104.

284. Henrici-Olive, G. and S. Olivé, *Molecular interactions and macroscopic properties of polyacrylonitrile and model substances*, in *Chemistry*. 1979, Springer. p. 123-152.

285. Rosenbaum, S., *Polyacrylonitrile fiber behavior. I. Mechanisms of tensile response.* Journal of Applied Polymer Science, 1965. **9**(6): p. 2071-2084.

286. Armand, M., *Polymer solid electrolytes-an overview.* Solid State Ionics, 1983. **9**: p. 745-754.

287. Papke, B., M. Ratner, and D. Shriver, *Conformation and ion-transport models for the structure and ionic conductivity in complexes of polyethers with alkali Metal Salts.* Journal of the Electrochemical Society, 1982. **129**(8): p. 1694.

288. Shriver, D., et al., *Structure and ion transport in polymer-salt complexes.* Solid State Ionics, 1981. **5**: p. 83-88.

289. Chu, P. and Z.-P. He, *Lithium complex in polyacrylonitrile/EC/PC gel-type electrolyte.* Polymer, 2001. **42**(10): p. 4743-4749.

290. Chen, X. and D.G. Kuroda, *Molecular motions of acetonitrile molecules in the solvation shell of lithium ions.* The Journal of Chemical Physics, 2020. **153**(16): p. 164502.

VITA

Jeramie Rushing received his Bachelors of Science from The University of Alabama in 2016. He has since worked with Dr. Daniel Kuroda at Louisiana State University, probing electrolytes and studying nonlinear spectroscopy. His areas of research interest include electrolytes, deep eutectic solvents, and metalloid chemistry. He anticipates graduating in spring of 2022.